Mass Assembly in Star Formation via Interstellar Filaments

by

Michael Chun-Yuan Chen
B.Sc., University of British Columbia, 2012
M.Sc., University of Victoria, 2015

A Dissertation Submitted in Partial Fulfillment of the
Requirements for the Degree of

DOCTOR OF PHILOSOPHY

in the Department of Physics and Astronomy

Mass Assembly in Star Formation via Interstellar Filaments

by

Michael Chun-Yuan Chen
B.Sc., University of British Columbia, 2012
M.Sc., University of Victoria, 2015

Supervisory Committee

Dr. James Di Francesco, Supervisor
(Department of Physics and Astronomy & National Research Council of Canada)

Dr. Jon Willis, Supervisor
(Department of Physics and Astronomy)

Dr. Adam Monahan, Outside Member
(School of Earth and Ocean Sciences)

ABSTRACT

Understanding how diffuse molecular clouds at large scales ($\sim$ 10 pc) assemble mass into dense, star-forming cores at small scales ($\sim$ 0.1 pc) is crucial to building a holistic theory of star formation. While recent observations suggest that filaments play an important role in the mass assembly of dense cores, detailed gas kinematics studies are still lacking. My dissertation presents three innovative techniques that enable us to study star-forming filaments' complex gas kinematics in unprecedented detail: multi-component spectral fit, multi-dimensional filament identification, and membership assignment of velocity-coherent structures. Through these techniques, I analyzed star-forming filaments in the Perseus Molecular Cloud and unveiled unexpectedly complex velocity structures at scales where filaments are well resolved, to as low as the 0.01 pc scale. Moreover, the correlations I discovered between the various filament properties further suggest a scenario in which thermally supercritical filaments grow continuously via accretion from their surroundings while simultaneously forming cores through fragmentation along their lengths.

Contents

Supervisory Committee ii

Abstract iii

Table of Contents iv

List of Figures vii

Acknowledgements x

Dedication xi

1 Introduction 1

1.1 Star Formation Among the Cosmos 1
1.2 Molecular Clouds 2
1.3 Interstellar Filaments 4
1.4 Observing Physical Properties of Molecular Gas 7
1.4.1 Ammonia Inversion Transition 8
1.4.2 Radiative Transfer 11

2 Velocity-Coherent Filaments in NGC 1333: Evidence for Accretion Flow? 15

2.1 Introduction 15
2.2 Models & data 18
2.2.1 NH_3 Line Models 18
2.2.2 Synthetic Spectra 20
2.2.3 NH_3 Observations, Reduction, and Imaging 21
2.3 Analysis Methods 22
2.3.1 Spectral Fitting 22
2.3.2 Performance Tests on Line Fitting 27

2.3.3 Identifying Velocity Coherent Filaments . . . 29
2.3.4 Velocity Gradient Analysis . . . 35
2.4 Results . . . 38
2.4.1 NGC 1333 - Fitted Models . . . 38
2.4.2 NGC 1333 - Velocity Gradients . . . 39
2.5 Discussion . . . 40
2.5.1 Comparing with N_2H^+ Analysis of NGC 1333 . . . 40
2.5.2 Velocity Gradients on Large Scales . . . 43
2.5.3 Velocity Gradients on Small Scales . . . 45
2.6 Summary . . . 51

3 Turbulence, Accretion, and Infall: a High-resolution Study of the B5 Filaments 54
3.1 Introduction . . . 54
3.2 Data . . . 57
3.3 Method . . . 58
3.3.1 Spectral-fitting . . . 58
3.3.2 Filament Identification . . . 61
3.4 Results . . . 62
3.4.1 Derived $v_{\rm LSR}$ and σ_v maps . . . 62
3.4.2 Identified Filaments . . . 65
3.4.3 Velocity-coherent Maps . . . 66
3.5 Discussion . . . 68
3.5.1 Ambient environment . . . 68
3.5.2 Dense, subsonic structures . . . 70
3.5.3 Radial Profiles . . . 71
3.5.4 Velocity Gradients . . . 78
3.6 Summary and Conclusions . . . 88

4 Filament Accretion and Fragmentation in the Perseus Molecular Cloud 91
4.1 Introduction . . . 91
4.2 Data . . . 93
4.3 Method . . . 94
4.3.1 Spectral Fitting . . . 94

4.3.2 Filaments Identification and Analysis 94
4.4 Results and Discussion 97
4.4.1 Spectrally Modelled Data 97
4.4.2 The role of clump environment 97
4.4.3 Velocity dispersion and gradients 100
4.4.4 Filament fragmentation, cores, and YSOs 104
4.4.5 Velocity gradient orientations 107
4.5 Summary and Conclusions 109

5 Conclusions **112**
5.1 Conclusions of the Dissertation 112
5.2 Work Moving Forward 113
5.2.1 Investigating the Role of Magnetic Fields 113
5.2.2 Multi-tracer Surveys 114
5.3 Synthetic Observations 115

Bibliography **117**

A Further details on filament identification and membership assignment **131**
A.1 Parameter choices for CRISPy 131
A.2 Membership Assignment to Velocity Coherent Structures 132

List of Figures

Figure 1.1 The CO column density map of the Taurus Molecular Cloud . . 2
Figure 1.2 The core mass function and the initial mass function 6
Figure 1.3 An illustration of NH_3 inversion and its respective potential energy curve 9
Figure 1.4 An example synthetic spectrum of the NH_3 (1,1) lines 11

Figure 2.1 Example NH_3 (1,1) spectra taken from a synthetic spectral cube and the NGC 1333 observations 19
Figure 2.2 Confusion matrices quantifying MUFASA's ability to classify the number of velocity slabs. 23
Figure 2.3 The true-positive rate of identifying a two-slab spectrum plotted as a function of the $v_{\rm LSR}$ separation between the slabs 26
Figure 2.4 The 1-σ error of the fitted $v_{\rm LSR}$ and σ_v as a function of SNR . . 28
Figure 2.5 The debelended cube of NGC 1333 and the CRISPy identified filament spines 30
Figure 2.6 Snapshots of SCMS finding a 2D 'density' ridge 32
Figure 2.7 An illustration of 3D skeleton pruning 33
Figure 2.8 An illustration of how a ppv-footprint is produced iteratively . 35
Figure 2.9 Distance transform of a filament spine overlaid with its corresponding divergence and parallel fields 36
Figure 2.10 Relative likelihood of the fitted models in NGC 1333 and examples of these spectral fits 37
Figure 2.11 The $v_{\rm LSR}$, $\nabla v_{\rm LSR,\parallel}$, and $\nabla v_{\rm LSR,\perp}$ maps of the NGC 1333 filaments 39
Figure 2.12 The ratio between σ_v of two velocity slabs versus velocity separation between these slabs 41
Figure 2.13 The $v_{\rm LSR}$ and σ_v profiles along the NGC 1333 filament spines . 43
Figure 2.14 Radial profiles of $|\nabla v_{\rm LSR,\perp}|$ and $|\nabla v_{\rm LSR,\parallel}|$ for the NGC 1333 filaments 49

Figure 2.15Polar histograms of the $\nabla v_{\rm LSR}$ orientations measured in the NGC 1333 filaments 51

Figure 3.1 The NH_3 integrated intensity maps of B5 for the GBT-only and the GBT+VLA observations 57
Figure 3.2 The relative likelihood maps of the B5 fits to the GBT-only and the VLA+GBT data, accompanied by examples of these fits . . 59
Figure 3.3 The $v_{\rm LSR}$ and σ_v maps derived from the GBT-only data and the VLA+GBT data 61
Figure 3.4 The PDF of the $v_{\rm LSR}$ for the narrow, wide, and only components derived from fits to the B5 GBT and VLA+GBT data 63
Figure 3.5 The PDF of the σ_v for the narrow, wide, and only components derived from fits to the B5 GBT and VLA+GBT data 64
Figure 3.6 The integrated intensity, $v_{\rm LSR}$, and σ_v maps of B5 overlaid with the identified filament spines 65
Figure 3.7 The $v_{\rm LSR}$ and σ_v profiles along the B5 filament spines 67
Figure 3.8 The integrated intensity and the ambient-component $v_{\rm LSR}$ maps of the GBT-only observations of B5 69
Figure 3.9 Radial profiles of the NH_3 integrated intensities for the B5 filaments. 72
Figure 3.10Radial profiles of $v_{\rm LSR}$ for the B5 filaments 75
Figure 3.11Radial profiles of σ_v for the B5 filaments 76
Figure 3.12Line integral convolution of the $\nabla v_{\rm LSR}$ field overlaid on the NH_3 integrated intensity and $\log|\nabla v_{\rm LSR}|$ maps of B5 79
Figure 3.13The $\nabla v_{\rm LSR,\perp}$, $\nabla v_{\rm LSR,\parallel}$, and $|\nabla v_{\rm LSR}|$ maps of B5 81
Figure 3.14The radial profiles of $|\nabla v_{\rm LSR,\perp}|$ and $|\nabla v_{\rm LSR,\parallel}|$ of the B5 filaments 85
Figure 3.15Polar histograms of the $\nabla v_{\rm LSR}$ orientations measured in the B5 filaments 87

Figure 4.1 The H_2 column density map of Perseus West with contours of where one- and two-component NH_3 spectra are detected 96
Figure 4.2 The H_2 column density map of Perseus East with contours of where one- and two-component NH_3 spectra are detected 97
Figure 4.3 $v_{\rm LSR}$ versus $M_{\rm lin}$ for the Perseus filaments 98
Figure 4.4 The inter-filament $v_{\rm LSR}$ dispersion in each star-forming clump versus the clump mass 99

Figure 4.5 σ_v versus $M_{\rm lin}$ for the Perseus filaments 101
Figure 4.6 $|\nabla v_{\rm LSR,\perp}|$ versus $|\nabla v_{\rm LSR,\parallel}|$ for the Perseus filaments 102
Figure 4.7 $|\nabla v_{\rm LSR,\perp}|$ and $|\nabla v_{\rm LSR,\parallel}|$ versus $M_{\rm lin}$ for the Perseus filaments . . 103
Figure 4.8 $|\nabla v_{\rm LSR,\perp}|$ and $|\nabla v_{\rm LSR,\parallel}|$ versus σ_v for the Perseus filaments . . . 104
Figure 4.9 The number of cores per unit length versus $M_{\rm lin}$ for the Perseus filaments 105
Figure 4.10 The number of class 0/1 YSOs per unit length versus $M_{\rm lin}$ for the Perseus filaments 106
Figure 4.11 The number of cores per unit length and the numbers of Class 0/I YSOs per unit length versus σ_v for the Perseus filaments . . 107
Figure 4.12 $|\nabla v_{\rm LSR,\perp}|$ versus number of class 0/1 YSOs per unit length for the Perseus filaments 108
Figure 4.13 The 'randomness' of the $\nabla v_{\rm LSR}$ orientations versus σ_v for the Perseus filaments 109

ACKNOWLEDGEMENTS

I would like to thank:

My Advisor James, for your mentorship, support, encouragement, and patience. You truly empowered me to grow into the scientist and the person I am proud to have become.

Erik Rosolowsky, for opening the door to this remarkable journey and guiding me to make the most out of my PhD.

Jared Keown, for sharing the joy, struggle, and delicious foods together as my academic sibling.

Helen Kirk, for always having your door open and allowing me to ask embarrassing questions, share my excitement for science, or just have a lovely chat.

Ayla Barten, for supporting me as a friend and a roommate incredibly during my final year of PhD amidst a global pandemic. Also, for being a giant derp.

Maan Hani, for being de-acknowledged. Your perspectives, insights, and actions challenged me profoundly in the most positive way. You are an inspiring friend.

Steve Mairs, for being there since the beginning. I relish the depths of our conversations and the incredible growth we shared as friends.

My fellow grad students, especially Asya, Bobby, Collin, Hannah, Jason, Mara, and Sébastien, to name a few. Your friendship and the memories we shared will be deeply treasured.

The Lekwungen peoples, on whose traditional territory I pursued my PhD, and the **Songhees, Esquimalt and WSÁNEĆ peoples** whose historical relationships with the land continue to this day.

There are no mistakes, only happy accidents.
Bob Ross

DEDICATION

To my dearest parents,
爸媽，謝謝你們一路下來的愛，關懷，鼓勵，與付出。

Chapter 1

Introduction

1.1 Star Formation Among the Cosmos

Star formation is one of the fundamental drivers of galactic evolution and a key player in forming life as we know it. When the Universe cooled and became dark shortly following the Big Bang, star formation relit the Universe by transforming gas into stars, populating galaxies full of these nuclear engines as they form. To this day, optical and dust-reprocessed infrared starlight still dominates the total photon energy budget at shorter wavelengths, with the afterglow of the Big Bang lurking in the longer wavelength microwave range (Dole et al., 2006).

Star formation determines and self-regulates the population of stars being born, which in turn sets the chemical evolution of galaxies as stars process the primordial gas consisting of only hydrogen, helium, and lithium into heavier elements. The heavier elements such as carbon, nitrogen, and oxygen, are the basis of life as we know it, while silicon and iron compose the rocky planets and moons on which life may develop. Star formation also plays a vital role in galaxies' dynamic evolution by transforming gas into collisionless stars. It helps to set the distribution of visible matters within a galaxy by determining where stars are born and by further perturbing the remaining gas with feedback from the stars it forms.

Planets, such as the one that hosts us and ones we hope to find life on, are a byproduct of star formation. The initial conditions posed by star formation on the formation and subsequent evolution of planets may therefore be crucial to setting up the right stage for life to develop. The complex organic molecules which form inside cold, dense star-forming gas may also provide life with the necessary building blocks

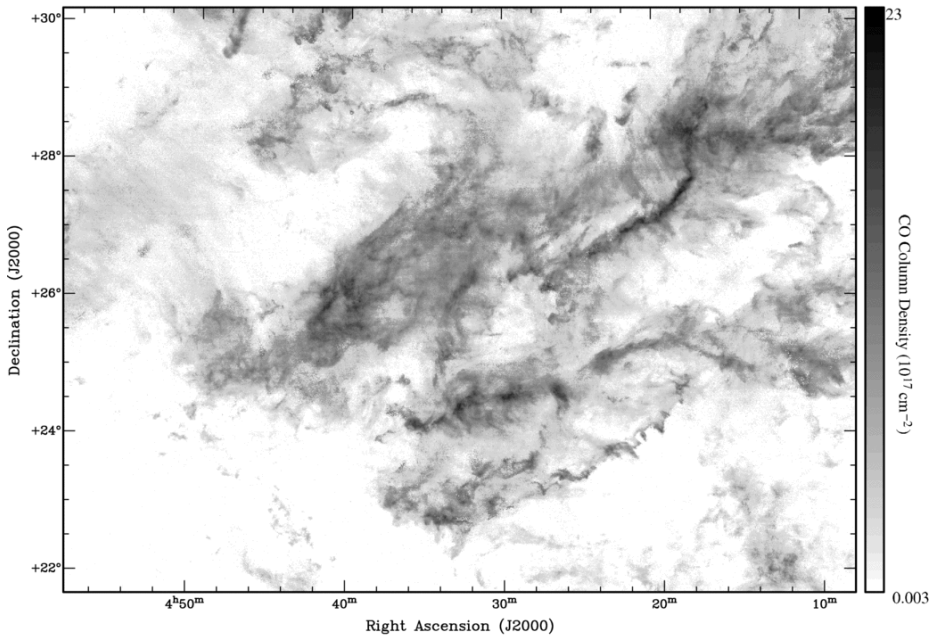

Figure 1.1: The CO column density map of the Taurus molecular cloud showing the hierarchical nature of the cloud. The grey scale is expressed as the square root of the CO column density (Pineda et al., 2010b).

from the start, making star formation not only crucial to the cosmic evolution at large but also our own origin story.

1.2 Molecular Clouds

Stars are born out of the cold, dense molecular gas predominantly found in molecular clouds (MC). MCs are typically $\sim 10^4 - 10^6$ $M_\odot$[i] in mass (McKee & Ostriker, 2007) and $\sim 1 - 100$ pc[ii] in size (Solomon et al., 1987). The particle densities within individual clouds can range between 1 cm^{-3} and 10^6 cm^{-3}. MCs are structurally hierarchical, meaning their smaller structures are typically found within larger structures over a wide range of scales. In gravitationally bounded clouds, these scales range from the cloud size down to the thermal Jeans length, the smallest size for which a body of gas can collapse against thermal pressure (McKee & Ostriker, 2007).

Figure 1.1 shows an example of such a hierarchy in the Taurus molecular cloud, where cores or a cluster of cores are embedded within filaments, which in turn form

[i]Solar masses, 1 $M_\odot \simeq 1.99 \times 10^{33}$g

[ii]Parsecs, 1 pc $\simeq$ 3.26 light-years or $\simeq 3.1 \times 10^{18}$ cm

a network within the cloud. A dense core is defined as the smallest unit of self-gravitating overdensity, typically $\sim$ 0.1 pc in size, for which a stellar system can form directly out of via gravitational collapse (Stahler & Palla 2005; Di Francesco et al. 2007). A filament, on the other hand, is more loosely defined as an elongated overdensity with a high aspect ratio.

The hierarchical nature of an MC has often been seen as the consequences of the turbulence within a cloud (e.g., Elmegreen et al. 2000). Indeed, MCs are very turbulent as inferred from kinematic observations. The total velocity dispersion ($\sigma_{\rm v}$) measured towards MCs tends to be an order of magnitude larger than its corresponding thermal velocity dispersion ($\sigma_{\rm v,T} \sim 0.1$ km s^{-1}), indicating that gas motions within MCs are dominated by supersonic turbulence (e.g., Larson 1981; Solomon et al. 1987). Moreover, the observed velocity dispersion appear to be empirically correlated to the size of the MCs, characterized by what is known as Larson's first law (Larson, 1981) and takes the following form as measured by Solomon et al. (1987),

$$\sigma_{\rm v} = (1.0 \pm 0.1)\, R_{\rm pc}^{0.5\pm0.05}\ {\rm km\ s^{-1}}, \tag{1.1}$$

where $R_{\rm pc}$ is the size of the measured cloud in unit of parsecs. As shown by Heyer & Brunt (2004), this law not only holds for individual clouds but also for substructures within a cloud, further suggesting the universality of turbulence in MCs.

Turbulence has been proposed to be a mechanism that helps support MCs against their own weight and subsequently suppresses the high, theoretical star formation rates compared to the actually observed lower rates (e.g., Krumholz & McKee 2005). Indeed, under the microturbulent approximation, random compressive motions on the small-scales can contribute ram-pressures that collectively give rise to a global "turbulent pressure" that is often expressed as

$$P = \rho {\sigma_{\rm v,NT}}^2, \tag{1.2}$$

where ρ and $\sigma_{\rm v,NT}$ are the average density and the non-thermal velocity dispersion of a cloud structure, respectively (McKee & Ostriker, 2007). Such a microturbulent approximation holds well when the pressure is evaluated at a size scale that is much larger than the observed non-thermal motions or when the object being evaluated has a lifespan much longer than the dynamical time.

In addition to supporting the cloud, supersonic turbulence found in numerous

3D hydrodynamic (e.g., Nordlund & Padoan 1999) and magnetohydrodynamic (e.g., Ostriker et al. 2001) simulations can naturally produce hierarchical structures that have lognormal density distribution when self-gravity is unimportant. This density distribution is similar to those found in the observations for structures with column densities less than $\sim 10^{21}$ cm^{-2} (e.g., André et al. 2011; Schneider et al. 2013), just below the thresholds for which dense cores are found, i.e., in the regime where self-gravity is important (e.g., Onishi et al. 1998; Heiderman et al. 2010). Turbulence thus appears to be important not only for supporting the larger cloud as a whole but also for creating small-scale overdensities for which gravitational instability can develop and ultimately collapse into stars.

1.3 Interstellar Filaments

The hierarchical and turbulent nature of MC structures suggests that the formation of these structures is also hierarchical. Filamentary structures being part of such a hierarchy has been known for a while (e.g., Schneider & Elmegreen 1979; Bally et al. 1987), with the ubiquity of filaments within MCs confirmed by the more recent, large sample studies conducted with the *Herschel* Space Observatory (e.g., André et al. 2010). The role in which filaments play in the hierarchy is further confirmed with the finding that dense cores are statistically more likely to be found in filaments with column densities greater than $\sim 7 \times 10^{21}$ cm^{-2}, suggesting that cores are indeed formed out of filaments (André et al. 2014).

In terms of simple analytical models such as an infinite isothermal cylinder (e.g., Stodólkiewicz 1963; Ostriker 1964; Inutsuka & Miyama 1997), the formation of dense cores can occur via filament fragmentation when a filament reaches beyond a critical line density for which its weight can no longer be supported by thermal pressure. The critical line density in such a model can be written as

$$M_{\rm lin,crit} = \frac{2c_s^2}{G}, \tag{1.3}$$

where G is the gravitational constant and c_s is the isothermal sound speed of the gas

$$c_s^2 = \sqrt{\frac{kT}{m_{\rm p}}}, \tag{1.4}$$

where k is the Boltzmann constant, T is the temperature of the gas, and $m_{\rm p}$ is the mean particle mass of the gas (see Inutsuka & Miyama 1997). For an assumed temperature of $\sim$ 10 K, this critical line density corresponds to $M_{\rm lin,crit} \simeq 16$ M$_\odot$ pc^{-1}, which is within a factor of 2 of those found in filaments that preferentially host dense cores (André et al. 2014).

Due to MCs' complex nature, the physical characteristics of filaments are far from the ideals assumed by analytical models. Detailed models that treat the turbulent cloud as a whole are therefore needed. Numerical simulations have shown that filaments can be naturally produced under various physical conditions. These conditions include clouds with supersonic converging flows both in the absence (Gong & Ostriker 2011a) and presence (Chen & Ostriker 2014a) of a magnetic field, as well as those with a strong magnetic field regulated by ambipolar diffusion, i.e., the coupling to a magnetic field via the collision of its neutrals with its ions (Li & Nakamura 2004). Detailed, statistical comparisons between the observed filaments with those found in the simulations are thus needed to constrain these models.

In particular, it is important to study filaments in terms of their role in the mass assembly of dense cores. There appears to be a universal, empirical law that describes the probability in which a star with a given initial mass can be born, known as the initial mass function (IMF; e.g., Salpeter 1955; Kroupa 2001; Chabrier 2003). Interestingly, the probability distribution of core masses, i.e., the core mass function (CMF; e.g., Motte et al. 1998), seem to share a very similar shape as the IMF, suggesting that the initial mass distribution of stars are set by the core formation mechanism. Figure 1.2 shows some of the well-accepted IMFs plotted against the CMF measured by Könyves et al. (2010) in the Aquila rift cloud complex. If the CMF does indeed map directly onto the IMF, then being able to establish a fundamental understanding of how dense cores are assembled would have profound implications on the origin of stellar populations in the cosmos.

With regards to the mass assembly of dense cores via filaments, there are several outstanding questions. First, how do filaments become supercritical with respect to its gravitational stability? Do supercritical filaments form directly out of turbulent compression or do they form from mass accretion of their subcritical progenitors? Second, what is the role of filaments in core and core cluster formation? Do filaments feed core clusters via mass transport along their lengths like their cosmological counterparts? Third, how much of a role does turbulence play in filament fragmentation in addition to gravity? Do gas motions within a filament have first to become sub-

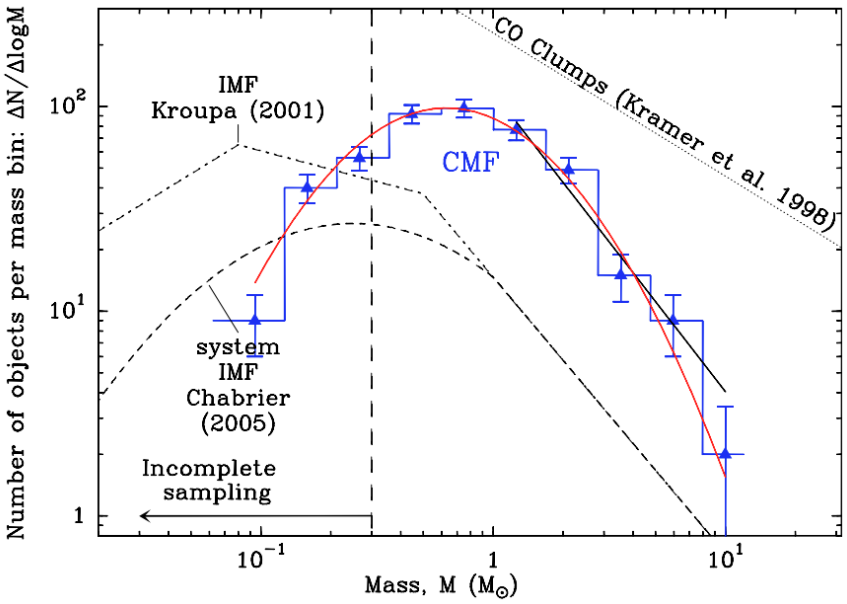

Figure 1.2: The CMF (blue) constructed from ~ 500 candidate prestellar cores identified in Aquila (Könyves et al. 2010), overlaid with its corrosponding lognormal fit (red). The IMF of single stars (Kroupa 2001), multiple systems (e.g., Chabrier 2005), and the typical mass of CO clumps (e.g., Kramer et al. 1998) are shown in various black dash lines for a comparison.

sonic before the filament becomes gravitationally unstable? In this dissertation, I will address these questions via a large sample study of filament kinematics in the nearby MCs, the first study of its kind.

1.4 Observing Physical Properties of Molecular Gas

Directly observing cold molecular gas is difficult because its primary constituent H_2 emits very little light at low temperatures. The moment of inertia for a H_2 molecule is relatively low, which means its rotational energy levels are relatively far apart and can only be sufficiently excited at high temperatures ($\sim$ 1000 K; Stahler & Palla 2005). Furthermore, H_2 lacks a permanent electric dipole moment, which means its rotational transitions have to occur via a quadrupole-enabled transition that can be much less probable than a dipole-enabled transition. Probing star-forming gas thus has to be done via observations of other emitters within the gas that we call tracers.

Interstellar dust grains mixed in with the gas are one of the most important tracers of star-forming gas. Their thermal emission typically dominates the total energy budget of Galactic continuum emission in the spectral range between far-infrared and microwaves, and is usually optically thin. The latter property is very beneficial for structural studies of cloud mass because it allows all the dust along a line of sight to be observed. Furthermore, since thermal dust emission intensity is temperature-sensitive, these dust grains' temperature can be determined by measuring their relative intensity at different wavelengths. At high enough densities where the gas and dust are thermally coupled, i.e., $> 10^4$ cm^{-3}, this property allows the gas temperature to be measured in addition to its mass, enabling one to estimate a structure's thermal stability against gravity. Kinematic information is further needed if non-thermal support also needs to be accounted for.

Gas kinematics cannot be inferred from thermal dust emission. Continuum emission, such as thermal dust emission, does not intrinsically have distinct spectral features to which Doppler shifts associated with gas motions can be measured. Monochromatic spectral lines are therefore needed for any kinematic study. For this reason, carbon monoxide, CO, being the second most abundant molecule next to H_2 and which also possesses a dipole moment, is commonly used to probe kinematics of star-forming gas.

Using CO as a tracer of star-forming gas can have a few notable drawbacks. Being an abundant molecule, with an average abundance of $\sim$ 1 per 10^4 H_2 particles,

CO emission can become optically thick quickly even when the gas column density is moderate. While this limitation can be addressed by observing one of the less abundant isotopomers of CO, such as $C^{18}O$, carbon-bearing molecules such as CO also freeze-out easily onto dust grain surfaces in cold, high-density environments deep in the interiors of clouds. Such a depletion typically occurs at densities $> 10^4$ cm^{-3} (e.g., Tafalla et al. 2002), making CO an unsuitable tracer of dense gas. Alternative tracers, however, such as NH_3 and N_2H^+, are available to probe kinematics of gas that is sufficiently dense to collapse under self-gravity. Both NH_3 and N_2H^+ also have low-level transitions that excite at higher densities than those for CO and are much more resilient to depletion onto dust grains.

1.4.1 Ammonia Inversion Transition

Ammonia (i.e., NH_3) is one of the most important molecular tracers used to study the coldest phases of ISM (Ho & Townes 1983; Benson & Myers 1989), and hence star-forming gas. Not only is NH_3 one of the most abundant molecular species found in the ISM, with a typical abundance of ~ 1 per 10^8 H_2 particles in dense cores (e.g., Friesen et al. 2009), its large number of transitions is also sensitive to a wide range of excitation conditions, making it an excellent diagnostic of these gas (Ho & Townes, 1983). The fact that many NH_3 transitions occur within a narrow range of frequencies also means these transitions can often be observed simultaneously with the same instrument, greatly reducing calibration errors when making line ratio measurements (Stahler & Palla 2005).

NH_3 is sensitive to a wide range of gas densities, ranging between $\sim 10^3$ cm^{-3} (Evans 1999), where dense gas tracers such as N_2H^+ can be destroyed by undepleted CO (Tafalla et al. 2002), up to $\sim 10^6$ cm^{-3} where most neutral molecules are frozen onto dust grains (Caselli et al. 2003). Unlike CO, the brightest molecular emitter in the ISM, NH_3 does not deplete easily onto dust grains at higher densities and is typically optically thin in star-forming gas, which allows its emission to trace the entire gas structure along a line of sight. These two factors make NH_3 an excellent tracer of intermediate-to-high density gas, which includes both the ambient gas falling onto filaments as well as the filaments and dense cores themselves.

NH_3 is a symmetric top molecule, meaning two of its three, non-zero principal moment of inertia components are equal in magnitude. This arrangement gives NH_3 two degrees of rotational freedom, allowing it to rotate about its axis of symme-

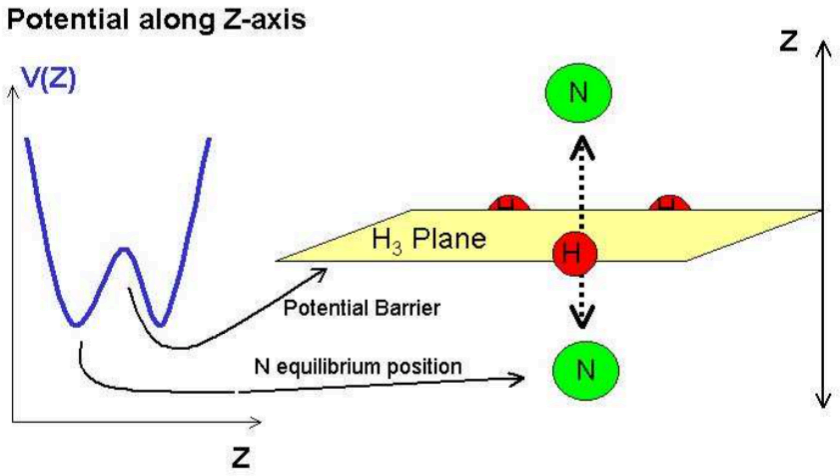

Figure 1.3: An illustration of ammonia inversion (right) and its respective potential energy curve as a function of ammonia's symmetry axis, Z (left) take from Shirley (2003).

try like a spinning top and tumble 'sideways' like a dumbbell. These two degrees of rotational freedom give rise to rotational energy structures that can be fully described by the quantum numbers J and K, i.e., its total angular momentum and its axis-of-symmetry-projected counterpart, respectively. These energy structures can be visualized as a set of ladders where individual ladders and their rungs are described by K and J, respectively. By convention, each rotational state is designated by its principal quantum number as (J, K).

The individual rotational levels of NH_3 are further split into two due to the inversion of its nitrogen atom across the plane of symmetry defined by the three hydrogen atoms, i.e., the H_3 plane. Figure 1.3 shows an illustration of the NH_3 inversion and its respective potential energy curve as a function of NH_3's symmetry axis, Z. Classically, one can think of such a system as an umbrella constantly inverting its curvature back and forth. Unlike a classical system, however, the position of the nitrogen atom is not well defined and the atom 'exists' simultaneously on two sides of the H_3 plane. Indeed, there are two distinct, total wave functions that describe the state of the nitrogen atom, which are the symmetric (+) and antisymmetric (-) combinations of the atoms's wave functions to the left and right of the H_3 plane, Ψ_L and Ψ_R, respectively, i.e.,

$$\Psi_+ = \frac{1}{\sqrt{2}} \left(\Psi_L + \Psi_R \right) \tag{1.5}$$

$$\Psi_- = \frac{1}{\sqrt{2}} \left(\Psi_L - \Psi_R \right). \tag{1.6}$$

The two energy states associated with these two wave functions are known as the inversion doublets.

The inversion doublets found in the lowest rotational state of each K ladder, i.e., $J = K$, are metastable because rotational states with $J \geq K$ tend to decay rapidly down a K ladder, and the dipole transitions between K ladders are radiatively forbidden. This metastability means the $J = K$ doublets are predominantly excited by collision and can be well approximated by a two-level system to calculate important gas properties such as kinematic temperatures or gas densities (Ho & Townes, 1983). This behavior is why NH_3 inversion transitions are perhaps the most astrophysically important lines to observe for NH_3.

The NH_3 inversion doublets are each further split into hyperfine structures. First, the interaction between the electric quadrupole moments found within the nitrogen

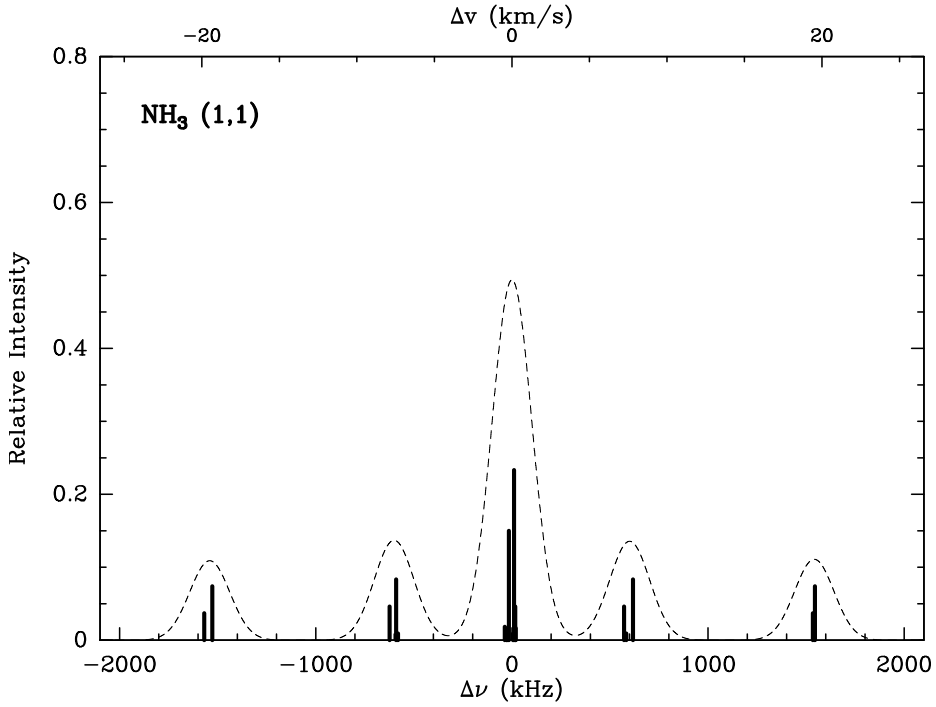

Figure 1.4: Synthetic spectrum of the NH_3 (1,1) transition lines showing the hyperfine structures and their relative intensities (solid lines). Its Gaussian broadened counterpart, with a linewidth of $\sigma_\nu = 100$ kHz, is shown with dashed lines (Mangum & Shirley, 2015).

nucleus and the electric field generated by the three hydrogen atoms splits each doublets into three hyperfine states. These three states are then further split into more hyperfine states by the relatively weaker interaction between the magnetic dipoles of the three hydrogen nuclei and the magnetic field generated from molecular rotation. Figure 1.4 shows the hyperfine structure of the NH_3 (1,1) inversion transition and its relative intensities in a synthetic spectrum. Since the intrinsic intensities of the NH_3 hyperfine lines are well known (Townes & Schawlow, 1975), the optical depth of the emission can also be directly determined from the intensity ratios of the observed hyperfine lines (Mayer et al. 1973; Barrett et al. 1977; Ho & Townes 1983).

1.4.2 Radiative Transfer

To model the observed emissions well, we need to understand how light interacts with matter as it traverses through a medium towards us. The light matter interaction

along an infinitesimal path can be described by the radiative transfer equation,

$$\frac{dI_\nu}{d\tau} = -I_\nu + S_\nu(\vec{r}) \tag{1.7}$$

where I_ν is the specific intensity of the traversing light, τ_ν is the optical depth of the path, and S_ν is the source function of the medium, which accounts for both emission and absorption. The subscript ν denotes that these quantities are frequency dependent. Formally, I_ν is defined as

$$I_\nu = \frac{dE}{d\nu\, dA\, dt\, d\Omega\, cos\theta}, \tag{1.8}$$

where E and ν are the energy and the frequency of the incoming ray, respectively, A is the area over which the ray is received, Ω is the solid angle the source subtends, and θ is the angle between dA and the incoming ray.

For a system with two populations of particles, n_1 and n_2, each occupying a distinct energy state and which are in equilibrium with one another, we can implicitly define the excitation temperature of the system, T_{ex}, in terms of its Boltzmann distribution as,

$$\frac{n_1}{n_2} = \frac{g_1}{g_2} \exp\left(\frac{h\nu}{kT_{ex}}\right), \tag{1.9}$$

where k is the Boltzmann constant, $h\nu = \Delta E$ is the energy gap between the two states, and g_1 and g_2 are the statistical weights of the states 1 and 2, respectively. Since the generalized source function in the framework of the Einstein relations is given by

$$S_\nu = \frac{2h\nu^3}{c^2}\left(\frac{g_2 n_1}{g_1 n_2} - 1\right)^{-1}, \tag{1.10}$$

where c is the speed of light in vacuum and h is the Planck constant, we can further express the source function as the following by combining Equation 1.9 and Equation 1.10:

$$S_\nu = B_\nu\left(T_{ex}\right) \tag{1.11}$$

where B_ν is the Planck's law,

$$B_\nu(T) = \frac{2h\nu^3}{c^2}\frac{1}{e^{h\nu/kT} - 1}. \tag{1.12}$$

For a slab of homogeneous medium, we can solve the radiative transfer equation

(Equation 1.7) and obtain the following:

$$I_\nu = B_\nu(T_{ex})(1 - e^{-\tau_\nu}) + I_\nu^{bg} e^{-\tau_\nu}, \tag{1.13}$$

where I_ν^{bg} is the specific intensity of the background radiation.

Since the observed Doppler shift in frequency is directly proportional to the radial velocity of the emitter in the non-relativistic regime, it is often useful to perform radiative transfer modelling in velocity space instead of frequency space. In this framework, the optical depth of an uniform slab moving with a bulk radial velocity of v_0 can be modelled by a single Gaussian as,

$$\tau(v) = \tau_0 e^{\frac{-(v-v_0)^2}{2\sigma_v^2}}, \tag{1.14}$$

where v is the radial velocity centroid, σ_v is the radial velocity dispersion, and τ_0 is the peak optical depth. This model assumes the radial velocity profile of a slab to be a composite of a thermal and a non-thermal component, both which are Gaussians that consequently add in quadrature, i.e.,

$$\sigma_v^2 = \sigma_{v,T}^2 + \sigma_{v,NT}^2. \tag{1.15}$$

To account for transitions with hyperfine structures, such as NH_3 inversion transitions, the $\tau(v)$ of a single velocity component model takes the form of

$$\tau(v) = \sum_{i=1}^{n} W_i \tau_0 e^{\frac{-(v-v_0-\delta v)^2}{2\sigma_v^2}}. \tag{1.16}$$

where n is the number of hyperfine components, i is the index of the individual components, W_i is the weight of the components, δv is the velocity shift of the components with respect to the velocity centroid, and the rest of the parameters are the same as those specified in Equation 1.14. As it can be seen, the hyperfine model splits the otherwise single Gaussian $\tau(v)$ profile into a superposition of multiple Gaussians centred around $v = v_0 - \delta v$ and weighted by W_i, whose sum normalizes to one.

The models which adopt the kinematic profiles described by Equations 1.14 for a uniform slab of gas are often referred to as the one-slab model or single velocity component model. The models which describe multiple gas slabs along a line of sight with these kinematic profiles are often referred to as the multiple-slab or multiple

velocity component models.

Chapter 2

Velocity-Coherent Filaments in NGC 1333: Evidence for Accretion Flow?

The material in this chapter was originally published in the Astrophysical Journal Volume 891, Issue 1, id.84, 18 pp. (2020) under the same title by Michael Chun-Yuan Chen, James Di Francesco, Erik Rosolowsky, Jared Keown, Jaime E. Pineda, Rachel K. Friesen, Paola Caselli, How-Huan Chen, Christopher D. Matzner, Stella S. Offner, Anna Punanova, Elena Redaelli, Samantha Scibelli, and Yancy Shirley. The analysis was led by me with data acquisition carried out by members of the GAS Survey Team (Friesen et al., 2017), including myself. Erik Rosolowsky implemented the base version of the synthetic spectra generator for which I expanded and improved upon to include features such as multi-processing. Jared Keown and Jaime Pineda helped test the generator, with Jared Keown contributed additionally to the software development of the generator.

2.1 Introduction

Molecular cloud filaments appear to play a pivotal role in star formation. In addition to being featured prominently in star-forming regions (e.g., Schneider & Elmegreen 1979; Bally et al. 1987) and being ubiquitous in molecular clouds at large (e.g., André et al. 2010), filaments appear to harbour most of the observed dense cores (e.g., Men'shchikov et al. 2010; Könyves et al. 2015), the smallest structure from

which stellar systems emerge (see Di Francesco et al. 2007). Theoretically, filaments appear to form naturally from supersonic turbulent motions of a cloud in numerical simulations, both in the absence (e.g., Porter et al. 1994) and in the presence (e.g., Jappsen et al. 2005) of self-gravity. Moreover, filaments appear to be analytically the most favoured structure to grow locally and fragment readily under weak perturbations in a finite cloud (Pon et al. 2011). Such properties likely make filaments highly effective at assembling dense cores from a molecular cloud prior to, or even in the absence of, an overwhelming, global cloud collapse.

How dense cores relate to their host filaments is currently not well understood. Gravitationally induced fragmentation along filament lengths, like those found in numerical models (e.g., Bastien et al. 1991; Inutsuka & Miyama 1997), has been suggested to be how supercritical filaments produce cores, as inferred by *Herschel* observations (see André et al. 2014). While Hacar & Tafalla (2011) found that dense structures in the L1517 filament correlate with oscillatory line-of-sight velocities, suggesting filament fragmentation, such behaviour has not been generally observed in other filaments (e.g., Tafalla & Hacar 2015). Other core formation mechanisms, such as those that form cores and filaments simultaneously in simulations (e.g., Gong & Ostriker 2011b; Chen & Ostriker 2014a, 2015a; Gómez & Vázquez-Semadeni 2014), may thus play an important role in star formation as well.

In addition to forming cores, filaments in simulations accrete material from their surroundings and transport mass along their lengths to feed dense cores and protoclusters (e.g., Balsara et al. 2001; Smith et al. 2011, 2016; Gómez & Vázquez-Semadeni 2014). Indeed, velocity gradients observed across (e.g., Palmeirim et al. 2013; Fernández-López et al. 2014; Dhabal et al. 2018) and along (e.g., Kirk et al. 2013a; Friesen et al. 2013) filaments have been interpreted as evidence for such accretion onto and along these filaments, respectively. Further kinematic studies are needed to understand how such filaments fit within the wide variety of existing models and how they assemble mass in star formation in detail.

A filament that appears to be a single, coherent (i.e., continuous) structure on the sky may not necessarily be truly coherent in three dimensional, position-position-position (ppp) space. Multiple structures that are distinct in ppp space can appear as a single structure by mere projection along lines of sight. With CO observations, Hacar et al. (2013) showed that a seemingly coherent filament on the sky can in fact contain multiple velocity-coherent 'fibres' when viewed in position-position-velocity (ppv) space.

While some ppv fibres may indeed trace physical ppp sub-filaments like those produced in simulations (e.g., Moeckel & Burkert 2015; Smith et al. 2016; Clarke et al. 2017), synthetic CO observations of a simulation showed that ppv fibres do not necessarily map well onto ppp structures, and vice versa (Clarke et al. 2018a). Structures that are coherent in ppv space can still suffer from line-of-sight confusion when distinct ppp structures possess similar velocities (e.g., Beaumont et al. 2013). Such a scenario can be common, for example, when multiple ppp structures are swept up by a large-scale flow. Fortunately, denser gas tracers such as NH_3 and N_2H^+ are expected to be less susceptible to these problems due their lower volume-filling fraction in a cloud. This claim seems to be supported by Tafalla & Hacar (2015), who observed only a single N_2H^+ ppv fibre over each line of sight where multiple CO ppv fibres had been detected earlier by Hacar et al. (2013).

Regardless of how well ppv coherent (hereafter velocity-coherent) structures map onto ppp space, multi-component line modelling is needed to avoid deriving erroneous gas properties that are unphysical. Kinematic analyses that perform multiple-component fits to a large number of spectra, however, are uncommon. This situation is due to the typical need for human intervention in popular least-squares fitting methods, such as the Levenberg–Marquardt (LM; Levenberg 1944; Marquardt 1963; Moré 1978) method, and the inefficiencies associated with many automated approaches, such as the grid-search or Markov chain Monte Carlo (MCMC) methods.

Recent automated methods for multi-component fits, such as Behind The Spectrum (BTS; Clarke et al. 2018a) and GaussPy+ (Riener et al., 2019), work only with optically-thin, Gaussian lines by design. Other methods that fit hyperfine lines, such as those used by Henshaw et al. (SCOUSE, 2016) and Hacar et al. (2017), are semi-automatic and hence are still subject to human biases. An efficient, automated method that fits hyperfine lines is therefore highly desirable for kinematic studies that use species like NH_3 and N_2H^+ to trace dense cores and filaments.

In this paper, we describe an automated, generalizable method that fits two-component NH_3 (1,1) spectra efficiently using the LM method, without the need for user-provided initial guesses. The fitted models are subsequently used to identify filament spines in ppv space, which are sorted into velocity-coherent filaments accordingly. Moreover, we present a novel approach to study velocity gradients in filaments on beam-resolved scales, where velocity gradients are decomposed into components that are parallel and perpendicular with respect to local filament spines. Such a technique enables us to explore filament kinematics and accretion flow directions on the

dense core (< 0.1 pc) scale in addition to the filament scale (> 0.5 pc).

We apply our new methods to filaments seen in NH_3 (1,1) data of the NGC 1333 region. Located at a distance of about 295 pc away (Ortiz-León et al. 2018; Zucker et al. 2018), the NGC 1333 star-forming clump in the Perseus molecular cloud is one of the nearest cluster-forming regions. Its properties make NGC 1333 an ideal place to study the interplay between filaments and cores in a cluster-forming environment in detail. NGC 1333 is also one of the most extensively studied star-forming clumps (see Walawender et al. 2008), providing a wealth of context within which our study can be placed.

This paper is laid out as follows. We describe our NH_3 (1,1) model, synthetic data, and observed data of NGC 1333 in Section 2.2. Methods behind our analysis, as well as test results of our line-fitting method, are presented in Section 2.3. The results of our analysis on the NGC 1333 observations are presented in Section 2.4, followed by a discussion of these results in Section 2.5. A concluding summary is in Section 2.6.

2.2 Models & data

We used two data sets for our work presented here: one synthetic and one observational. The spectral model behind our line fits is described in Section 2.2.1 while the synthetic data used to test the accuracy of our line-fitting method is described in Section 2.2.2. The observations we used for this work are obtained from the Green Bank Ammonia Survey (GAS; Friesen et al. 2017) and are presented in Section 2.2.3.

2.2.1 NH_3 Line Models

We modelled observations of the NH_3 (1,1) inversion transition along a given line of sight with up to two homogeneous bodies of beam-filling gas known as slabs. Each slab in our model corresponds to a kinematic (i.e., velocity) component observed in a spectrum and is assumed to be at a local thermal equilibrium with itself. Furthermore, we assume the emission can be parameterized by excitation temperature (T_{ex}), optical depth (τ_0), velocity dispersion (σ_v), and velocity centroid in the local standard of rest

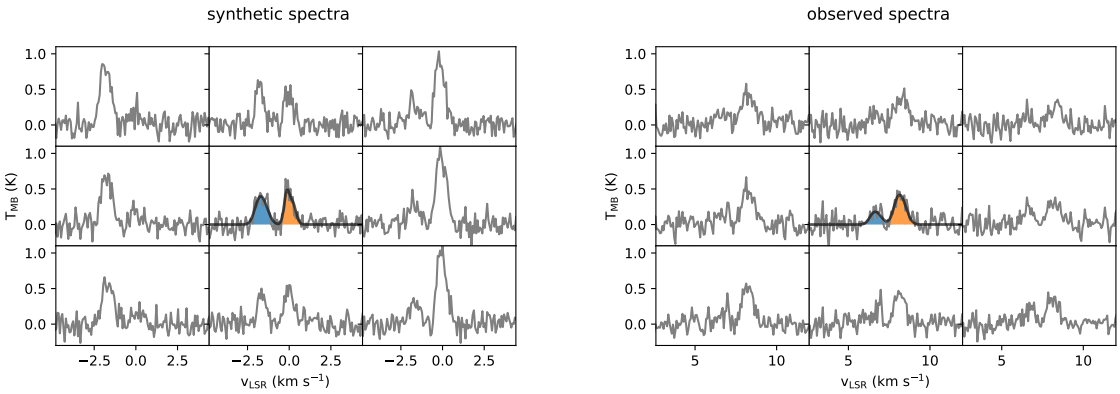

Figure 2.1: NH_3 (1,1) spectra (grey) taken from a synthetic spectral cube (left) and the NGC 1333 observation (right) over a grid of 3×3 footprint, zoomed in to focus on the main hyperfine structures. Models fitted to all 18 hyperfine component of the spectra in the center pixel are shown in black, and the individual components of the model are shown in blue and orange.

frame ($v_{\rm LSR}$). The optical depth profile of each slab is described by

$$\tau(v, \sigma_v) = \sum_{i=1}^{n} W_i \tau_0 \exp\left[\frac{-(v - v_{\rm LSR} - \delta v_i)^2}{2\sigma_v^2}\right], \tag{2.1}$$

where W_i and δv_i are the relative weight and velocity offset of each of the eighteen NH_3 (1,1) hyperfine components, respectively. These weights and velocity offsets are tabulated by Mangum & Shirley (2015). We further note that the τ_0 here corresponds to the combined optical depth of all the hyperfine components.

The radiative transfer of our model emission through each slab is governed by:

$$I_\nu = B_\nu(T_{ex})(1 - e^{-\tau_\nu}) + I_\nu^{bg} e^{-\tau_\nu}, \tag{2.2}$$

where I_ν^{bg} is the specific intensity of the background radiation and $B_\nu(T)$ is the Planck function at a temperature T. Each slab is assumed to have a constant T_{ex} and we adopt the cosmic microwave background (CMB), as the I_ν^{bg} for our first slab, i.e., the slab furthest from the observer. We then subsequently use the emergent I_ν of the first slab as the I_ν^{bg} of our second slab to complete the calculation. To mimic baseline-removal used in our data reduction, a constant value of $B_\nu(T_{\rm CMB} = 2.73{\rm K})$ is subtracted from Equation 2.2 in our final I_ν model.

While we assume the slab furthest from an observer to be the optically thicker slab in our initial guesses, our least-squares fitting routine ultimately decides the order of

the modelled slabs along the line of sight. We note that such an ordering of the slabs is unimportant when the two slabs are optically thin with respect to each other, or when two optically thick slabs are not spectrally overlapped due to large $v_{\rm LSR}$ separations. Since the satellite hyperfine lines of NH_3 (1,1) emissions are optically thin in most cases, they help to constrain our kinematic fits well even when the main hyperfine lines are optically thick. Such a constraint allows our fitting method to distinguish double spectral peaks resulting from a line absorption profile from those resulting from superpositions. We implicitly explore how the ordering of the slabs affects our fitting accuracy with the performance test described below in Section 2.2.2.

Since this paper focuses exclusively on understanding the gas kinematics, we analyzed only the NH_3 (1,1) lines to maximize our spatial coverage for the study. As the (2,2) line is expected to be weaker than the (1,1) line, this strategy enabled us to extend our analysis over wider regions where the NH_3 (2,2) line is not detected. While such an approach does not allow us to derive T_{ex} and τ_0 accurately for purely optically thin slabs, where the two parameters are spectrally degenerate, it does remove the potential bias that comes with assuming a single T_{ex} for both the (1,1) and (2,2) lines.

2.2.2 Synthetic Spectra

To test the accuracy of our line-fitting method, we generated a set of 25,000 synthetic NH_3 (1,1) spectra, each from either a one- or two-slab model that fills the beam. To motivate our test set physically, we constructed each of our synthetic slabs with the NH_3 model adopted by the GAS DR1 first results paper (Friesen et al. 2017) instead of using our fitting model, described earlier in Section 2.2.1. The model adopted by the DR1 paper is based on the work by Rosolowsky et al. (2008) and Friesen et al. (2009), and developed from the framework described in Mangum & Shirley (2015).

Each gas slab in our testing model is physically parametrized by the para-ammonia column density, N, and the kinetic temperature, $T_{\rm k}$, in addition to σ_v, $v_{\rm LSR}$, and T_{ex}. We further assumed these slabs are in local thermal equilibrium (LTE), i.e., $T_{ex} = T_{\rm k}$, and draw parameters behind each instance of synthetic slab randomly from the predefined distributions specified below:

- N is drawn from a log-uniform distribution in the range of $13 \leq \log\left(N/{\rm cm}^{-2}\right) < 14.5$;

- $T_{\rm k}$ is drawn from a uniform distribution in the range of 8 K $\leq T_{\rm k} <$ 25 K;
- σ_v is the quadrature sum of the thermal line width, $\sigma_{v,\rm T} = 0.08$ km s^{-1}, and the non-thermal line width, $\sigma_{v,\rm NT}$, where ln $[\sigma_{v,\rm NT}/(\text{km s}^{-1})]$ is drawn from a normal distribution with a mean and a standard deviation of -2.3 and 1.5, respectively. This particular line width distribution is chosen to resemble those found in the GAS DR1 first results, and;
- $v_{\rm LSR}$ of the first gas slab is drawn from a uniform distribution in the range of -2.5 km s^{-1} $\leq v_{\rm LSR} <$ 2.5 km s^{-1} while the $v_{\rm LSR}$ offset of the second slab from the first is drawn independently from the same distribution.

We chose these distributions to represent broadly the typical physical conditions seen towards nearby molecular clouds with NH_3.

We constructed a two-slab spectrum using the same radiative transfer formalism described by Equation 2.2, with the CMB subtracted as a constant. The final synthetic spectrum is produced by adding random Gaussian noise with an rms value of 0.1 K to the model spectrum. The value of 0.1 K is chosen to mimic the typical noise level found in the GAS DR1 observations (Friesen et al., 2017).

For each instance of randomly generated spectrum, eight additional, spatially-correlated spectra are produced. Collectively, these spectra are placed in a 3×3 spatial grid with the original spectrum positioned in the centre. The purpose behind creating such a cube is to provide spatial information for fitting methods that utilize them, including the method presented in this paper.

The spatial correlation between pixels of a synthetic cube is achieved by applying spatial gradients to the model parameters, referenced at the central pixel. The gradients used for each parameter are randomly drawn from a Gaussian distribution with a 1-σ values of 0.2 K, 0.1 km s^{-1}, 0.1 km s^{-1}, and 0.01 for $T_{\rm k}$, σ_v, $v_{\rm LSR}$, and log (N), respectively, per pixel. Figure 2.1 (left) shows spectra extracted from such a synthetic cube, displayed spatially on a 3×3 grid.

2.2.3 NH_3 Observations, Reduction, and Imaging

We observed the Gould Belt molecular clouds with NH_3 (1,1) and (2,2) inversion lines as a part of the GAS survey (Friesen et al. 2017). The GAS observations were made with the Robert C. Byrd Green Bank Telescope (GBT) using its 7-beam K-Band Focal Plane Array (KFPA) and its VErsatile GBT Astronomical Spectrometer

(VEGAS) backend. The angular and spectral resolutions (FWHMs) of our NH_3 data are $32''$ and ~ 0.07 km s^{-1} (i.e., 5.7 kHz at 23.7 GHz), respectively.

Our targets are observed using the On-The-Fly (OTF) technique, where a $10' \times 10'$ on-sky tile was scanned with a Nyquist-sampled spacing between each row. We reduced these observations with the GBT KFPA data reduction pipeline (Masters et al. 2011) and imaged them with the recipe described by Mangum et al. (2007). Further details of the observations, data reduction, and imaging are available in the GAS first results paper (Friesen et al. 2017). For this work, we will focus on the observations of NGC 1333 star-forming clump, available to the public via Data Release 1 (DR1) of the first results paper. Figure 2.1 shows example spectra on its left panel extracted from the DR1 data over a 3×3 pixel region in NGC 1333.

2.3 Analysis Methods

Here, we present our analysis methods in this section below. Details of our spectral fitting method are provided in Section 2.3.1. We conducted a performance test on our fitting method to quantify its accuracy and completeness, and we present the details and the results of this test in Section 2.3.2. Methods for identifying velocity-coherent filaments and assigning component memberships to these filaments based on the fits are presented in Section 2.3.3. Methods behind velocity gradient analysis are presented in Section 2.3.4.

2.3.1 Spectral Fitting

We fitted our synthetic and real data automatically using the Levenberg–Marquardt (LM; Levenberg 1944; Marquardt 1963; Moré 1978) least-squares minimization method. We bypassed the need for user-provided initial guesses using an automated approach described in Section 2.3.1 and performed least-squares fits using the PySpecKit package (Ginsburg & Mirocha, 2011). The `Python` implementation of the LM method used by the PySpecKit is based on the `FORTRAN` version found in the MINPACK-1 package (Moré et al., 1980), made available via a series of translations (Rivers 2002; Markwardt 2009). Our fits are performed on a pixel-by-pixel basis for all the pixels in our data, excluding noisy regions near the map edges. We use a statistical method described in 2.3.1 to discern whether a pixel is better modelled by noise, a one-component model, or a two-component model. Our fitting package is publicly

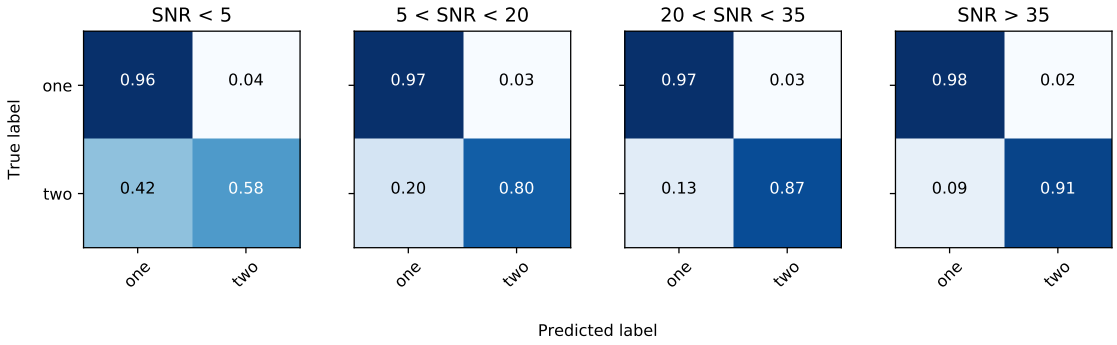

Figure 2.2: Confusion matrices quantifying MUFASA's ability to classify the number of velocity slabs behind a synthetic spectrum. Each matrix contains a subset of our samples at a given range of SNR values.

available via *GitHub* under a GNU General Public License as the MUFASA[i] (i.e., MUlti-component Fitter for Astrophysical Spectral Applications). The version we used for this work is archived in Zenodo (Chen, 2020a).

Making Initial Guesses

The LM method is an iterative approach to find local minima using a hybrid algorithm of the gradient-ascent and the Gauss–Newton methods (see Lourakis 2005). Due to the nature of these methods, good initial guesses are typically needed with the LM method to find the global minima. Such guesses are particularly required for complex spectral models with many local chi-squared minima and are the reasons why many earlier efforts to fit multiple slab models (e.g., Hacar et al. 2013; Henshaw et al. 2016) require human intervention and are not fully automated. For our method, i.e. MUFASA, we fit spectra automatically using initial guesses generated from a recipe described below. A statistical technique (see Section 2.3.1) is used thereafter to decide which of the one- or two-slab models fitted for each pixel is more appropriate, without human intervention.

The GAS DR1's one-slab fitting method used an effective and automated recipe to make initial guesses. The recipe used the first and second moments of the central, i.e., main, NH_3 (1,1) hyperfine lines as its initial $v_{\rm LSR}$ and σ_v guesses. Such a calculation excludes the satellite hyperfine lines because their large velocity offsets are not a kinematic feature. The main hyperfine lines were isolated for such a calculation in

[i] `MUFASA` codebase: `https://github.com/mcyc/mufasa`.

DR1 via a user-defined spectral window.

For our one-slab model fits, we adopt the DR1 recipe for our initial guesses of $v_{\rm LSR}$ and σ_v, but define our spectral windows automatically instead. We automate such a process by centering a 6 km s^{-1} full-width window on the emission peak of the spatially integrated spectrum of our data. Since the NH_3 (1,1) emission should be optically thin throughout the majority of the data, such an emission peak should locate the whereabouts of the main hyperfine lines. Once the window is defined, we follow the DR1 recipe and calculate the zeroth, first, and second moments (μ_0, μ_1, μ_2) of the main hyperfine lines over the window.

To obtain initial guesses for T_{ex} and τ_0 better than assuming fixed values, we use the zeroth moment (μ_0) map as a proxy instead. Specifically, we calculate our guesses by first normalizing the 99.7 percentile value of the μ_0 distribution across the map to one. The initial guesses for T_{ex} and τ_0 are then obtained from the normalized μ_0, i.e., $\widetilde{\mu_0}$, as $\widetilde{\mu_0} \cdot T_{gmx}$ and $\widetilde{\mu_0} \cdot \tau_{gmx}$, respectively, where $T_{gmx} = 8$ K and $\tau_{gmx} = 1$. The resulting fits from adopting such guesses do not depend sensitively on T_{gmx} and τ_{gmx} around these chosen values.

We expand the DR1 fitting recipe further for our two-slab fits via the following steps:

1. Adopt the first and second $v_{\rm LSR}$ guesses as $\mu_1 \pm 0.4\ \mu_2$, respectively.
2. Adopt the first and second σ_v guesses both as $0.5\ \mu_2$, respectively.
3. Adopt the first and second T_{ex} guesses as $\widetilde{\mu_0}\ T_{gmx}$ and $0.8\ \widetilde{\mu_0}\ T_{gmx}$, respectively.
4. Adopt the first and second τ_0 guesses as $0.75\ \widetilde{\mu_0}\ \tau_{gmx}$ and $0.25\ \widetilde{\mu_0}\ \tau_{gmx}$, respectively.

As with the guesses used for one-slab fits, our choices for T_{gmx} and τ_{gmx}, and their respective scaling factors, do not affect the fitting outcome sensitively. Our choices for these values are motivated by a hypothetical scenario where the two gas slabs emitting a spectrum have comparable velocity dispersions, densities, and kinetic temperatures. We note that our initial guesses assume the slab further from the observer has a higher optical depth. As we show below in Section 2.3.2, our recipe for making guesses for the two-slab fit is robust even when the gas slabs emitting the spectrum have dissimilar velocity dispersions, i.e., contrary to this assumption.

To take advantage of spatial information present in our observations, we first fit data that are spatially convolved to an angular resolution twice the size of the original resolution. The parameter maps derived from this initial fit are then median-smoothed and interpolated. For T_{ex} and τ_0 guesses, values outside of ranges 3 - 8 K and 0.2 - 8, respectively, are removed prior to median-smoothing and interpolation. These post-processed parameter maps are then adopted as the initial guesses of our fits to the full resolution cubes.

By using parameters fitted to the spatially convolved cube as initial guesses for the full-resolution fit, we are able to take advantage of the enhanced signal-to-noise ratio (SNR) in addition to the spatial information present in the convolved cube to improve our fits. Figure 2.1 shows spectra extracted over a 3×3 pixel region from a synthetic data cube (left) and the DR1 data of NGC 1333 (right), demonstrating the spatial correlation of these spectra between pixels. The two-slab model fitted to the central pixel using this method is overlaid over the central spectrum.

Since moment estimates for making initial guesses may overlook a faint spectral component in the presence of a much brighter one, we further fit one-slab models to our fit residuals in an attempt to recover missing components. The spectral window used to estimate initial guesses for this fit is centered on the $v_{\rm LSR}$ derived from the initial one-slab fit, with a full window width of 7 km s^{-1}.

We use the results of the one-slab residual fit subsequently to assist with the recovery of a missing component. These results are taken in tandem with those of the original one-slab fit as initial guesses for the re-attempt at fitting a two-slab model. We perform these re-attempts over pixels where one-slab models initially fit the full spectrum better than the two-slab models, as determined by the selection criterion described in the next section (i.e., Section 2.3.1). The same criteria is used further to determine whether or not this new two-slab fit is justified over the one-slab fit.

Model selection

Many previous multi-component fitting methods selected their best fit models for each component via an SNR threshold (e.g., Sokolov et al. 2017), a velocity separation threshold, or both (e.g., Hacar et al. 2013, Hacar et al. 2017, Chen et al. 2019b). While these criteria are effective at avoiding overfitting, they are not necessarily good at picking up all the spectral components present along a given line of sight. We addressed this issue by using the corrected Akaike information criterion (AICc;

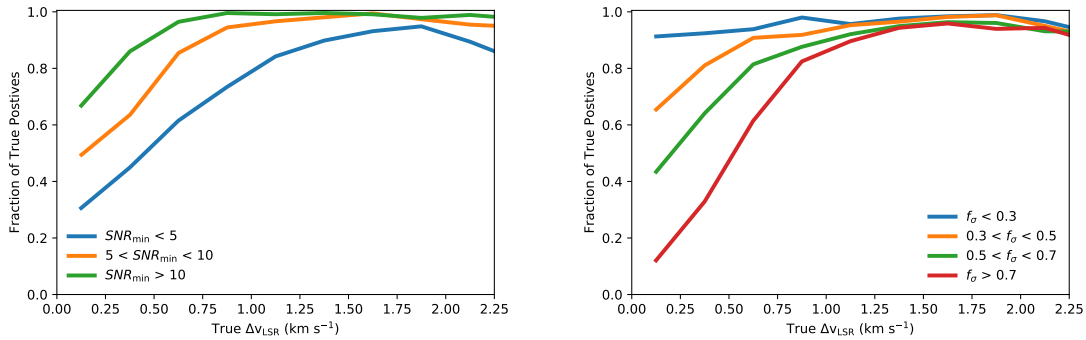

Figure 2.3: The rate of true-positive identification of a two-slab spectrum plotted as a function of the $v_{\rm LSR}$ separation between the slabs. The left panel shows these test samples binned by the SNR values of the fainter slab while the right panel shows these values binned by velocity dispersion ratio f_σ of the narrow slab with respect to the wide slab. The median σ_v values for the narrow and wide components in these samples are 0.23 km s^{-1} and 0.48 km s^{-1}, respectively.

Akaike 1974; Sugiura 1978) to select the best model between the one- and two-slab fits, on a pixel-by-pixel basis.

The AICc is a second-order corrected estimator, based on the K-L information loss (Kullback & Leibler 1951), for the relative likelihood of one model with respect to another at representing a dataset with N samples. Assuming the errors in the data are normally distributed, the AICc can be written in terms of the χ^2 of the fit as:

$$\mathrm{AICc} = \chi^2 + 2p + \frac{2p(p+1)}{N-p-1}, \tag{2.3}$$

where p is the number of parameters used in the model. At each pixel, we accept a two-slab model as the better fit over its one-slab counterpart when their relative likelihood, K_1^2, given by

$$\ln K_2^1 = -\left(\mathrm{AICc}_2 - \mathrm{AICc}_1\right)/2 \tag{2.4}$$

is greater than 5 (Burnham & Anderson, 2004). Similarly, we accept a one-slab model as the better fit over a $I_\nu = 0$ model of a noise with no free parameter when their relative likelihood, $\ln K_0^1$, is greater than 5.

Pixels with reduced χ^2 values of $\chi^2_\nu > 1.5$ are further masked from our analysis to ensure spectra which are inadequately modelled by our fits, e.g., those with possibly three or more velocity slabs, are not included in the analyses. In NGC 1333, no pixel

is masked out as all pixels best fitted by 2-slab models have $\chi^2_\nu < 1.5$.

2.3.2 Performance Tests on Line Fitting

Figure 2.2 summarizes the performance of our line-fitting method, MUFASA, at identifying the correct number of velocity slabs behind a synthetic spectrum, using confusion matrices. These results are obtained from fits to all 25,000 synthetic test spectra described in Section 2.2.2 and are binned into separate matrices according to the SNR of their true underlying spectra. Unless stated otherwise, we refer to SNR as the modelled peak brightness to noise ratio of a final, radiatively transferred spectrum rather than that of its individual components. As illustrated in Figure 2.2, our fitting method identifies true one-slab spectra robustly. The true-positive rate of this identification is greater than 96% even for our lowest SNR (< 5) bin. For two-slab identification, the true-positive rate correlates with the SNR value of the spectra, reaching values upwards of about 90% at higher SNR. Even at moderate SNRs between 5 and 20, the true-positive rate is roughly 80% for two-slab spectra.

We next explore the impact of velocity separation between the slabs and intrinsic velocity dispersion (i.e., σ_v) on the success of our fitting method. Figure 2.3 shows the rate of true-positive identification of a two-slab spectrum as a function of the $v_{\rm LSR}$ separation between the slabs, i.e., $\Delta v_{\rm LSR}$. The left panel shows these rates binned according to the SNR value of the fainter slab, i.e., $\rm SNR_{min}$.

The response curves in Figure 2.3 show the same shape across various $\rm SNR_{min}$ regimes. Namely, they increase monotonically with $\Delta v_{\rm LSR}$ until the fraction of true-positive identification plateaus at 100%. Prior to plateauing, these curves shift vertically upwards as the $\rm SNR_{min}$ increases and behave qualitatively the same even when they are binned instead according to the SNR of the brighter slab, i.e., $\rm SNR_{max}$, or the SNR taken from the peak of the combined spectrum (i.e., the SNR).

The only exception to this plateauing trend is when $\rm SNR_{min}$ is low, i.e., at a value less than 5. At this low SNR regime, the true-positive rate reaches a maximum of 95% at a value of about 1.9 km s^{-1} before it turns around instead of plateauing. This turnaround in the true-positive rate likely reflects the limit of our ability to make initial guesses, suggesting that moment maps may have trouble picking up fainter components when these components reside near the edges of the spectral window from which moment maps are calculated from.

The performance of MUFASA decreases with decreasing $\Delta v_{\rm LSR}$, likely resulting

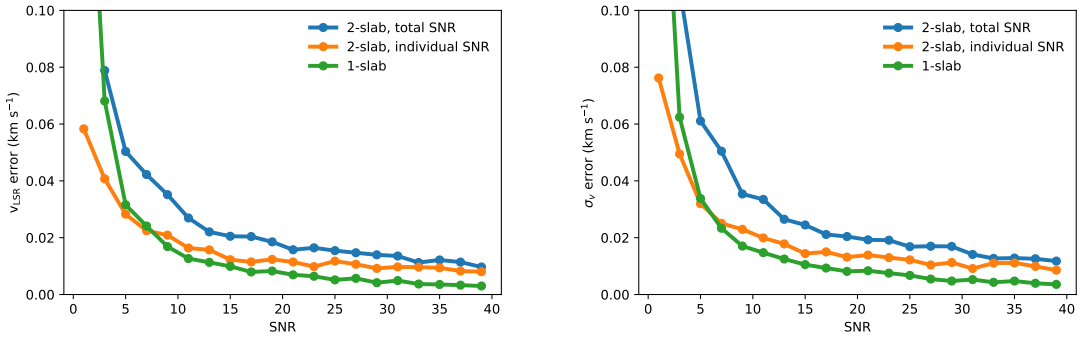

Figure 2.4: The 1-σ error of the fitted $v_{\rm LSR}$ (left) and σ_v (right) as a function of (blue) the total SNR of a 2-slab spectrum, (orange) the SNR of a given slab in a spectrum, and (green) the SNR of a one-slab spectrum, for fits with correct number of identified components.

from a lack of velocity acuity between two slabs when they have similar velocities. As $\Delta v_{\rm LSR}$ decreases, the spectral profiles of the two slabs start to blend together, making them more difficult to distinguish from a one-slab profile. This lack of acuity is what prompted many studies to adopt a $\Delta v_{\rm LSR}$ threshold for their model selection to guard against overfitting (e.g., Hacar et al. 2013), and remains a challenge even for advanced machine learning techniques (e.g., Keown et al. 2019).

The right panel of Figure 2.3 shows the true-positive identification rates divided into various regimes of velocity dispersion ratio, i.e., the line width of the narrower slab relative to its wider counterpart along a line of sight ($f_\sigma = \sigma_{\rm v,narrow}/\sigma_{\rm v,wide}$). Here, the true-positive rate anti-correlates strongly with f_σ. This true-positive rate is likely enhanced when the spectral profiles from the slabs are less similar, i.e., when f_σ is low, which makes them easier to discern from one another when their amplitudes are different. Indeed, this rate can be as high as 90% for spectra with $f_\sigma < 0.3$ and correlates weakly with $\Delta v_{\rm LSR}$ in this regime.

Such enhanced identification rates in the low f_σ regime make MUFASA particularly useful for disentangling subsonic gas from supersonic gas along lines of sight. For reference, the median σ_v values for the narrow and wide components in our test samples are 0.23 km s^{-1} and 0.48 km s^{-1}, respectively, whereas the isothermal sound speed at 10 K is ~ 0.2 km s^{-1}. Like the trend seen in the left panel, the true-positive rate correlates with $\Delta v_{\rm LSR}$ for most f_σ values prior to plateauing. The slope of these correlations, however, becomes shallower as f_σ decreases.

Figure 2.3 reveals that MUFASA is able to recover a large fraction of two-slab

spectra that would otherwise be missed by using a $\Delta v_{\rm LSR}$ threshold for model selection. For a spectral population described by our synthetic spectra, at least 20% and 30% of the second slab missed by a threshold of 0.25 km s^{-1} (e.g., Hacar et al. 2017) and a 0.4 km s^{-1} (e.g., Chen et al. 2019b), respectively, are recovered with MUFASA. These recovery rates can be significantly higher, however, depending on the SNR and f_σ.

Figure 2.2 reveals that MUFASA rarely overfits one-slab spectra, i.e., misidentifying a one-slab spectrum as having two slabs. Our test shows MUFASA only misidentifies one-slab spectra $< 3\%$ of the time. Even in the lowest SNR regime, such misidentification only occurs 4% of the time. Performing model selection via AICc alone is thus sufficient to guard against overfitting without needing an additional threshold criterion.

To quantify how well MUFASA captures the true $v_{\rm LSR}$ and σ_v, Figure 2.4 shows the true 1-σ errors of these two parameter fits as a function of the following values: the SNR of a two-slab spectrum, the SNR of an individual slab in a two-slab spectrum, and the SNR of a one-slab spectrum. These SNR-error relations are plotted with errors calculated from the median absolute deviation (MAD) of the fitted parameters with respect to the true value behind a synthetic spectrum. As expected, the parameter errors are anti-correlated with the SNR. We note that these errors also account for any potential cases where the spatial order of velocity slabs may not be ordered correctly along a line of sight.

2.3.3 Identifying Velocity Coherent Filaments

Velocity gradient analyses are only useful for understanding gas flows if the structures being analyzed are velocity-coherent, i.e., continuous in velocity. Velocity slabs derived from our fits must therefore be sorted into velocity-coherent structures prior to such analyses. In this sub-section, we present methods to reconstruct fits to our data as simple emission line models in position-position-velocity (i.e., ppv) space without hyperfine structures. We further present methods to identify filament spines from these models in ppv space and sort the fitted slabs into velocity-coherent filaments based on these identified spines.

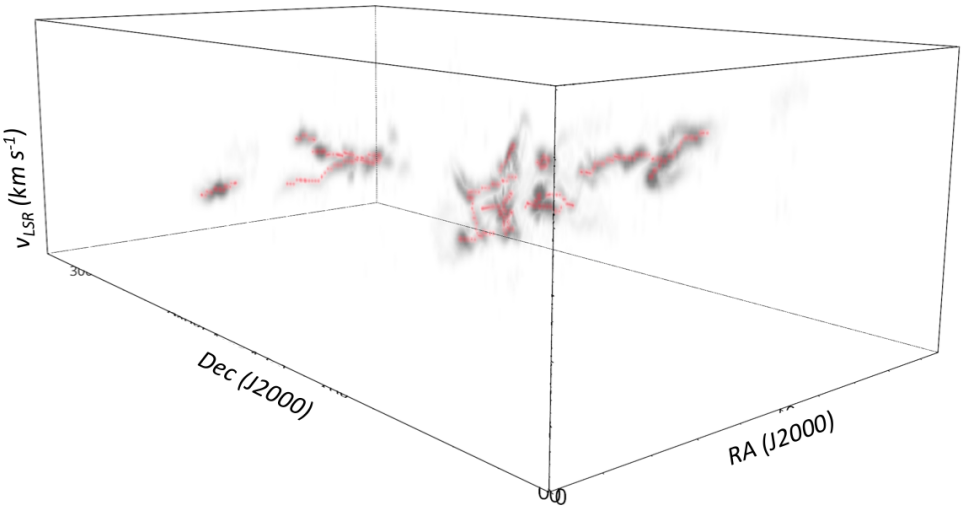

Figure 2.5: The debelended ppv cube of NGC 1333 reconstructed from the best fit models (grey), and the filament spines identified from the cube using CRISPY (red).

Reconstructing velocity structures

To help identify velocity coherent structures in ppv space, we first reconstruct our best fit models with the hyperfine structures removed to avoid confusion from these non-kinematic features. Such a reconstruction, known as "deblending," is accomplished by computing the spectral profile of each gas slab using a single Gaussian τ_ν profile based on our best fit model, which accounts for all 18 hyperfine structures (see Section 2.2.1). In other words, we reconstruct the spectral profile along a line of sight with either one or two Gaussian τ_ν components using our best fit parameters and number of components as determined by the AICc criterion.

Since our τ_0 value derived from a fit (see Eq. 2.1) represents the peak optical depth of all the NH_3 (1,1) hyperfine lines combined, we scale down our fitted τ_0 by a factor of 10 to represent better the actual optical depths of individual hyperfine groups in our reconstruction. For reference, the main and satellite hyperfine groups each contain about 50% and 10% of the optical depth represented by τ_0, respectively. The observed satellite lines are thus typically optically thin even when the main hyperfine lines are not, which enables these thin lines to reveal unobstructed structures along lines of sight.

We further assume each deblended velocity component is optically thin with respect to each other but not with respect to the CMB, individually. Our deblended

model, with the CMB subtracted as a constant baseline, can thus be expressed as,

$$I_\nu = \sum_{j=i}^{m} \left[B_\nu(T_{ex,j}) - B_\nu(T_{\rm CMB})\right] \left[1 - e^{-\tau_{\nu,j}}\right], \tag{2.5}$$

where j designates each velocity component along a line of sight and $\tau_{\nu,j}$ is governed by,

$$\tau_{\nu,j} = 0.1\ \tau_{0,j} \exp\left[\frac{-(v - v_{{\rm LSR},j})^2}{2\sigma_{v,j}^2}\right]. \tag{2.6}$$

Here, $T_{ex,j}$, $\tau_{0,j}$, $v_{{\rm LSR},j}$, and $\sigma_{v,j}$ are obtained from previously fitted models with hyperfine structures. To ensure the deblended emission have high spectral acuities for structure identification in ppv space, we further set $\sigma_{v,j}$ to 0.09 km s^{-1} instead of adopting the line widths previously derived from our fits. This constant σ_v value is roughly the minimal line width required to be Nyquist-sampled at our 0.07 km s^{-1} full-width-half-max (FWHM) spectral resolution.

To illustrate structures revealed by deblending, Figure 2.5 shows the volume-rendered deblended ppv cube of our fits to the NH_3 (1,1) observations of NGC 1333.

Identifying filaments

We identify filaments in ppv space by using a multi-dimensional density ridge identification algorithm known as the Subspace Constrained Mean Shift (SCMS) (Ozertem & Erdogmus, 2011). The mathematical framework behind SCMS was generalized by Chen et al. (2014) to operate on weighted, particle-like data in addition to their unweighted counterparts, which enables SCMS to run on gridded, multi-dimensional images. Since the publicly available `R` code developed by Chen et al. (2015) for cosmological applications only implemented the original framework, we modified the code to reflect the generalized one. We further translated the code to `Python`, parallelized it for multi-processing, and made it publicly available on *GitHub* via the CRISPy[ii] (i.e., Computational Ridge Identification with SCMS for Python) package under a GNU General Public License. The version of CRISPy we used in this paper is archived in Zenodo (Chen, 2020b).

While the DisPerSE algorithm (Sousbie 2011; Sousbie et al. 2011) recently used in star formation studies (e.g., Arzoumanian et al. 2011) also operates in 3D (e.g., Smith et al. 2016), it requires two more user-defined parameters to run than SCMS.

[ii] `CRISPy` codebase: https://github.com/mcyc/crispy.

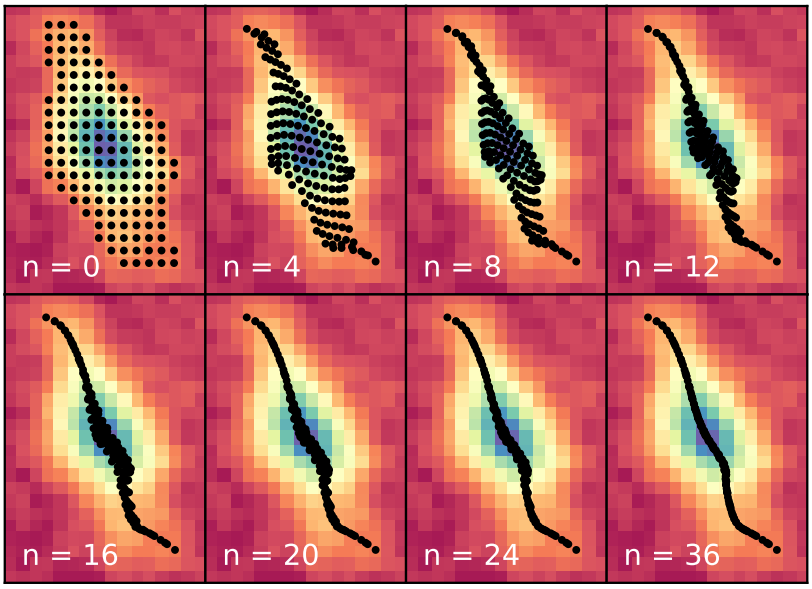

Figure 2.6: Snapshots of SCMS finding a 2D 'density' ridge from the image shown in the background, as carried out by CRISPy. The respective iteration number for each snapshot is labelled in each panel. The black dots represent the SCMS walkers and the background image was taken from the integrated NH_3 emission map of NGC 1333, cropped around a source in its north-east.

The SCMS' ability to find density ridges consistently is also well established in statistical studies (Chen et al. 2014), making SCMS an attractive option over other methods. Furthermore, SCMS captures local information, such as ridge orientations, better than methods that derive ridges from monolithic filament objects (e.g., Koch & Rosolowsky 2015) or approximate them as line segments (Hacar et al. 2013, 2017).

The SCMS algorithm defines a ridge as a smooth, continuous, one-dimensional object in a multi-dimensional density field. In addition to this nomenclature, we define a skeleton as a ridge that has been gridded onto an image and a spine as a skeleton with all its branches removed. The SCMS algorithm finds ridges by moving walkers iteratively up the density field using a gradient ascent method. This approach is subspace constrained (see Chen et al. 2014) to ensure the walkers converge on one-dimensional ridges instead of zero-dimensional peaks. Figure 2.6 demonstrates how SCMS identifies such a ridge in 2D from an NH_3 integrated intensity map of a source in NGC 1333 using the CRISPy package.

In general, the SCMS algorithm operates primarily on two user-defined param-

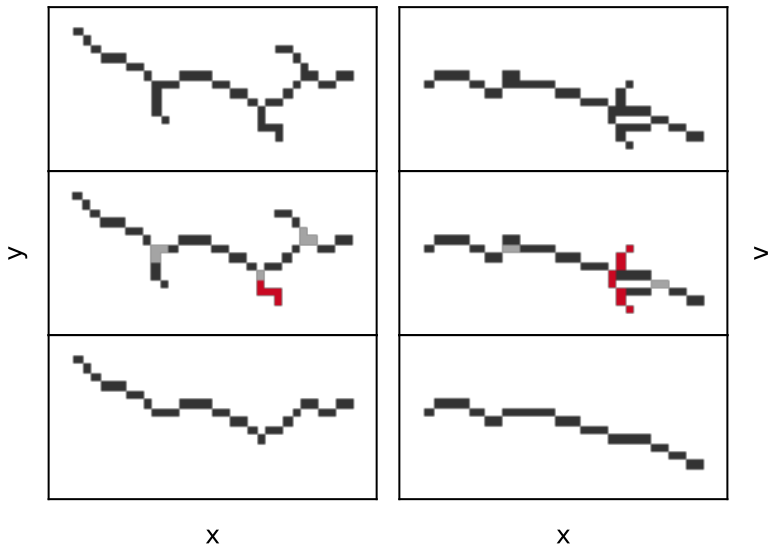

Figure 2.7: A gridded, 3D skeleton being pruned into a spine, projected onto the xy and xv planes on the left and right panels, respectively. Top: the skeleton prior to pruning. Middle: the skeleton decomposed into branches (black), intersections (grey), and 'bad' branches (red; see Section 2.3.3). Bottom: the resulting spine, defined by the longest path in the skeleton with 'bad' branches excluded.

eters: density (e.g., intensity) threshold and smoothing bandwidth. The density threshold masks out noisy features in the density field while the smoothing bandwidth performs a kernel estimate of the field from particle-like data. Even though a gridded image, e.g., an emission cube, can in principle serve directly as a density field without a kernel estimate, a smoothing kernel is still required by the generalized SCMS to estimate density gradients efficiently and move its walkers accordingly (Chen et al., 2014). A smoothing length comparable to, or greater than, the resolution of the image is thus required still.

For this work, we adopted a density threshold of 0.15 K and a smoothing length of 1.5 pixels for our SCMS run with CRISPy. The deblended cube was spatially convolved to twice its original beam width prior to the run. This additional step was performed to suppress noisy features further in the cube without sacrificing spectral resolution, particularly given that SCMS smooths its data indiscriminately in all three dimensions. Since SCMS operates natively in a continuous space, we set our convergence criterion such that the ridges identified are less than one voxel in width prior to re-gridding. We describe details on our choice of parameters further in Appendix A.1.

Once CRISPy identified emission ridges in the continuous ppv space, we map these ridges back to the native grid of the deblended cube. These re-gridded ridges are referred to as skeletons and are subsequently pruned down to branchless structures we call spines. We accomplish such a pruning by using a graph-based technique developed by Koch & Rosolowsky (2015), which we have generalized to operate in 3D.

We prune branches by first decomposing a skeleton into intersection and branch objects known as nodes and edges in graph theory, respectively. We then find the longest path in the graph, measured in Euclidean distance, and subsequently remove all the edges outside of this path. To ensure our spines represent velocity-coherent structures, branches that may bridge velocity-discontinuities are further removed. We define these 'bad' branches as ones with an on-sky length less than 9 pixels and a velocity projected length greater than that of its on-sky length in pixels (i.e., ~ 4.8 km s^{-1} pc^{-1} for NGC 1333 with our data). Figure 2.7 shows a demonstration of our pruning process with 'bad' branches shown in red. We note that removing 'bad' branches does not necessarily impose a maximum velocity gradient limit on a filament. This process merely breaks filaments apart.

Assigning Membership to Filaments

We group our fits-derived velocity slabs obtained with MUFASA into velocity coherent structures by associating them with filament spines. In brief, we do so hierarchically by first placing velocity slabs into structures we call associations based on each slab's proximity to a spine in the ppv space. Such proximity is calculated using a spatial extension of a spine we call ppv-footprint, a structure for which the $v_{\rm LSR}$ separation between a slab and a spine can be referenced from at each pixel. This first step intends to disentangle filaments that overlap in projection into associations.

Associations, which are allowed to have more than one velocity slab at each pixel, are then sorted internally to produce velocity coherent structures (vc-structures) that contain only a single slab at a pixel. This sortation is carried out based on kinematic similarities between the velocity slabs. The $v_{\rm LSR}$ map resulting from this sortation is subsequnetly median smoothed and adopted as the new ppv-footprint. This last step serves to grow and update the association iteratively starting from the filament spine, one pixel at a time.

We repeat such an assignation and sortation for five iterations. This number of

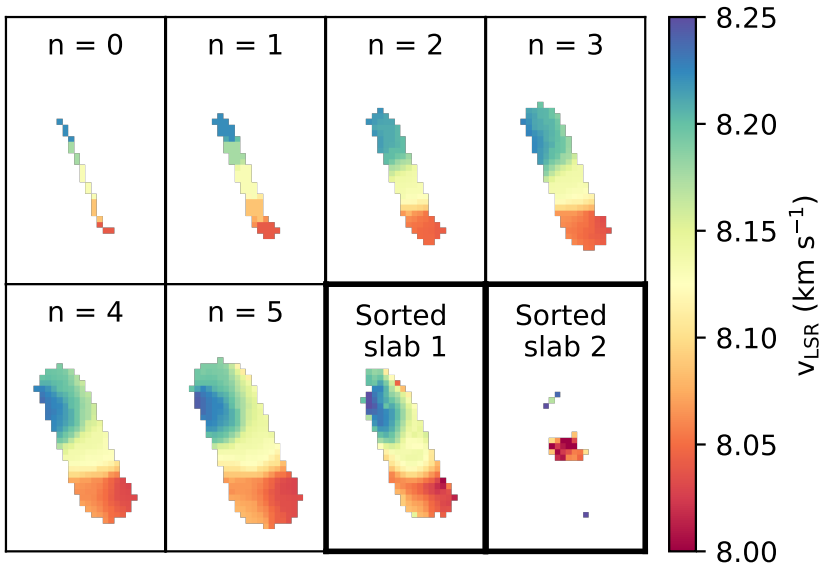

Figure 2.8: A ppv-footprint during each iteration of its creation, shown in panels labelled with the iteration number n. The v_{LSR} maps of the sorted velocity slabs, which have been assigned to the final ppv-footprint (n=5) as members of an association based on their v_{LSR} proximities, is shown in the last two panels, framed with bold borders. Only the first velocity slab represents a velocity coherent structure we used for our velocity gradient analyses.

iterations grows our vc-structures to an extent where SNR values of the new pixels start to drop off below 3. Figure 2.8 shows ppv-footprints corresponding to each of these iterations in panels labeled with the iteration number n. The v_{LSR} maps of the first and second velocity slabs in the final association are shown in the last two panels of Figure 2.8. This first velocity slab shown in the figure is representative of those that go into our final vc-structures, which are used in our velocity gradient analyses. Further details of our membership assignment to vc-structures are described in Appendix A.2.

2.3.4 Velocity Gradient Analysis

Decomposition of Vector Fields

To study gas motions geometrically with respect to filament spines, we devised a technique to decompose a vector field (e.g., the velocity gradient field) into orthogonal components that are either parallel or perpendicular to a filament spine. Such a decomposition is accomplished by first taking a distance transform of a sky-projected

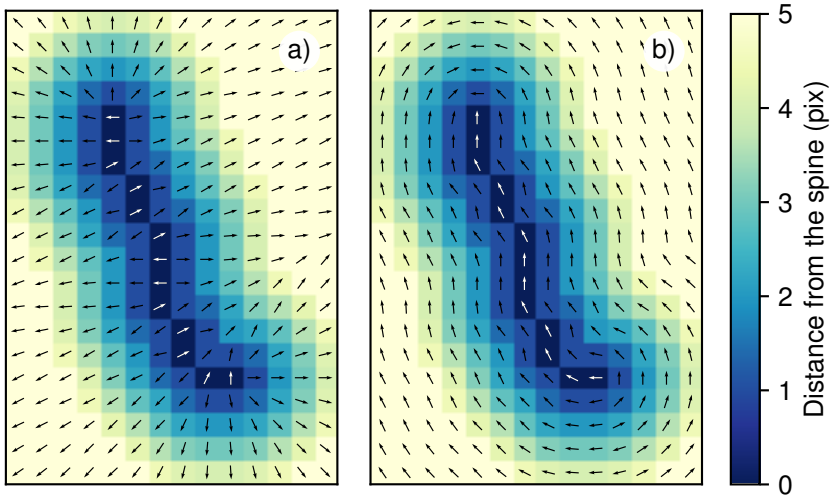

Figure 2.9: Distance transform of a filament spine overlaid with its corresponding a) divergence field and b) parallel field. The vectors on and off the spine are colored white and black, respectively. The color scale corresponds to pixel distances between 0 and 5.

spine to map out the shortest Euclidean distance between a given pixel and the spine. In other words, we calculated the radial distance between a pixel and a spine from which radial profiles of filaments can be constructed.

Vector-fields that point orthogonally away from the filament spines are then created by taking gradients of our distance transforms over a sampling distance of 1 pixel using the second-order accurate central differences method. We refer to these fields as the divergence fields. Figure 2.9a shows an example of a divergence field superimposed on its corresponding distance transform.

Due to the sampling method of the gradient calculation and symmetry, the divergence field vectors right on the spine often have magnitudes of zero. To avoid a loss of information due to this limitation, we reconstructed an on-spine vector field parallel to the spine by taking gradients, i.e., central differences, of the spine's pixel coordinates. This on-spine field is then rotated by 90° and inserted into the divergence-field, as shown in Figure 2.9a in white.

We construct the corresponding parallel field of a filament by rotating the divergence field by 90°. Since the divergence field is discontinuous across the spine, where its vectors point oppositely away from each other, a uniform rotation of the divergence field will result in a discontinuous parallel field, where its vectors are anti-

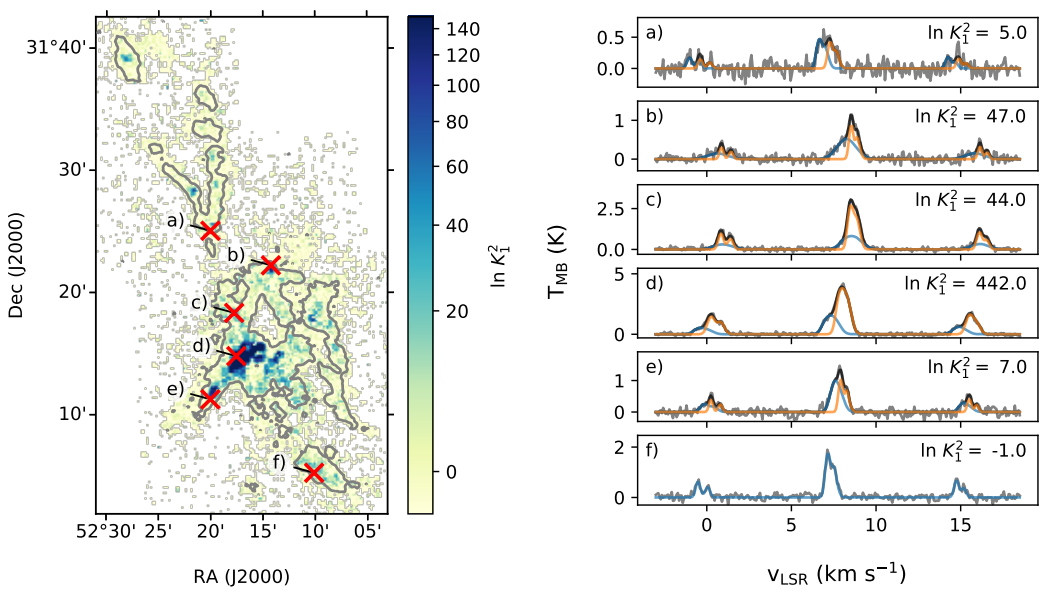

Figure 2.10: Left panel: relative likelihood of the two-slab fit over its one-slab counterpart in NGC 1333. The grey contour shows the integrated NH_3 (1,1) emission at the 0.35 K km s^{-1} level. Right panel: the observed NH_3 $(1,1)$ spectra (grey) extracted from the positions marked with red x's shown in the left panel, cropped to focus on the spectral regions near the main hyperfine lines. The spectra are superimposed with their corresponding two-slab fits (black) and models of their individual components (blue and orange).

aligned with respect to each other across the spine. To address this issue, we rotated the divergence field vectors on each side of the spine independently in the directions opposite to each other. Such a rotation is accomplished by exploiting angular degeneracy in the arctan function to differentiate vectors on the two sides of the spine. Figure 2.9b shows an example of a parallel-field overlaid on the distance transform of its corresponding spine.

Computing Velocity Gradients

We calculate $v_{\rm LSR}$ gradients, i.e., $\nabla v_{\rm LSR}$, from $v_{\rm LSR}$ maps of velocity-coherent structures determined with the methods described in Section 2.3.3. These gradients are calculated on a pixel-by-pixel basis by fitting a plane over pixels within a 6-pixel diameter aperture centered on them. The diameter of the plane-fitting aperture is explicitly chosen to be twice the size of our FWHM beam to ensure the velocity gradients are calculated over resolved structures. To ensure the quality of our calculations,

we calculate $\nabla v_{\rm LSR}$ only over apertures where $v_{\rm LSR}$ values are available for more than 1/3 of the pixels.

We further decompose the calculated $\nabla v_{\rm LSR}$ fields into components that are perpendicular and parallel with respect to its associated filament spine. This decomposition is accomplished by taking the dot products between the $\nabla v_{\rm LSR}$ field and the divergence field, as well as between the $\nabla v_{\rm LSR}$ field and the parallel field (see Section 2.3.4).

2.4 Results

Earlier in Section 2.3.2, we presented the performance of our fitting method, MUFASA, as characterized by our test fits to synthetic spectra. Here we present our best fit models to the GAS NH_3 (1,1) observations of NGC 1333 in Section 2.4.1, along with the deblended emission reconstructed from these fits. The filament spines identified from the deblended emission by CRISPy and the velocity slabs assigned to these spines are also presented in the same subsection. We further present our velocity gradient analysis on these velocity-coherent filaments in Section 2.4.2.

2.4.1 NGC 1333 - Fitted Models

Figure 2.10 shows the relative likelihood of the two-slab fit over the one-slab fit, i.e., K_1^2, in NGC 1333 as determined by the AICc (see Section 2.2.1). A significant fraction, i.e., 40%, of the pixels in NGC 1333 with SNR > 3 are determined to be better fitted with two-slab models based on the statistically robust threshold of $\ln K_1^2 > 5$ (Burnham & Anderson, 2004). This fraction is significantly higher than that suggested by the GAS DR1 paper (Friesen et al., 2017), where when examined by eye, only 5% or less of the pixels with SNR > 3 appears to be inadequately fitted by a one-component model. No pixel best fitted with our two-slab model has $\chi_\nu > 1.5$, which indicates that our observations of NGC 1333 are indeed well modelled with two or fewer velocity slabs.

The right panel of Figure 2.10 shows examples of our best fits to the NH_3 $(1,1)$ emission, superimposed on spectra extracted from positions marked in the left panel. It is qualitatively apparent that these spectra are indeed better fitted by two component models when $\ln K_1^2 > 5$, even in the limiting case where $\ln K_1^2$ is near 5.

The deblended ppv cube of NGC 1333 derived from our best fit models is shown

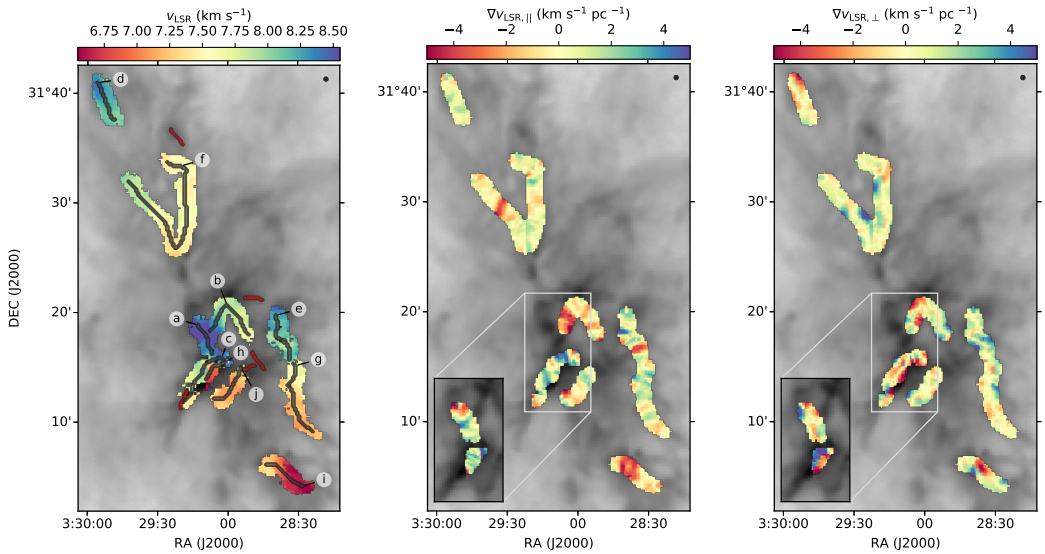

Figure 2.11: Left panel: projections of filament spines identified in NGC 1333, overlaid on top of the $v_{\rm LSR}$ maps of selected velocity-coherent filaments (color). Spines less than 15 pixels in length are colored in red and their associated filaments are excluded from our analysis. Centre and right panels: spatial distribution of the parallel and perpendicular components of $\nabla v_{\rm LSR}$, respectively, relative to their filament spines. The call-out boxes in these panels show the same $\nabla v_{\rm LSR}$ components of the additional, overlapping velocity-coherent filaments in the sky. The FWHM beam of the NH_3 (1,1) data (black circle) and the *Herschel* $N(H_2)$ map (grey; A. Singh et al., in prep.) are shown on the top right corner and the background of each panel, respectively.

earlier in Figure 2.5, overlaid with their respective spines identified by CRISPy. The left panel of Figure 2.11 shows these spines projected onto the sky, and overlaid on top of the $v_{\rm LSR}$ maps of selected vc-structures, which are further overlaid on top of the *Herschel* derived $N(H_2)$ map (A. Singh et al., in prep). All the spines identified are used to sort fitted slabs into vc-structures, but only vc-structures with spines longer than 15 pixels in length ($\sim$ 6 beam widths) are considered filaments in our analysis. In NGC 1333, we identified 10 velocity-coherent filaments in total, and have labeled them alphabetically from *"a"* to *"j"* in Figure 2.11.

2.4.2 NGC 1333 - Velocity Gradients

The center and right panels of Figure 2.11 show, respectively, the spatial distribution of perpendicular and parallel components of velocity gradients ($\nabla v_{\rm LSR}$) in the NGC 1333 filaments. These filaments display a wealth of $\nabla v_{\rm LSR}$ structures within them.

A large fraction of these pixels have values of $|\nabla v_{\rm LSR}| > 2$ km s^{-1} pc^{-1} in both components, with many of them exceeding 4 km s^{-1} pc^{-1}.

At our sampling distance of two-beam widths ($\sim$ 0.06 pc in NGC 1333), our measured velocity gradients appear consistent with those median values reported by Hacar et al. (2013) in NGC 1333, measured with N_2H^+ in the parallel direction on the same spatial scale. Similarly, Lee et al. (2014a) also reported comparable values in Serpens Main, measured in the parallel direction for filaments with mass ~ 4 M$_\odot$. Parallel gradients measured on larger scales (> 0.2 pc), however, tend to have smaller values. For example, the Serpens South filaments (Kirk et al. 2013a; Fernández-López et al. 2014) and the Serpens Main filaments with masses of ~ 15 M$_\odot$ (Lee et al. 2014a) all have larger-scale parallel gradients ≤ 1.5 km s^{-1} pc^{-1}.

2.5 Discussion

2.5.1 Comparing with N_2H^+ Analysis of NGC 1333

Hacar et al. (2017), hereafter H17, conducted a multi-component spectral analysis of NGC 1333 with a dense gas tracer, i.e., N_2H^+ (1-0) lines. Their data have a spatial and spectral resolution (30" and 0.06 km s^{-1}, respectively) similar to our NH_3 (1,1) data, and a typical rms noise of 0.15 K, which is about 50% higher than ours. H17 fitted their observations with a semi-automatic method, using either one- or two-component models as determined by eye.

About 15% of the spectra successfully fitted by H17 are fitted with a two-component model. Considering not all of these successfully fitted spectra have SNR > 3, we estimate upwards to about 20% of those spectra with SNR > 3 are fitted with two-component models. This estimate assumes all the successful two-component fits have SNR > 3 in this limit. This 20% fraction is significantly lower than that of our NH_3 (1,1) fits, where two-component models best fit about 40% of our spectra with SNR > 3. The difference in the model-selection criteria between our method (MUFASA) and that of H17 may contribute predominantly to this reported difference, where the conservative $\Delta v_{\rm LSR}$ threshold adopted by H17 may have culled out a significant fraction of their two-component fits.

Figure 2.12 shows the f_σ and $\Delta v_{\rm LSR}$ values derived from two-slab fits in NGC 1333 plotted against each other. The colored contours in the background show the kernel density estimate of this scatter plot. The filled curves to the right and the top of the

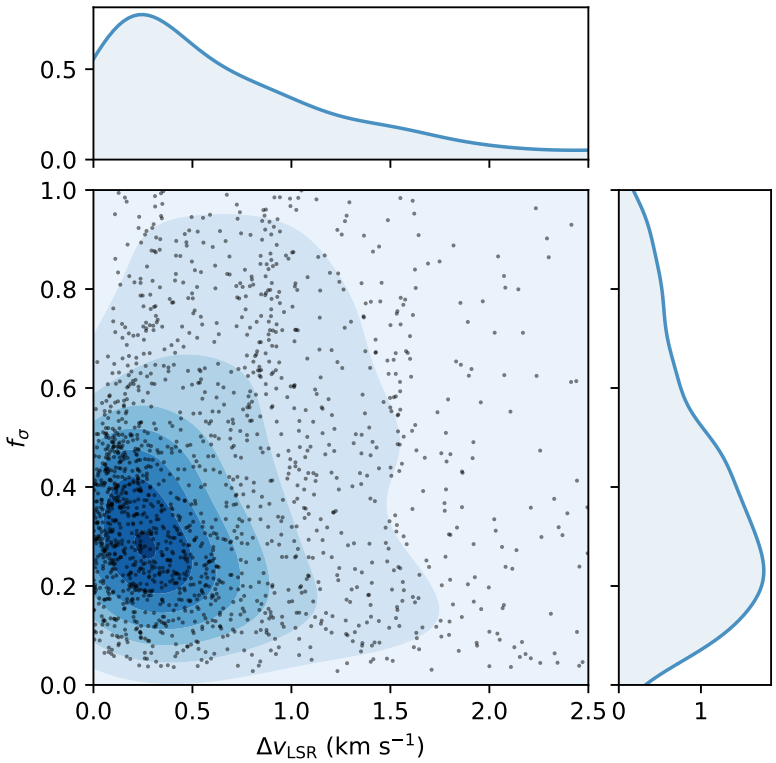

Figure 2.12: The ratio between the fitted line widths of two velocity slabs (i.e., f_σ), plotted against velocity separation between these slabs ($\Delta v_{\rm LSR}$) for successful fits in NGC 1333. The colored background shows the contours of a kernel density estimate (KDE) while the filled curves to the top and the right show the 1D KDE distributions of f_σ and $\Delta v_{\rm LSR}$, respectively.

plot show the 1D kernel estimated distributions of f_σ and $\Delta v_{\rm LSR}$. Most of the points on this plot cluster around f_σ and $\Delta v_{\rm LSR}$ values of 0.3 and 0.25 km s^{-1}, respectively. This clustering places these values in the regime where the true-positive identification rate for two-slab spectra is in the range of $\sim 70 - 90\%$ according to our truth test shown in Figure 2.3b, accounting for all SNR values found in our synthetic test set. Given that MUFASA's performance at identifying two-slab spectra decreases towards higher f_σ values and lower $\Delta v_{\rm LSR}$ values, the true peak of the underlying two-slab population likely sits higher on the f_σ axis and lower on the $\Delta v_{\rm LSR}$ axis. We reiterate that MUFASA only misidentifies a one-slab spectrum as a two-slab spectrum in $< 4\%$ of the test cases for all SNR values.

About 40% of our two-slab fits to spectra with SNR > 3 in NGC 1333 have $\Delta v_{\rm LSR}$

values that are less than 0.25 km s^{-1}, the threshold used by H17 to determine whether or not additional components are justified for their fits to N_2H^+ (1-0) observations of the same region. If NH_3 (1,1) and N_2H^+ (1-0) indeed trace the same gas population in this region, then the fraction of dense gas spectra in NGC 1333 with multiple velocity-components and SNR > 3 may be significantly underreported by H17 due to their choice of $\Delta v_{\rm LSR}$ threshold. Given that two-slab identification with MUFASA is successful even with moderate SNR values (i.e., 5 - 20; see Fig. 2.2), the actual number of two-slab spectra with SNR > 3 is likely higher than those reported in both the H17 study and our study here.

The NH_3 (1,1) and N_2H^+ (1-0) lines have critical densities of $\sim 2 \times 10^3$ cm^{-3} and $\sim 5 \times 10^4$ cm^{-3}, respectively, at gas temperatures $\lesssim 20$ K (Shirley 2015). The ratio between these critical densities remains similar even at higher temperatures. If the second velocity-component detected in our study tends to trace more diffuse gas, then the difference between the reported fraction of multi-component spectra between this work and that of H17 may be due to density differences in the tracers themselves in addition to the line-fitting methods used. The sensitivity difference between our data and that of H17 may also play a role as well.

A recent high angular-resolution study of NGC 1333 concluded that NH_3 (1,1) and N_2H^+ (1-0) trace the same gas population well (Dhabal et al., 2019). Since this study only fits one velocity component along each line of sight, however, it is unclear how robust their conclusion is. Further investigation on how well NH_3 (1,1) and N_2H^+ (1-0) trace each other in NGC 1333 is thus needed, particularly for diffuse emission to which the data of Dhabal et al. (2019) are less sensitive.

The filament spines we identified from our NH_3 data with CRISPy (see Figure 2.11, left) are morphologically similar to the 'filament axes' identified by H17 with N_2H^+ observations. Some of the longer filaments, however, are 'split' differently. Our filament *f*, for example, is split into filaments *12* and *14* by H17, while our filament *g* is split into filaments *1* and *2* by H17. Moreover, we identify a kinematically distinct filament (i.e., *h*) that was not identified earlier by H17, which runs closely parallel to our filament *c* (i.e., *10*).

Even though the spatial separation between spines of filament *c* and *h* is only slightly resolved in our data, the spectral separation of these spines (~ 0.9 km s^{-1}) is well resolved. When observed at higher spatial resolutions with NH_3 and N_2H^+ (Dhabal et al., 2019), these two filaments can be seen by eye as distinct structures. Filament *h* is thus likely missed by H17 due to their approach rather than observa-

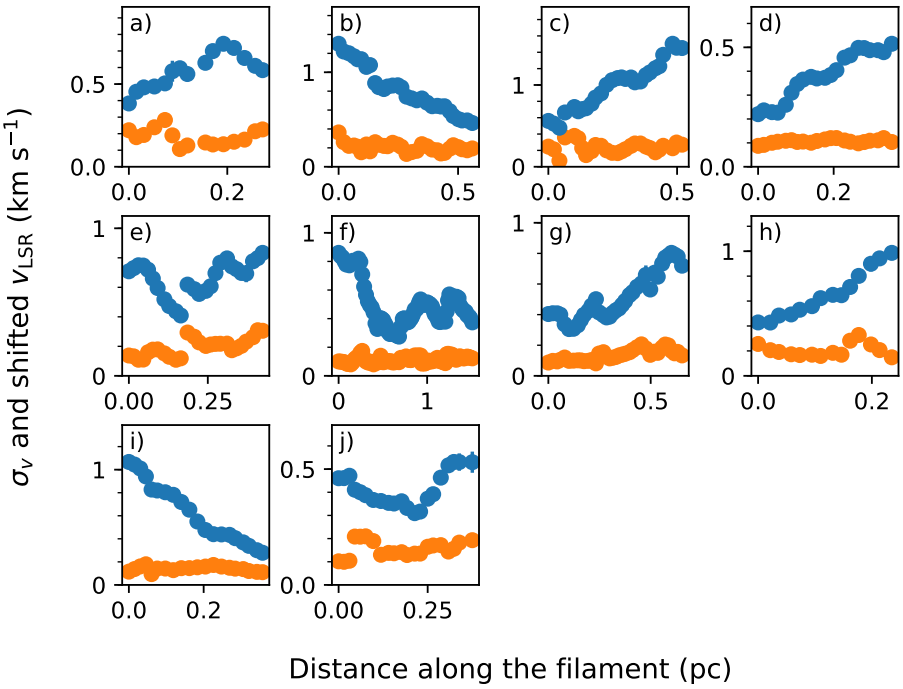

Figure 2.13: The profiles of σ_v (orange dots) and $v_{\rm LSR}$ (blue dots) along filament spines identified in NGC 1333. The $v_{\rm LSR}$ shown here have been shifted to fit on the same axes as σ_v.

tional biases introduced by the tracers used.

2.5.2 Velocity Gradients on Large Scales

Figure 2.13 shows 1D $\sigma_{\rm v}$ and $v_{\rm LSR}$ profiles of the filaments identified in NGC 1333, taken directly from the pixels on their spines. The $v_{\rm LSR}$ values displayed in Figure 2.13 have been the zero-point shifted arbitrarily from the local standard of rest (i.e., LSR) to fit nicely on the same axes as the $\sigma_{\rm v}$. We note that these spine profiles run in the direction that starts on the ends closest to the map origin, i.e., the south-eastern corner.

The $v_{\rm LSR}$ variations along these spines are generally smooth with respect to their estimated errors. Only a few discontinuities are found in these profiles. Such a lack of discontinuity suggests that CRISPy does indeed identify density ridges robustly as continuous structures, which form the basis of our membership assignment to velocity-coherent filaments.

The $v_{\rm LSR}$ values shown in Fig. 2.13 do vary significantly along most of the identified filaments. Many of the $v_{\rm LSR}$ profiles are approximately linear and monotonic on scales larger than 0.2 pc, and have velocity gradients typically in the range of 0.8 - 2.5 km s^{-1} pc^{-1} on those scales. The large-scale ($>$ 0.2 pc) velocity gradients are similar to those found with N_2H^+ observations in NGC 1333 ($\sim$ 0.5 - 2.5 km s^{-1} pc^{-1}, Hacar et al. 2017) and the Serpens South SF region (1.4 km s^{-1} pc^{-1}, Kirk et al. 2013a; $\sim$ 1 km s^{-1}pc^{-1}, Fernández-López et al. 2014). These gradients also fall within the range measured in the Serpens Main SF region (0.7 - 4.8 km s^{-1} pc^{-1}, Lee et al. 2014a).

Velocity gradients along filaments on a large scale have often, but not uniquely, been interpreted as signatures of mass flow towards a star-forming core or cores (e.g., Kirk et al. 2013a). While dense structures in NGC 1333 do not necessarily display a classical "hub and spokes" geometry, over-densities of dense cores and Class 0/I YSOs, as estimated by Hacar et al. (2017), are often found at the ends of our filament spines in projection. Filaments c and h, for example, have very linear $v_{\rm LSR}$ profiles and large-scale $\nabla v_{\rm LSR}$ values of roughly 1.9 km s^{-1} pc^{-1} and 2.5 km s^{-1} pc^{-1}, respectively. The fact that the north-western ends of these filaments coincide with the most prominent peak of over-densities in NGC 1333, in the SVS 13 vicinity (see Walawender et al. 2008), suggests these filaments are indeed transporting gas along their lengths towards a small (i.e., $n < 10$) cluster/proto-cluster.

While filament b has no end that correlates with an over-density of dense cores and Class 0/I YSOs, it does have an over-density midway through its length, located at the apex of its sharp turn near the HH 12 IR sources (i.e., VLA 42; see Walawender et al. 2008). Remarkably, this filament has a very linear and continuous $v_{\rm LSR}$ profile despite having such a distinct bend in its middle. Considering that this profile has a large-scale $\nabla v_{\rm LSR}$ of 1.4 km s^{-1} pc^{-1}, filament b is likely a velocity-coherent system of two filaments that are transporting material towards a small hub.

Interestingly, the $\nabla v_{\rm LSR}$ seen on the largest scale of our observation ($\sim$ 4 pc), i.e., at the clump scale, also appears to be fairly ordered along the north-south direction. Nearly all the filaments featuring linear $v_{\rm LSR}$ profiles along their spines have $v_{\rm LSR}$ values that increase northwards. Filament b is the only exception, where half of its western segment prior to its sharp bend has $v_{\rm LSR}$ values that increase southwards instead. Even though filament f does not have an overall linear $v_{\rm LSR}$ profile, its western portion prior to its sharp bend does have a segment, $\sim$ 0.2 pc in length, with a fairly linear $v_{\rm LSR}$ profile and a $\nabla v_{\rm LSR}$ of $\sim$ 2.5 km s^{-1} pc^{-1}. The $v_{\rm LSR}$ values of this segment increase northwards as well.

In addition to the prevalent trend that $v_{\rm LSR}$ increases northward in most filaments, the median $v_{\rm LSR}$ value of each filament tends to increase northwards across the NGC 1333 clump as well. Considering that NGC 1333 is relatively elongated in the north-south direction on the clump scale ($>$ 4 pc; see map by Sadavoy et al. 2012 for example), most of these filaments may trace a larger filamentary inflow like those assumed by Matzner & Jumper (2015) in their model, of which these smaller filaments may be a part.

2.5.3 Velocity Gradients on Small Scales

Parallel Components

In addition to well-organized velocity structures on larger scales, Figures 2.11 and 2.13 reveal many quasi-oscillatory $v_{\rm LSR}$ structures that can be found on the 0.1 pc ($\sim$ 3 beam widths) scale in NGC 1333. This behaviour is prominently visible along the spines of many filaments (see Figure 2.13) and shows up in the parallel $\nabla v_{\rm LSR,\parallel}$ map (see Figure 2.11, center) as "zebra stripes." These small-scale structures, e.g., gradient peaks and dips, also appear to be somewhat evenly spaced by $\sim$ 0.1 pc, which suggests a quasi-oscillatory wavelength of $\sim$ 0.2 pc. Interestingly, this behaviour is not confined to the spines of filaments and extends spatially across the width of a filament.

Similar quasi-oscillatory $v_{\rm LSR}$ behaviours have been found in Taurus L1495/B213 (Tafalla & Hacar 2015) and in Serpens South filaments (Fernández-López et al. 2014) based on one-component fits to N_2H^+ (1-0) observations. Filaments and fibres identified from multi-component fits to $C^{18}O$ (1-0) observations in Taurus-Auriga L1517 (Hacar & Tafalla 2011), and Taurus L1495/B213 (Hacar et al. 2013), respectively, also showed similar results. These quasi-oscillatory $v_{\rm LSR}$ behaviours generally resemble those seen in synthetic $C^{18}O$ observations of simulated filaments, constructed with various degrees of realism (e.g., Moeckel & Burkert 2015; Smith et al. 2016; Clarke et al. 2018a).

We find no strong spatial correlations between quasi-oscillatory $v_{\rm LSR}$ and dense structures in NGC 1333. This result is contrary to that found in Taurus-Auriga L1517 (Hacar & Tafalla 2011) using $C^{18}O$ observations but agrees with the behaviour found in Taurus L1495/B213 (Tafalla & Hacar 2015) using N_2H^+ (1-0) observations. This agreement extends to synthetic $C^{18}O$ observations of simulations (e.g., Smith et al. 2016). The lack of correlation between quasi-oscillatory $v_{\rm LSR}$ values and dense

structures suggests the former is not driven by periodic gravitational instabilities. Alternative mechanisms, such as magnetic waves explored by Tritsis & Tassis (2016), Tritsis & Tassis (2018), and Offner & Liu (2018), may be responsible for these quasi-oscillatory behaviours.

Perpendicular Components

Filaments in NGC 1333 also contain a wealth of perpendicular velocity gradients, i.e., $\nabla v_{\mathrm{LSR},\perp}$, structures on smaller scales (see right panel of Fig. 2.11). Regions with high $|\nabla v_{\mathrm{LSR},\perp}|$ values (> 2 km s^{-1} pc^{-1}) tend to form spatially compact but resolved $\nabla v_{\mathrm{LSR},\perp}$ structures on the outskirts of the filaments, i.e., away from the spine. Similar to interpretations made in the literature (e.g., Palmeirim et al. 2013; Dhabal et al. 2018), these compact $\nabla v_{\mathrm{LSR},\perp}$ structures may be indicative of recent or ongoing accretion of nearby gas onto the filaments.

Free-fall accretion in analytic models typically has estimated infall velocities of a few km s^{-1} at filament 'boundaries' (e.g., Palmeirim et al. 2013; Heitsch 2013). Such an infall velocity will likely result in shocks if the accreting filament is in hydrostatic equilibrium like those described in classic models (e.g., Stodólkiewicz 1963; Ostriker 1964). Even in numerical models for which filaments are not equilibrium substructures, shock-induced discontinuities in velocities are expected from accretion (e.g., Clarke et al. 2018a).

We neither saw nor expected velocity discontinuities in our filaments because velocity-coherent structures are continuous in their velocities by definition. Velocity discontinuities, however, can be inferred from the Δv_{LSR} observed between velocity slabs along a line of sight. With the exception of filaments c and h, which have typical Δv_{LSR} values of ~ 0.8 km s^{-1} between them, we did not find filaments with overlapping velocity slabs that had Δv_{LSR} values greater than 0.4 km s^{-1}, i.e., about twice the isothermal sound speed at 10 K. Interestingly, the region where filaments c and h overlap along lines of sight is also where some of the most prominent $\nabla v_{\mathrm{LSR},\perp}$ structures are found in NGC 1333. We note that this observed $\nabla v_{\mathrm{LSR},\perp}$ structure is unlikely driven by the highly collimated outflow originated from IRAS 4 (e.g., Blake et al. 1995) given that it poorly aligns with the orientation of the outflow.

Except for where filaments overlap in projection, we typically only detect two-slab spectra near filament spines rather than the edges. This lack of detection near the edges is likely limited by the sensitivity of our data. Not much information

is therefore available on $\Delta v_{\rm LSR}$ over filament edges to infer the nature of spatially compact $\nabla v_{\rm LSR,\perp}$ structures that reside there. Furthermore, despite having a critical density of 10^3 cm^{-3}, it remains unclear how effective NH_3 is at tracing accretion flows, which themselves are likely more diffuse than the dense filaments. Further investigation with NH_3 synthetic observations, similar to that conducted by Clarke et al. (2018a) with $C^{18}O$ transitions, would be highly valuable.

To search for potential sources of accretion flows, we looked for structures around our filaments in the column density, i.e., $N(H_2)$, map of NGC 1333 derived from *Herschel* observations (A. Singh et al., in prep). We find no strong spatial correlation, however, between ambient *Herschel* structures (e.g., sub-filaments) and the observed $\nabla v_{\rm LSR,\perp}$ structures. This lack of correlation suggests that accretion from sub-filaments, such as those seen in Taurus B211/B213 (Goldsmith et al. 2008, Palmeirim et al. 2013), is unlikely to explain the origin of the compact $\nabla v_{\rm LSR,\perp}$ structures seen near filament edges.

Nevertheless, the lack of visible, interconnected ambient structures does not necessarily rule out $\nabla v_{\rm LSR,\perp}$ as a sign of accretion flows onto dense filaments in NGC 1333. According to models where a post-shock layer of a converging flow produces filaments (e.g., Chen & Ostriker 2014a; 2015a), a sub-filamentary network only arises in a strong magnetic field. In these models, gravity drives the accretion flows in a post-shock layer. The resulting flows move predominately along the field lines and may not necessarily contain sub-structures with densities high enough to be distinguished from the rest of the planar, accretion flow. Without visible substructures, these flows may appear as a large-scale background to *Herschel* due to their planar geometry, making them difficult to discern.

Post-shock accretion models, such as those developed by Chen & Ostriker (2014a), have been proposed by Dhabal et al. (2019) as an explanation for the observed large $\nabla v_{\rm LSR,\perp}$ along the south-western edge of filament *c*. This particular $\nabla v_{\rm LSR,\perp}$ structure has been found in both the high resolution NH_3 and N_2H^+ observations by Dhabal et al. (2019) as well as our NH_3 observations. The filament *h* we identify with two-slab fits, which runs parallel to filament *c*, also displays similar $\nabla v_{\rm LSR,\perp}$ over the same region. In a post-shock accretion interpretation, such a similarity suggests that filament *h* belongs to the same planar flow as filament *c*. Interestingly, filament *h* is spatially well resolved in the high-resolution observation by Dhabal et al. (2019) as a filament distinct from *c*.

It is worth noting that Walsh et al. (2006) measured infall velocities of ~ 1 km s^{-1}

towards the south-western edge of filament h with HCO^+ (1-0) observations, modelled as self-absorbed lines. The infall velocities measured with HCO^+ (1-0), which were interpreted as a sign of large-scale ($\sim$ 0.2 pc) infall, are similar to the observed $v_{\rm LSR}$ separation ($\sim$ 0.8 km s^{-1}) between filaments c and h in NH_3 along lines of sight. Given that this infall region spatially correlates with filaments c and h, the HCO^+ (1-0) observed there may indeed trace the same planar accretion flow as that suggested by the large NH_3 $\nabla v_{\rm LSR,\perp}$ we see towards filaments c and h.

Not all the observed $\nabla v_{\rm LSR,\perp}$ structures in our filaments can be well explained by models of accretion flow along a post-shock layer. While the compact nature of $\nabla v_{\rm LSR,\perp}$ may be explained by clumpy, inhomogeneous accretion, the sign (i.e., direction) alternation of $\nabla v_{\rm LSR,\perp}$ along filament edges, however, does not conform well to the planar geometry naively expected from a post-shock layer. Some, if not all, of these observed $\nabla v_{\rm LSR,\perp}$ features, may thus be driven by a different physical process.

While rotation of small bodies, such as dense cores, may produce compact $\nabla v_{\rm LSR,\perp}$ signatures, no clear correlation exists between cores and many of these compact $\nabla v_{\rm LSR,\perp}$ regions in the majority of the cases. Inhomogeneous accretion flows, on the other hand, similar to those seen in the non-magnetized simulation by Clarke et al. (2017) may explain the sign-changing behavior of these $\nabla v_{\rm LSR,\perp}$ along filament edges. Indeed, the shocked regions bordering dense structures in their simulation, as traced by local velocity divergence, morphologically resemble the $\nabla v_{\rm LSR,\perp}$ structures seen in NGC 1333. Further investigation with synthetic observations of simulations is needed to see if such a resemblance holds and whether or not magnetic fields play an important role in such an accretion.

Radial Dependencies

Figure 2.14 shows the magnitudes of the perpendicular and parallel velocity gradients plotted as functions of their respective distances from the filament spines. Their median, 15$^{\rm th}$, and 85$^{\rm th}$ percentile values are marked. While the parallel velocity gradients show little correlation with their distances from filament spines, the perpendicular velocity gradients tend to decrease as one moves towards the spine in many filaments.

Specifically, filaments b, e, f, g, and j clearly show such a trend. Indeed, the Wald Test (see Fahrmeir et al. 2013) revealed that these filaments all have p-values < 0.01 for a null hypothesis where the data are consistent with a zero-slope linear trend.

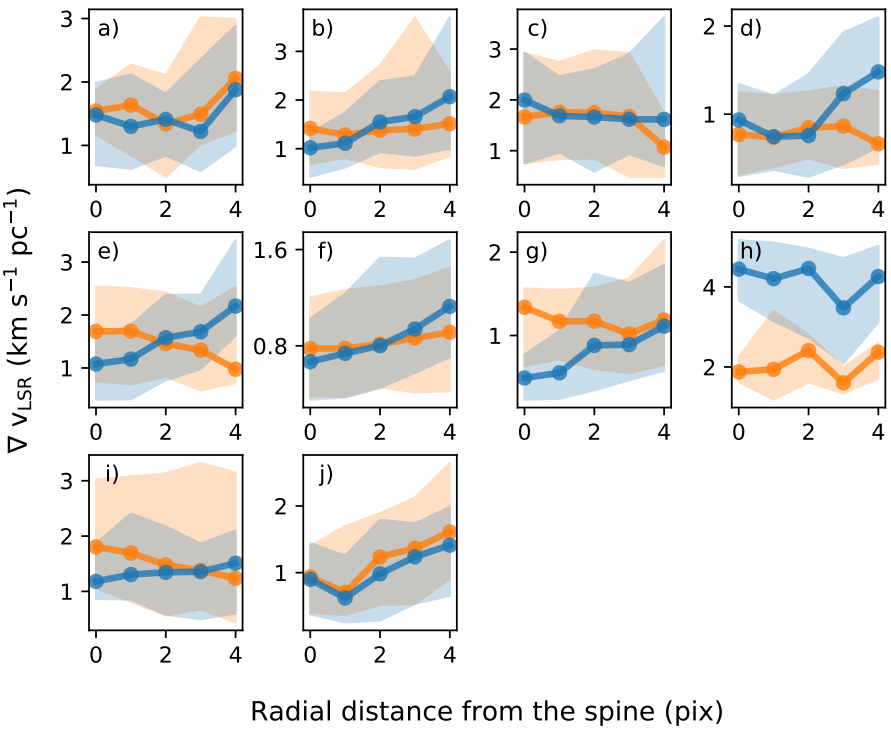

Figure 2.14: Median magnitudes of the perpendicular (blue) and parallel (orange) velocity gradients plotted as a function of their distance to the filament spines. The median values are marked by the connected dots while the 15$^{\text{th}}$ and 85$^{\text{th}}$ percentile values mark the lower and upper bound of the shaded regions, respectively.

The linear least-squares regression slopes of these trends are 0.40, 0.41, 0.17, 0.21, and 0.16, respectively, in units of km s^{-1} pc $^{-2}$. Moreover, the Pearson correlation coefficients, i.e. r-values (see Cohen 1988), of these regressions all fall in the range of 0.2 - 0.4, suggesting that these positive correlations are indeed significant but relatively scattered.

The decreasing trends in these filaments persist when gradients are calculated with smaller sampling distances ($r < 3$ pixels). Indeed, the regression slopes for these filaments actually increases with smaller sampling distances.

A decrease in $|\nabla v_{\mathrm{LSR},\perp}|$ towards a filament spine contradicts the behaviour of free-falling gas. Such a free-fall behavior is often assumed for gas accretion onto a filament in simple analytical models (e.g., Heitsch et al. 2009; Palmeirim et al. 2013). While filaments themselves are not typically expected to behave like pressureless systems, except for maybe the very massive ones (e.g., M $\sim$ 600 M$_\odot$; Gómez & Vázquez-

Semadeni 2014), a simple analytical examination of such an assumption can still provide vaulable perspectives in light of our results.

Consider a parcel of gas falling onto an infinitely long cylinder axially centered at $r = 0$. Such a parcel would have a velocity profile of $v_{\rm ff} \propto [\ln(r_0/r)]^{1/2}$ if the parcel was initially at rest at r_0 (see Heitsch et al. 2009). The radial derivative of this profile, i.e., $\nabla v_{\rm LSR,\perp}$, thus would be $dv_{\rm ff}/dr \propto [r^2 \ln(r_0/r)]^{-1/2}$ and would increase monotonically in magnitude towards the filament spine for r values less than $\sim r_0/2$. The observed $\nabla v_{\rm LSR,\perp}$ for that parcel of gas should thus increase towards a filament spine if the parcel's emission dominates over others along the line of sight, and its trajectory is not parallel to the plane of the sky.

While such a geometric assumption does not describe a simple, axially-symmetric accretion of a filament, it reasonably approximates inhomogeneous (e.g., Clarke et al. 2017) or anisotropic (e.g., Chen & Ostriker 2014a) accretion flows found in realistic simulations. In fact, the former model is unlikely to produce observable $\nabla v_{\rm LSR,\perp}$ in the first place, contrary to what we have observed. Thus, if these non-symmetric assumptions hold true for our observations, then the observed decrease in $|\nabla v_{\rm LSR,\perp}|$ towards the filament spine indeed suggests these filaments do not behave like a pressureless system under the accretion flow interpretation. The $\nabla v_{\rm LSR,\perp}$ we observed may thus suggest ongoing accretion that is being damped by the higher density material as the accreting gas moves closer to the filament spine.

Orientations

Figure 2.15 shows the orientation angles of the measured velocity gradients, θ, binned into polar histograms. The direction along a filament spine away from the end closest to the image origin, i.e., the bottom left corner, defines the zero-point reference of our angle θ. The convention is set such that vectors with $-180° < \theta < 0°$ point away from the spine and vectors with $0° < \theta < 180°$ point towards the spine.

Most of the $\nabla v_{\rm LSR}$ vectors within an NGC 1333 filament are not randomly oriented and often display unimodal or bimodal behaviours. A circular statistics analysis conducted with a Rayleigh test (Wilkie 1983a) shows that the θ values found in 9 out of the 10 of filaments are very unlikely to have been drawn from a random distribution ($p < 0.01$).

Coherent $\nabla v_{\rm LSR}$ orientations may seem perplexing at first considering how complex the $\nabla v_{\rm LSR}$ structures appear on small scales. A clearer picture emerges, how-

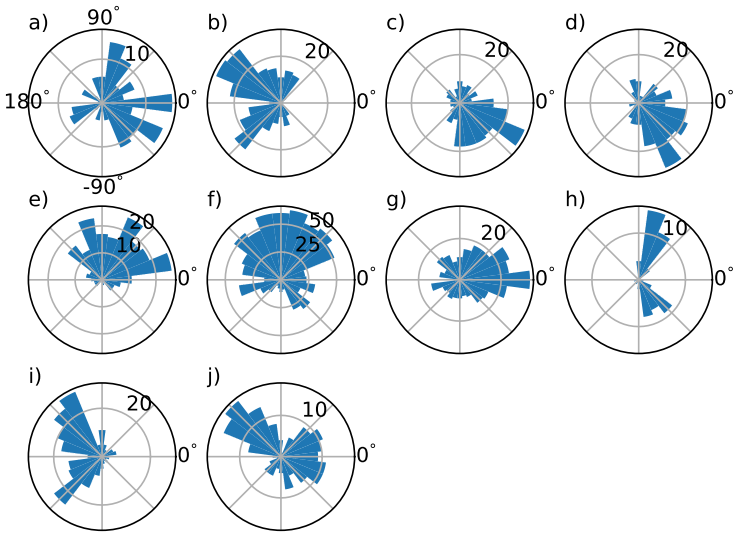

Figure 2.15: Polar histograms of the $\nabla v_{\rm LSR}$ orientations shown for each filament.

ever, when the $\nabla v_{\rm LSR,\parallel}$ on large scales and the radial dependency of $|\nabla v_{\rm LSR,\perp}|$ on small scales are considered together. For example, mass flows along filaments combined with perpendicular (i.e., radial) accretion onto filament edges may have caused the preferential $\nabla v_{\rm LSR}$ orientations observed here. After all, physics that are likely important in forming filaments, e.g., gravity and magnetic fields, do tend to impose order. If the observed $\nabla v_{\rm LSR}$ values are indeed indicative of mass flows, then filaments in NGC 1333 may be viewed as loci of collapsing flows where radially accreted gas changes direction to flow along filaments and into cores.

2.6 Summary

In this paper, we devised an efficient and robust method (i.e., MUFASA) to fit two-slab NH_3 (1,1) spectra automatically, one that is generalizable for other molecular species. We tested the performance of MUFASA on synthetic spectra and found it to be particularly robust at identifying two-component spectra with dissimilar σ_v between their components. This behavior makes MUFASA effective at disentangling subsonic gas from supersonic gas along lines of sight. By selecting our best fit model via a statistical approach, we recovered $\sim 40\%$ of the two-component NH_3 spectra from our synthetic data that would otherwise be culled by the $\Delta v_{\rm LSR} = 0.25$ km s^{-1} threshold used by Hacar et al. (2017) for their study of NGC 1333 with N_2H^+.

Based on our fit residuals, we find no strong evidence that three-component fits are warranted in NGC 1333.

We identified 3D filament spines in ppv space from MUFASA line-fitted models using our implementation of the generalized (i.e., weighted) SCMS algorithm (see Chen et al. 2014), CRISPy. The generalized SCMS operates on a well-established statistical framework where the orientations of the density ridges (e.g., spines) are well defined locally. We sorted the fitted models into velocity-coherent filaments with these spines and measured the velocity gradients of their filaments on a beam-resolved scale ($\sim$ 0.05 pc). We further decomposed these velocity gradients into parallel and perpendicular components with respect to the local spine.

By applying our analysis techniques to the observation of NGC 1333, we find the following:

1. Many filaments have remarkably linear changes in $v_{\rm LSR}$ along their spines on larger scales ($>$ 0.2 pc). The $\nabla v_{\rm LSR}$ corresponding to these changes are in the range of 0.8 - 2.5 km s^{-1} pc $^{-1}$, similar to those found in previous works (e.g., Kirk et al. 2013a). Several of these filaments have ends or sharp bends that spatially correlate with the kernel estimated over-densities of dense cores and embedded YSOs derived by Hacar et al. (2017). This result suggests the observed $\nabla v_{\rm LSR}$ may indeed be tracing mass flow along filaments towards star-forming cores.

2. Most filaments with a linear $v_{\rm LSR}$ profile along their spines have values that increase northwards. Considering that the median $v_{\rm LSR}$ of these filaments tends to increase northwards as well, these filaments may trace a larger-scale ($>$ 4 pc) filamentary accretion flow, similar to that assumed by Matzner & Jumper (2015) in their model, from which the NGC 1333 clump may be fed.

3. The $\nabla v_{\rm LSR,\parallel}$ measured on small scales show quasi-oscillatory $v_{\rm LSR}$ along filaments. These quasi-oscillations, however, do not correlate well with dense structures, a result similar to those found by Tafalla & Hacar (2015) in real N_2H^+ observation and by Smith et al. (2016) in synthetic $C^{18}O$ observations of a simulation. This lack of correlation suggests periodic gravitational instabilities are not responsible for such an observed behaviour. Alternative mechanisms, such as magnetic waves (e.g., Tritsis & Tassis 2016) may be responsible instead.

4. The $\nabla v_{\rm LSR,\perp}$ found on small scales tend to form compact structures near the fil-

ament edges, potentially indicating perpendicular accretion flows. The compact nature of these $\nabla v_{\rm LSR,\perp}$ structures combined with an apparent lack of ambient sub-filaments suggest these accretion flows are likely clumpy, i.e., inhomogeneous. Alternations in the direction of these $\nabla v_{\rm LSR,\perp}$ structures along filament edges also suggest these accretion flows may not be purely planar like those found in simulated magnetized post-shock layers (e.g., Chen & Ostriker 2014a), except possibly those first reported by Dhabal et al. (2019) for filaments *c* and *h*.

5. The magnitudes of the measured $\nabla v_{\rm LSR,\perp}$ decrease prominently toward filament spines in half (i.e., 5) of our filaments. Assuming our observations trace gas flows that are inhomogeneous or anisotropic with respect to the filament spines, such a trend is inconsistent with free-fall accretion models and suggest that these filaments do not behave like pressureless structures. Such an observed behaviour may thus indicate the infall of accretion flows being damped by the denser, pressure-supported gas within filaments.

6. The $\nabla v_{\rm LSR}$ vectors measured on small scales are not randomly oriented within a filament. Their orientations tend to be unimodally or bimodally distributed. This global trend within filaments conforms to a scenario by which the gas falling onto a filament is redirected to flow along the filament as it approaches the spine.

For our interpretations, we assumed the observed velocity gradients are indeed signs of accelerating gas seen along lines of sight. We plan to apply our analysis to synthetic NH_3 observations in future work to understand better the nature of these velocity gradients.

Chapter 3

Turbulence, Accretion, and Infall: a High-resolution Study of the B5 Filaments

The material in this chapter is submitted for publication in the Astrophysical Journal under the same title by Michael Chun-Yuan Chen, James Di Francesco, Jaime E. Pineda, Stella S. Offner, and Rachel K. Friesen. The analysis was led by me, with data acquisition led by Jaime Pineda (Pineda et al. 2010a; Pineda et al. 2015).

3.1 Introduction

Interstellar filaments appear to be intricately connected to star formation (Schneider & Elmegreen 1979; Balsara et al. 2001; André et al. 2014). Not only are they ubiquitous in molecular clouds (e.g., André et al. 2010; Men'shchikov et al. 2010; Miville-Deschênes et al. 2010; Hill et al. 2011; Roy et al. 2015), they also seem to host the majority of the star-forming cores (Könyves et al., 2015). Indeed, numerical simulations show that filaments are not only naturally produced by supersonic turbulent clouds (e.g., Porter et al. 1994; Vazquez-Semadeni 1994; Padoan et al. 2001), but the densest gas within these model filaments can also collapse to form stars under self-gravity, (e.g., Ostriker et al. 1999; Ballesteros-Paredes et al. 1999; Klessen & Burkert 2000; Bonnell et al. 2003; Mac Low & Klessen 2004; Tilley & Pudritz 2004; Krumholz et al. 2007). How filaments form and evolve in actual molecular clouds, however, remains to be characterized in detail, particularly in relation to star-forming

cores.

Observationally, filaments seem to possess a characteristic width of ~ 0.1 pc (e.g., Arzoumanian et al. 2011; Palmeirim et al. 2013; Arzoumanian et al. 2019). The origin of such a width has been attributed to the sonic scale, at which supersonic turbulent gas becomes subsonic, set by the typical cloud conditions found in the Milky Way spiral arms (Federrath, 2016). Interestingly, this ~ 0.1 pc sonic scale closely resembles that found empirically for dense cores (Goodman et al., 1998). Furthermore, subsonic levels of non-thermal motion have been observed in both dense cores (e.g., Barranco & Goodman 1998; Kirk et al. 2007; Rosolowsky et al. 2008) and filaments (e.g., Pineda et al. 2011; Hacar & Tafalla 2011; Hacar et al. 2016), suggesting that cores and filaments likely share a common origin.

While the non-thermal motions exhibited by subsonic cores have often been attributed to turbulence (e.g., Goodman et al. 1998; Pineda et al. 2010a; Chen et al. 2019a), infall motions have been proposed lately as an alternative under the global hierarchical collapse scenario (Vázquez-Semadeni et al., 2019). The turbulence interpretation, which often fits under the "gravoturbulent" scenario (e.g., Mac Low & Klessen 2004), implies that subsonic cores are formed under shock compression followed by turbulence dissipation (e.g., Chen et al. 2020b). The infall interpretation, on the other hand, suggests cores originate as density enhancements in mildly supersonic clouds and only start to contract as prestellar objects when the average Jeans mass in the cloud is reduced to that comparable to the cores, as the result of ongoing cloud contraction (Vázquez-Semadeni et al., 2019). These interpretations likely hold as well for subsonic filaments, which appear to be intimately linked to dense cores.

The key to constraining core formation models, therefore, requires not only a detailed understanding of the non-thermal motions within cores but also the relationship between cores, their host filaments, and their ambient environment. For example, filaments formed out of magnetized shock-compressed layers are expected to accrete preferentially along magnetic field lines, which are not necessarily perpendicular to filaments and can be bent and distorted by gas self-gravity as filaments evolve (e.g., Chen & Ostriker 2014b). Filaments formed in the global hierarchical collapse scenario in the absence of a magnetic field, on the other hand, are expected to accrete material from their surroundings in a perpendicular direction while they feed cores and clumps along their lengths (e.g., Gómez & Vázquez-Semadeni 2014). Gas flow analysis of observed filaments, therefore, is invaluable to understanding the formation and evolution of cores and filaments.

Observational studies have measured velocity gradients in filaments over directions that are either perpendicular (e.g., Palmeirim et al. 2013; Fernández-López et al. 2014; Dhabal et al. 2018) or parallel (e.g., Kirk et al. 2013b; Friesen et al. 2013) to a filament. The former and the latter measurements have often been interpreted as acceleration/deceleration of accretion flows onto and along filaments, respectively. By identifying filament spines and using them as precise local references for orientations, Chen et al. (2020c) measured velocity gradients simultaneously in both the parallel and the perpendicular directions on the ~ 0.05 pc scale and further revealed a wealth of kinematic structure that is not necessarily expected from simple accretion scenarios.

In this paper, we expand on the methods developed by Chen et al. (2020c) to explore the gas kinematics of the Perseus B5 region at a ~ 0.009 pc resolution with the NH_3 (1,1) observations first obtained by Pineda et al. (2015). We further model the NH_3 (1,1) emission with two spectral components to uncover a second NH_3 component along some lines of sight that was previously unseen in the B5 region (Pineda et al. 2010a; Pineda et al. 2011; Pineda et al. 2015; Schmiedeke et al. submitted; hereafter P10, P11, P15, and S20). At a distance of 302 pc (Zucker et al., 2018), Perseus B5 is a well-studied star-forming clump with the first known observation of a sharp spatial transition between a subsonic core and its supersonic surroundings (P10). The clump is also known to host at least a single protostar (B5-IRS1; Fuller et al. 1991). A subsequent high-resolution (~ 0.009 pc) study of B5 revealed that the "core" actually consists of several filaments that are well embedded within the sonic region (P11). A more sensitive followup of the P11 study at the same resolution further showed the highest column density regions of these B5 filaments seem to be gravitationally bound to each other and the B5-IRS1 protostar, likely in the process of forming a quadruple star system (P15). These properties combined make B5 a highly attractive region to explore further the origin and evolution of cores and filaments on the verge of forming stars.

Our paper is laid out as follows. In Section 4.2 and 4.3, we briefly describe the B5 data and our analysis methods, respectively. We present our results in Section 3.4, followed by a discussion of these results in Section 3.5. We end our paper with a concluding summary in Section 3.6.

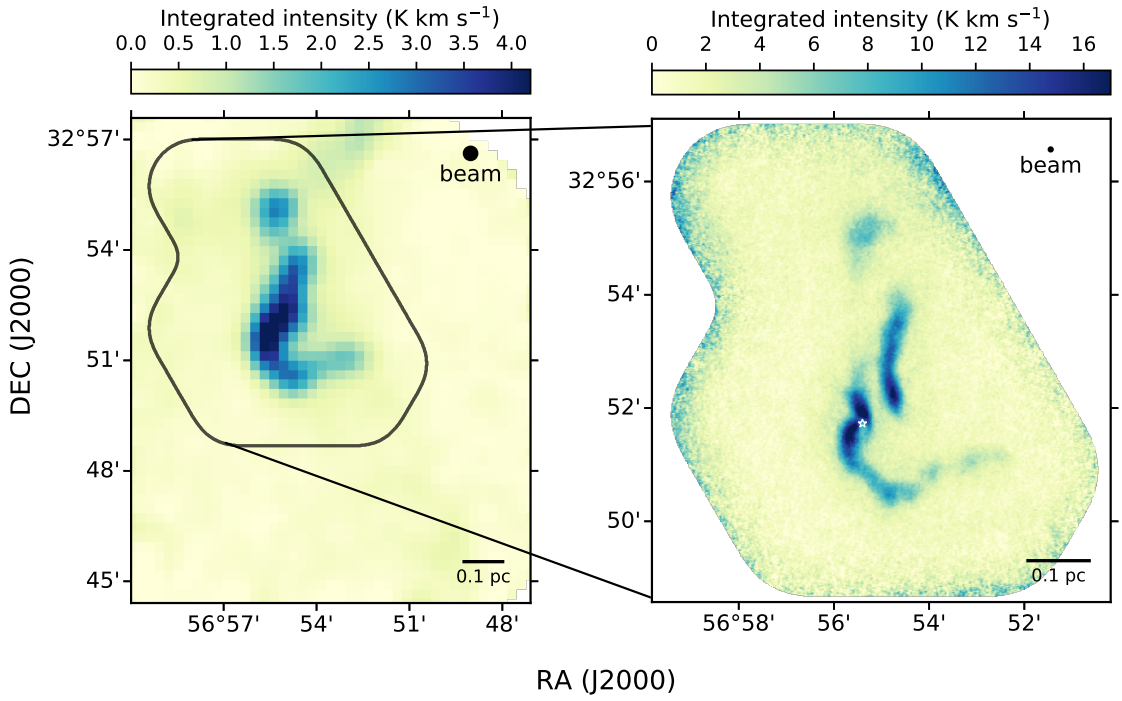

Figure 3.1: Integrated intensity maps of the NH_3 (1,1) emission seen towards the Perseus B5 region made with the GBT-only (left) and the GBT+VLA (right) observations. The on-sky footprint of the VLA observation is shown in white on the left panel and the position of B5-IRS1 protostar is marked by the star symbol in the right panel. The beam corresponding to each data set is shown in their respective panels, along with a physical scale bar.

3.2 Data

Our B5 data consist of single-dish observations made by Pineda et al. (2010a; hereafter P10) with the Robert F. Byrd Green Bank Telescope (GBT) and interferometric observations made by Pineda et al. (2015; hereafter P15) with the Jansky Very Large Array (VLA).

The P10 GBT observations were made with the On-The-Fly (Mangum et al., 2007) technique using K-band receivers and a 3.050 kHz channel width. These observations were reduced with `GBTIDL` (Marganian et al., 2013) and have angular and spectral resolutions of 31″ and 0.04 km s^{-1}, respectively. The final data product was imaged on a 15″.5 pixel grid and has a median rms noise of 0.046 K.

The P15 VLA observations were made with the K-band receivers and the WIDAR correlator at a 3.90625 kHz channel width (i.e., 0.049 km s^{-1} equivalent for the NH_3

spectra). The data were observed in the D-array and the CnD-array (project 11B-101) configurations, consisting of 27 mosaic pointings. P15 reduced the VLA data with the `CASA` (McMullin et al., 2007) software and combined the VLA data with the P10 GBT data to recover the large-scale structures of which the VLA is insensitive. The data were imaged using a 6″ circular beam with the multi-scale clean method and a robust parameter of 0.5, corrected by the primary beam, over the same 3.90625 kHz channel width. The final root mean square (rms) noise level of the reduced data is 0.24 K per channel, about 3.5 times lower than that of the P11 data, which is not a part of P15's reduced data product. For our study, we grid the final image over 1″ size pixels.

Figure 3.1 shows the integrated intensity maps of the NH_3 (1,1) emission of B5 imaged with the GBT-only (left) and the GBT+VLA combined (right) observations. The 31″ and 6″ beams of the GBT-only and the GBT+VLA data, respectively, are shown in their respective panels. At a distance of 302 pc, the physical sizes of the former and latter beams are 0.045 pc and 0.009 pc, respectively.

3.3 Method

3.3.1 Spectral-fitting

We fit multi-component spectra to the NH_3 (1,1) data using the `MUFASA` software (Chen et al. 2020c; hearafter, C20), which wraps around the `PySpecKit` package (Ginsburg & Mirocha, 2011) to perform least-squares fitting via the Levenberg–Marquardt (LM; Levenberg 1944; Marquardt 1963; Moré 1978) method automatically. For each NH_3 (1,1) spectrum, we fit up to two velocity components per model, with each of these velocity components consisting of 18 hyperfine lines. We model each of our velocity components as a homogeneous gas slab parameterized by its velocity centroid ($v_{\rm LSR}$), velocity dispersion (σ_v), excitation temperature (T_{ex}), and optical depth (τ_0). The final spectral model is generated via radiative transfer by including the cosmic microwave background (CMB) through each individual slab along the line of sight towards the observer. The spectral response of the frequency channels is not included in our model.

To ensure the robustness of our fits, we adopt `MUFASA`'s default (C20) recipe to fit our spectrum automatically over two iterations. Under this recipe, `MUFASA` first spatially convolves the cube to twice its beamsize and then fits the convolved cube

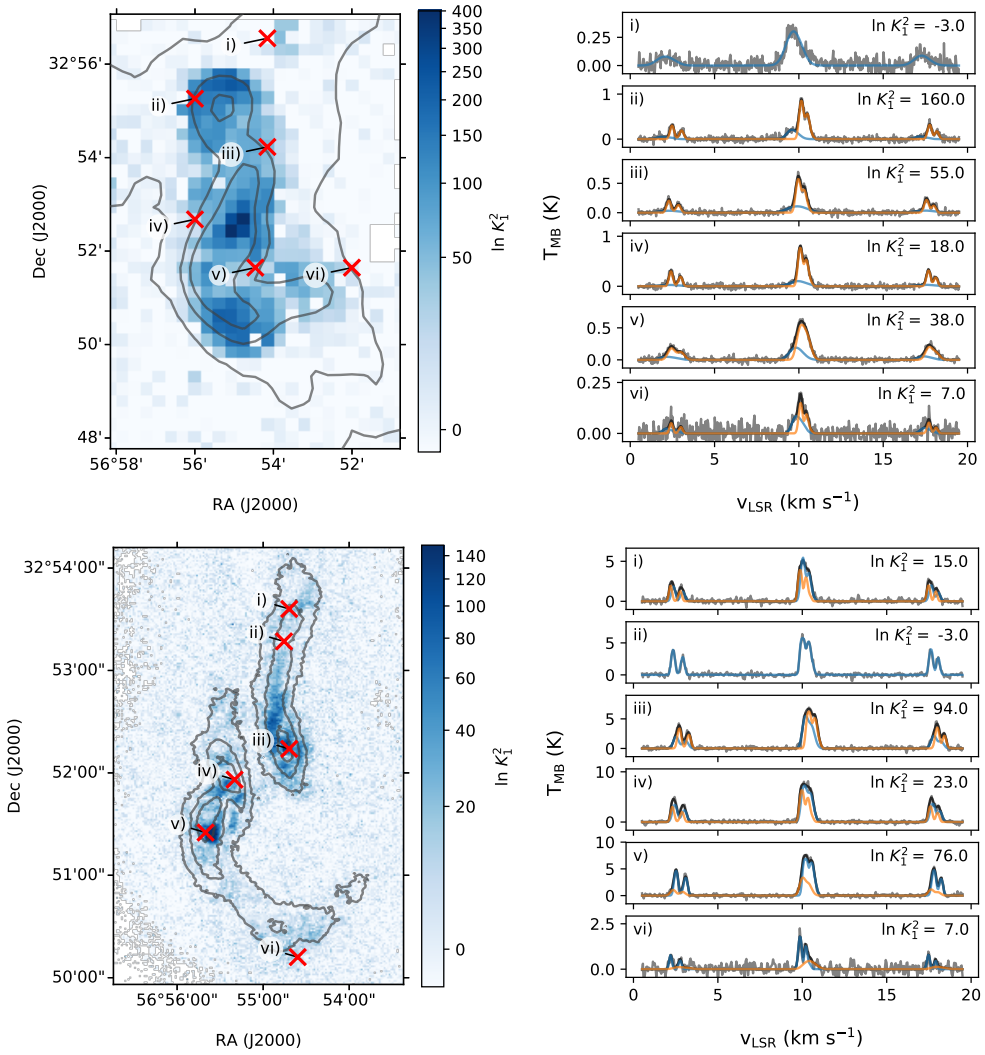

Figure 3.2: The left panels show the relative likelihood maps of our two-component fits over the one-component fits (i.e., ln K_1^2) to the GBT-only (top) and the VLA+GBT (bottom) data, as determined from the AICc. Grey contours correspond to where the NH_3 (1,1) integrated intensities are 0.3 K km s^{-1}, 1.2 K km s^{-1}, and 2.4 K km s^{-1} in the GBT-only data and 5 K km s^{-1}, 10 K km s^{-1} and 15 K km s^{-1} in the VLA+GBT data. Red 'x' symbols mark from where the example fits (black), their individual components (blue and orange), and their corresponding spectra (grey) shown in the right panels are taken.

using initial parameter guesses derived from its zeroth, first, and second moments. Following this initial fit, `MUFASA` then passes the fit results as initial guesses to a subsequent, full-resolution fit. This approach allows `MUFASA` to take advantage of the higher signal-to-noise ratio (SNR) and the increased spatial awareness of the convolved cube at each pixel to assist with fits to the full-resolution cube.

Once the full-resolution fits are obtained, `MUFASA` selects the best-fit model between the two-, one-, and zero-component (i.e., noise) fits on a pixel-by-pixel basis using the corrected Akaike Information Criterion (AICc; Akaike 1974; Sugiura 1978), where the small letter c denotes the second-order correction made to account for finite sample sizes. `MUFASA` selects one model over another when their relative log-likelihood determined by the AICc, i.e.,

$$\ln K_a^b = -\left(\mathrm{AICc}_b - \mathrm{AICc}_a\right)/2 \tag{3.1}$$

is above the statistically robust threshold of 5 (Burnham & Anderson, 2004), where the subscripts a and b represents arbitrary models a and b, respectively, and K_a^b is the relative likelihood of model b over model a. This approach allows `MUFASA` to detect signals more robustly than adopting a simple SNR threshold, obtaining results similar to the Bayesian method by Sokolov et al. (2020) without needing to sample likelihood spaces exhaustively for each fit.

`MUFASA`'s ability to fit spectra and select models correctly using the standard recipe described above is presented by C20 in their paper, based on test fits to 30,000 randomly generated synthetic spectra. To improve our fits further beyond those provided by the standard recipe, we perform yet another fit with new initial guesses derived from the Gaussian-smoothed results obtained from the standard fits. Pixels with Jacobian-estimated v_{LSR} and σ_v errors larger than 0.2 km s^{-1} are removed from the initial guesses before they are interpolated and smoothed with a Gaussian kernel with a width of $\sigma_{\mathrm{ker}} = 1$ pixel. For pixels with $\ln K_1^0 < 50$, where the SNRs of spectra are expected to be lower, a kernel with $\sigma_{\mathrm{ker}} = 3$ pixels is used instead. This additional iteration of fits successfully improves situation for the initially poorly-fitted pixels that are sporadically and sparsely scattered in regions that appear by eye to be well-fitted otherwise.

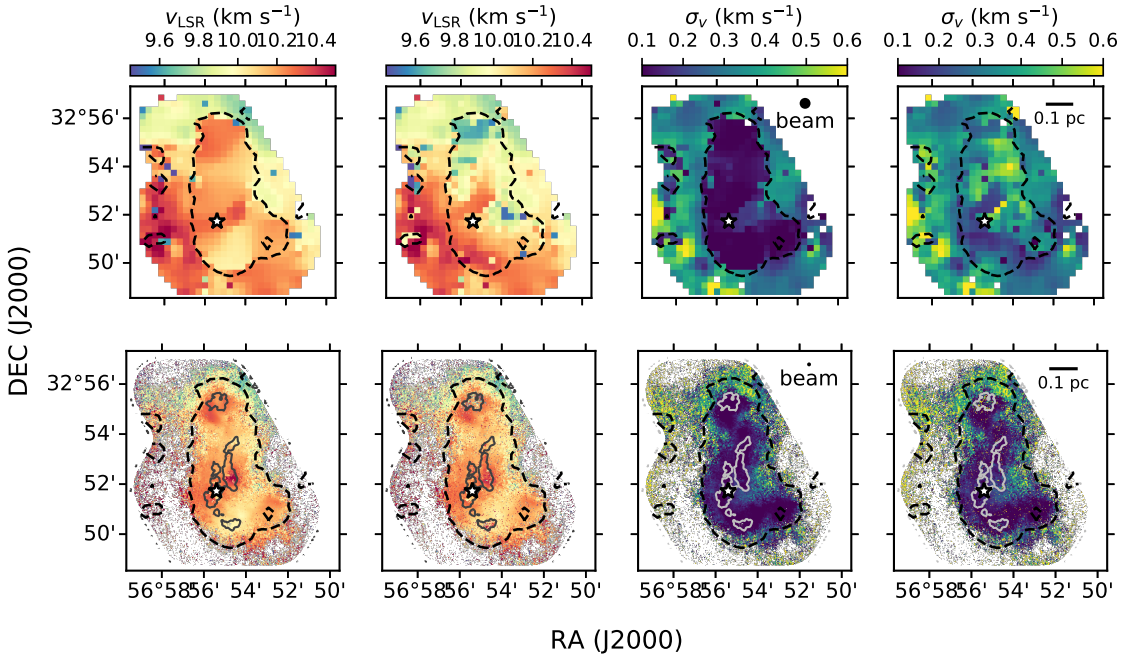

Figure 3.3: The $v_{\rm LSR}$ (left two columns) and σ_v maps (right two columns) derived from fits to the GBT-only data (top row) and the VLA+GBT data (bottom row). The star shows where the protostar IRS1 is located. The dashed black contour demarcates where two-component models fit the GBT-only data better (i.e., $\ln K_1^2 > 5$) while the solid grey contour in the bottom row demarcates where two-component models fit the VLA+GBT data better. The spectral components with the narrower σ_v are shown in the odd-numbered columns while their wide σ_v counterparts are shown in the even-numbered columns, inside the $\ln K_1^2 > 5$ contours of their respective data. Pixels outside the $\ln K_1^2 > 5$ contours show the same one-component fit results for all panels. The beams of the data and physical scale bars are shown in the third and fourth columns, respectively.

3.3.2 Filament Identification

Following C20, we identify filament spines in position-position-velocity (ppv) space using the emission cube we reconstructed from our spectral fits to the VLA+GBT data. To reveal the underlying kinematic structures and minimize spectral confusion, we remove the hyperfine structures in our reconstruction by modeling the optical depth (i.e., τ) profile of each velocity component as a single Gaussian. The peak τ value of each velocity component is set to one-tenth the peak τ value of all the hyperfine lines combined, as derived from the fits, to mimic the optical depths of the satellite hyperfine lines that are typically thin. To ensure the structures are well sep-

arated spectrally, we further constrained the velocity dispersions of the reconstructed emission to a constant, minimally Nyquist-sampled value of $\sigma_v = 0.043$ km s^{-1}. We call such a reconstructed emission cube a deblended cube.

We identified filament skeletons from the deblended cube using the `CRISPy` software developed by C20, which finds filament skeletons as one-dimensional density ridges in multi-dimensional images with the generalized Subspace Constrained Mean Shift (SCMS) method (Chen et al. 2014). The `Python`-based `CRISPy` software is derived and generalized from the `R` code written earlier by Chen et al. (2015). Filament skeletons identified through the SCMS framework have mathematically well-defined orientations set by the local density field. We further prune skeletons into branchless spines using the infrastructure developed by C20 based on its two-dimensional predecessor by Koch & Rosolowsky (2015). The filament spines are defined by the longest path within a skeleton.

3.4 Results

3.4.1 Derived $v_{\rm LSR}$ and σ_v maps

The left panels of Figure 3.2 show the relative log-likelihood maps of our two-component fits over the one-component fits as determined by the AICc. The right panels show example spectra and their best-fit models taken from positions shown in the left panels. For the GBT-only data, we detected NH_3 (1,1) spectra in all 741 pixels that lie within the footprint of the VLA observation. Out of these 741 pixels, 280 (i.e., 38%) of them are better fitted with two-component models. For the VLA+GBT data, we detected 119,398 spectra over the entire 166,920 pixel footprint, where 19,800 pixels of the detected spectra (i.e., 17.0%) are better fitted with two component models. The reduced fraction of two-component-detected spectra in the VLA+GBT data is likely caused by a reduction in the data's sensitivity to the larger-scale emissions associated with a smaller beam.

Figure 3.3 shows the $v_{\rm LSR}$ and σ_v maps derived from our best model fits to the GBT-only data and the VLA+GBT data, for both components. Interestingly, the GBT-only $v_{\rm LSR}$ and the σ_v maps of the wide-component appear more similar by eye to their single-component-only surroundings than their narrow-component counterparts do. Such a trend, however, is not seen in the VLA+GBT data.

Figures 3.4 and 3.5 show the kernel-estimated probability density distribution of

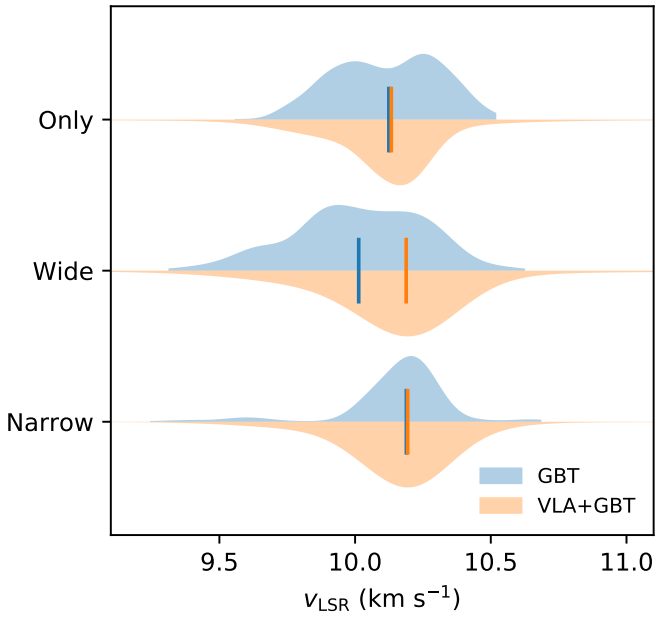

Figure 3.4: The kernel-estimated probability density distribution of the $v_{\rm LSR}$ derived from the fits to the GBT (blue) and the VLA+GBT (orange) data for the narrow, wide, and only component fits. The y-scaling is normalized to the peak value while the horizontal bars shows the median values of the distributions.

the $v_{\rm LSR}$ and σ_v, respectively, derived from fits to the GBT-only and the VLA+GBT data for the narrow, wide, and only component fits. Only pixels within the on-sky footprints of the VLA observations for both data sets are used for these comparisons. For reference, when the non-thermal component of σ_v, i.e.,

$$\sigma_{v,\rm NT} = \sqrt{\sigma_v^2 - k_b T_{\rm kin}/\mu_{\rm NH_3} m_{\rm H}} \tag{3.2}$$

is less than the isothermal sound speed of a gas,

$$c_s = \sqrt{k_b T_{\rm kin}/\mu_{\rm ISM} m_{\rm H}}, \tag{3.3}$$

the total σ_v would have values of

$$\sigma_v < \left[\frac{k_b T_{\rm kin}}{m_{\rm H}}\left(\frac{1}{\mu_{\rm ISM}} + \frac{1}{\mu_{\rm NH_3}}\right)\right]^{1/2}, \tag{3.4}$$

with k_b and m_H being the Boltzmann constant and atomic hydrogen mass, respectively. If we assume a kinematic gas temperature ($T_{\rm kin}$), an NH_3 molecular weight

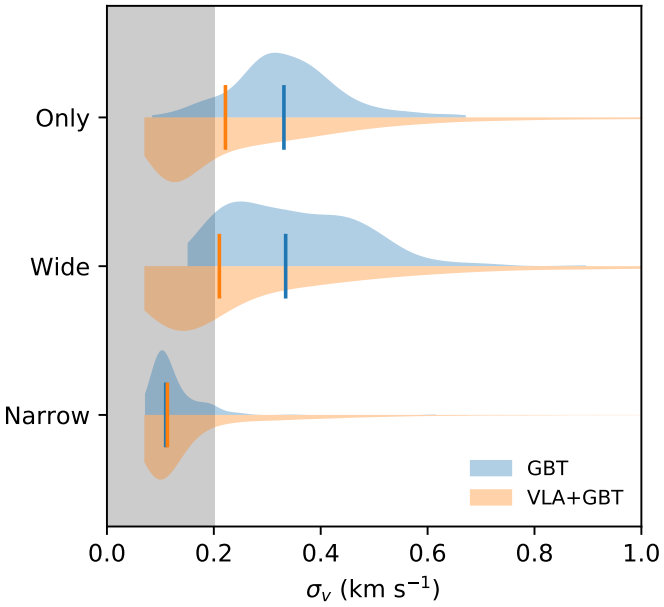

Figure 3.5: Same as Figure 3.4, but for derived σ_v. The shaded region indicates where the non-thermal component of σ_v is subsonic for a body of gas with kinematic temperature, T_k, of 10 K.

(μ_{NH_3}), and a mean interstellar molecular gas weight (μ_{ISM}) of 10 K, 17.031, and 2.33, respectively, then the total σ_v of a gas with a subsonic level of non-thermal motion should have values of $\lesssim 0.2$ km s^{-1}. We note the purely thermal motion of a gas under such assumptions has a speed of 0.19 km s^{-1}, a value that is marginally smaller than the total σ_v due to $\mu_{NH_3} \gg \mu_{ISM}$.

Figures 3.4 and 3.5 show that the narrow components detected in both the GBT-only and the VLA+GBT data appear to have similar distributions of v_{LSR} and σ_v, suggesting that these components likely trace the same gas population. The wide and single-only components detected in the GBT-only data, however, appear dissimilar to their VLA+GBT counterparts. In particular, the σ_v values derived from the VLA+GBT data are substantially lower than their GBT-only counterparts. The wide and only components detected by the VLA+GBT observations thus likely trace distinctly different gas than those detected by the GBT alone. Such a difference in detection is likely due to the VLA+GBT data's higher angular resolution, which makes them more sensitive than the GBT-only data to the compact, previously unresolved structures but less sensitive to the already well-resolved, diffuse gas.

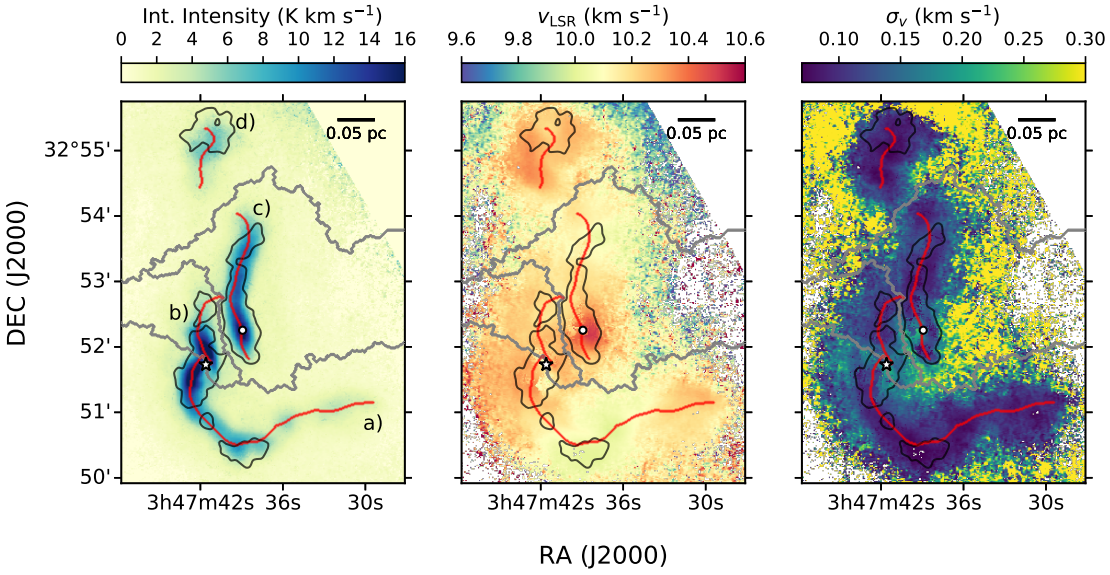

Figure 3.6: Filament spines (red) identified by `CRISPy` overlaid on the total modelled integrated intensity, (left), the sorted $v_{\rm LSR}$ (center), and the sorted σ_v (right) maps of our best fit model to the NH_3 VLA data. The position of the IRS1 protostar and *B5-Cond1* condensation (P15) are marked by the star and circle symbols, respectively. The borders of the watershed regions, identified from the integrated intensity map, are shown in light grey. Smoothed contours of where the data are better fitted by two components, i.e., where $\ln K_1^2 > 5$, are shown in black. Physical scale bars are shown in all panels.

3.4.2 Identified Filaments

The left panel of Figure 3.6 shows the `CRISPy` identified filament spines overlaid on top of the integrated intensity map of our modelled fits to the VLA+GBT data. The branches initially identified by `CRISPy` as a part of filament skeletons have been removed, leaving the longest paths through these skeletons as our final, branchless spines. In B5, we identify four filament spines in total. They are named alphabetically from *a* to *d*, ordered from the filament furthest from the origin of the image, i.e., the southeastern corner, to the one that is the nearest. While filament *d* appears by eye to have a relatively low aspect ratio, it does contain a well-defined density ridge traced by `CRISPy`. To ensure we have a complete, relatively unbiased sample, we include filament *d* in our analyses.

We note further the filaments identified with `CRISPy` in B5 differ a bit from those identified with `FilFinder` (Koch & Rosolowsky, 2015) by S20 using the same data. While both methods identified filament *c* (i.e., *B5-Fil1*) as the same structure,

`FilFinder` identified filament *b* and the eastern half of filament *a* as a single structure (i.e., *B5-Fil2*) instead of two. The difference between the filaments identified with the two method seems to indicate that `CRISPy` performs better than `FilFinder` at detecting filaments over a higher dynamic range of brightness. Since `FilFinder` identify filaments based on their overall morphology rather than local topology, such as density ridges, it seems to have missed the valley between filament *a* and *b*, which are brighter than the average background in B5.

Since the four filamentary structures identified by `CRISPy` in PPV space do not overlap on the plane of the sky, we further divided B5 into topologically distinct regions based on the integrated intensity map of our best-fitted NH_3 model using the watershed method implemented in the `scikit-image` package (van der Walt et al., 2014). The watershed method segments multi-dimensional structures with isosurfaces that are shared by density peaks or 'seeds,' and have been widely adopted by algorithms such as the `CLUMPFIND` (Williams et al., 1994) and `CPROPS` (Rosolowsky & Leroy, 2006) to identify molecular cloud structures. To ensure the B5 clump is divided into regions defined by their respective filaments, rather than just any emission peak, we seeded the watershed segmentation with our identified filament spines. The boundaries resulting from the segmentation are indicated in Figure 3.6.

3.4.3 Velocity-coherent Maps

Given that we detected two-component emission only over a limited area in the VLA+GBT data, as illustrated by the black contour shown in Figure 3.6, we further sorted our two-component fits based on their kinematic similarities to the one-component-fitted surrounding pixels. The purpose of such sorting is to identify the modelled component that is kinematically continuous, i.e., velocity-coherent, across the entire B5 region between both the one- and two-component fits. We accomplished such sorting by first interpolating our $v_{\rm LSR}$ and σ_v maps derived from the one-component fits over the two-component-fitted regions as if they are empty. The interpolation is performed using a Gaussian kernel that is $\sigma_{\rm ker} = 0.25$ pixels in size to avoid degrading the image resolution significantly.

Once we obtained the interpolated one-component maps as a reference for velocity-coherence, we calculated kinematic similarities between each of the two-component-fitted components and the reference maps by first calculating the differences between the interpolated one component maps and their two-component counterparts for both

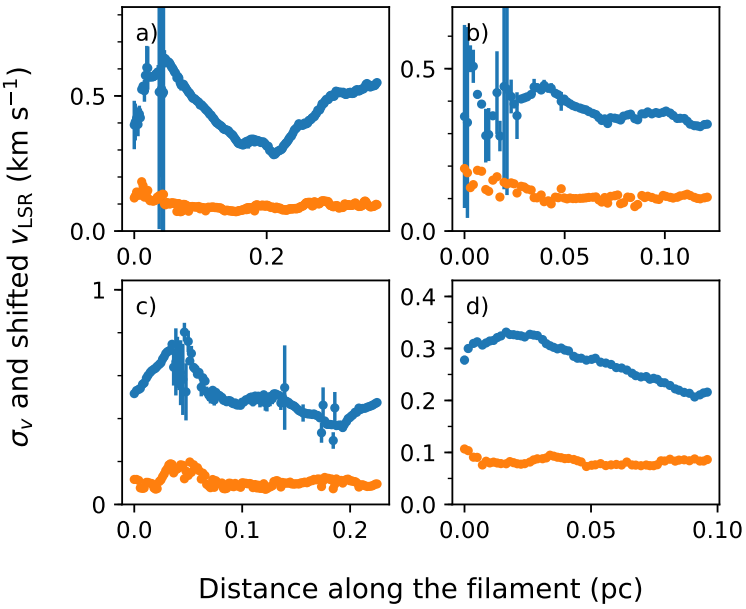

Figure 3.7: The shifted $v_{\rm LSR}$ (blue) and σ_v (orange) values of our final parameter maps along the four filament spines. The zero-point distance reference of the spine starts at the end closest to southeastern corner of the map, while the zero-point of the $v_{\rm LSR}$ shown is shifted arbitrarily to fit well within each panel.

the $v_{\rm LSR}$ and σ_v maps. We then take the quadrature sum of these difference maps of $v_{\rm LSR}$ and σ_v and use it as our metric for kinematic similarity.

The component determined to be most kinematically similar to the interpolated one-component fits is subsequently integrated into the one-component-only maps to form a final set of $v_{\rm LSR}$ and σ_v maps for our analysis. The center and right panels of Figure 3.6 show these sorted, final $v_{\rm LSR}$ and σ_v maps, respectively, overlaid with the same contours and symbols found in the left panel. The component we excluded from these final maps typically has estimated $v_{\rm LSR}$ errors at least twice those of their included counterparts, and have optical depths that are at least twice lower. Moreover, the $v_{\rm LSR}$ of the excluded component tends to form compact structures that are discontinuous from each other on the $10''$ scale, making them unsuitable for velocity gradient analysis. We henceforth exclude these kinematically less similar component from our analysis.

Figure 3.7 shows the (shifted) $v_{\rm LSR}$ and the σ_v taken from the final maps along our `CRISPy`-identified spines. With errors in both quantities taken into consideration, the sorted $v_{\rm LSR}$ and σ_v are reasonably continuous, indicating that we are indeed tracing

the kinematics of structures that are velocity coherent along their lengths. The abrupt increase in the estimated error in some instances results from two components at those locations having both similar $v_{\rm LSR}$ and σ_v values, with at least one of them being optically thick. Under these circumstances, the optically thicker component closer to the observer can easily eclipse the rear component, obscuring the kinematic information encoded in the shape of the spectrum. Visual inspections of the fitted spectra indeed show that fits with exceptionally large errors tend to have larger optical depths and small differences in $v_{\rm LSR}$ or σ_v between the two modeled components. Furthermore, these large error pixels tends to be found towards the centers of the densest structures (e.g., ridges) where the τ_0 values of both components often exceeds a value of 5 individually.

3.5 Discussion

In this section, we first discuss the kinematic behavior of the diffuse, supersonic gas in Section 3.5.1, followed by a high-resolution overview of the dense, subsonic filaments that embeds in this diffuse environment in Section 3.5.2. We further discuss the structural and kinematic radial profiles of these B5 filaments in Section 3.5.3, accompanied by a detailed look of B5's highly complex velocity gradients in Section 3.5.4.

3.5.1 Ambient environment

Our fits to the GBT-only data reveal that the entire subsonic region previously identified by P10 from their single-component fits are better modelled by two-component fits according to the AICc (see Section 4.3). When we sorted these fitted components by their σ_v and subsequently compared these sorted maps to their surrounding, single-component-fitted pixels (see Figure 3.3), we find by eye that the wider σ_v components resemble their surroundings better than their narrower σ_v counterparts do. This result holds true for both the derived σ_v and $v_{\rm LSR}$, which suggests the wide component detected with the GBT-only data indeed belongs to the diffuse ambient gas colloquially referred to as the 'cloud' (e.g., P10).

The kernel-estimated density distributions of the derived $v_{\rm LSR}$ and σ_v for each of these components (see Figures 3.4 and 3.5) further confirm that the kinematics of the wider σ_v component well resemble those single-component-fitted pixels outside of the

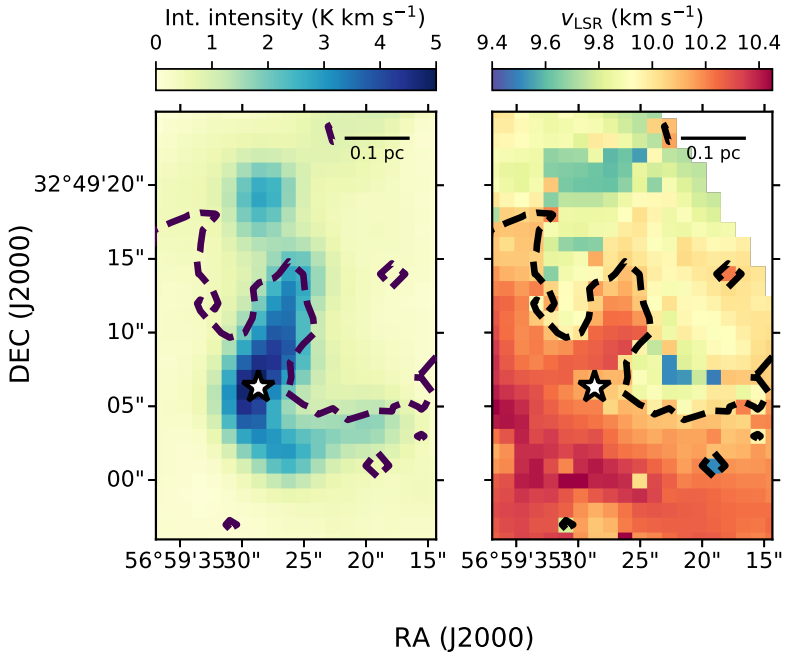

Figure 3.8: The integrated intensity (left) and the wide-and-only (i.e., ambient) component $v_{\rm LSR}$ (right) maps of the GBT-only observations of B5. The dashed line shows where $v_{\rm LSR} = 10.05$ km s^{-1}. The B5-IRS1 protostar marked by the star symbol and a physical scale bar are shown in both panels.

projected, sub-sonic region. The wide, mostly supersonic σ_v component thus seems to be tracing a supersonic, ambient gas that surrounds subsonic "islands of calmness" (Goodman et al., 1998) similar to those found spatially with both single-component (P10; Chen et al. 2019a) and multiple-component fits (Sokolov et al. 2018). With two-component fits to spatially averaged spectra, Choudhury et al. (2020) also found similar results in L1688, both spatially and spectrally (i.e., along lines of sight).

When taking spatial information further into account (see Figure 3.3), we found the $v_{\rm LSR}$ values of the subsonic region in B5 differ from those in its immediate surroundings in the north by $\gtrsim 0.2$ km s^{-1}. Assuming a 10 K gas temperature, such a difference indicates the subsonic structures in B5 are moving through their parental environment at a transonic or supersonic speed rather than along with it. Such a kinematic decoupling between the ~ 0.1 pc dense structures and their ambient surroundings may thus hint at a fairly dynamic origin for these dense structures, such as being produced by intersecting planar shock fronts (Pudritz & Kevlahan, 2013).

Interestingly, the wide and only components (i.e., the ambient component) in

the northwest and southeast of B5 seem to have $v_{\rm LSR}$ values that differ significantly. Figure 3.8 shows these $v_{\rm LSR}$ often differ by > 0.3 km s^{-1} and indeed transitions sharply between the two regions. Moreover, this transition seems to take place on the northern edges of the main B5 filaments, suggesting that the ambient gas of B5 may be a part of a larger-scale convergent flow or gravitational infall towards these filaments. The former scenario is expected to produce shock fronts while the latter, under the global hierarchical collapse scenario, do not (Vázquez-Semadeni et al., 2019). Considering the $v_{\rm LSR}$ transition here appears rather sharp, this transition likely indicates the presence of a velocity discontinuity resulted from a shock front. Furthermore, this transition exists far beyond the dense filaments, which indicates the inferred mass flows are unlikely driven by the gravitational potential of the local structures. Further study with shock tracers, such as SiO lines or higher J rotation-transition lines of CO (e.g., Pon et al. 2012), may be able to confirm the existence of a shock front at this sharp $v_{\rm LSR}$ transition, especially if the deprojected velocity difference between the flows is much larger than their observed, line-of-sight counterpart (i.e., ~ 0.3 km s^{-1}).

3.5.2 Dense, subsonic structures

As first revealed by P11, the dense, subsonic region in B5 is not a monolith. In fact, the subsonic region commonly referred to as a 'core' actually consists of several filaments. With `CRISPy` (Chen et al. 2020c), we identified four distinct filaments in B5 and designated them as *a* to *d*.

While the B5 filaments have been described as 'fibers' (e.g., André et al. 2014), a term first introduced by Hacar et al. (2013) to describe kinematically distinct but spatially unresolved bundles of sub-filaments, we will refer to them simply as filaments in this work. In particular, the fibers observed by Hacar et al. (2013) in Taurus with C^{18}O may not necessarily correspond to physical, three-dimensional filaments due to complex gas kinematics typically traced over intermediate density environments with species such as CO (e.g., Zamora-Avilés et al. 2017; Clarke et al. 2018b). And though the partial overlap resolved spatially between filaments *b* and *c* may resemble those found spectrally by Hacar et al. (2013), such an overlap is not typically found with denser gas tracers, such as NH_3 and N_2H^+ (e.g., Tafalla & Hacar 2015, Hacar et al. 2017, Hacar et al. 2018, Chen et al. 2020c).

Due to their smaller beam, the VLA+GBT data are inherently less sensitive than

the GBT-only data to the well-resolved, low surface brightness emission, even though the GBT data have been combined with the interferometric VLA measurements to recover large-scale emission. For that reason, we only detect one- and two- component spectra in the VLA+GBT data over a smaller area compared to where their GBT-only counterparts are detected. Nearly all the two-component spectra in the VLA+GBT data are detected in the filaments, where the emission is brightest.

The majorities (i.e., 63%) of the wide and only components detected in the VLA+GBT data tend to have σ_v values that are subsonic (i.e., < 0.2 km s^{-1}), unlike their GBT-only, supersonic counterparts (see also Figure 3.5). Such a result is consistent with the findings of P11 using less sensitive VLA+GBT observations of B5, where they only detected subsonic gas with their one-component fits. The fact that both components we detect with the VLA+GBT data are mostly subsonic suggests that at least three NH_3 components exist along lines of sights towards the B5 filaments: two subsonic, spatially compact components and one additional supersonic, ambient component detected only by the GBT-only data. The non-overlapping detection of two out of the three components likely results from VLA+GBT and GBT-only data having different sensitivities toward different spatial scales. As mentioned earlier, we excluded the second component detected with the VLA+GBT data due to them having larger fitting errors and being frequently velocity discontinuous over the scale of a filament.

3.5.3 Radial Profiles

Radial integrated intensity profiles

Figure 3.9 shows the NH_3 integrated intensity radial profiles of all four B5 filaments measured along the direction perpendicular to the filament spines. The solid lines show the median value of the profile while the shaded region represents the 25- and 75-percentile ranges. We only included pixels within the watershed boundaries of each filament for the respective profiles to ensure that contributions associated with unrelated filaments along each line of sight are minimized. Such a practice is important for filaments that are close in proximity to each other on the plane of the sky, particularly given that filaments are known to have non-negligible, power-law like profiles at larger radii (e.g., Arzoumanian et al. 2011).

We fitted the radial integrated intensity profiles of each filament with a Plummer-like functions (see Plummer 1911; Whitworth & Ward-Thompson 2001; Nutter et al.

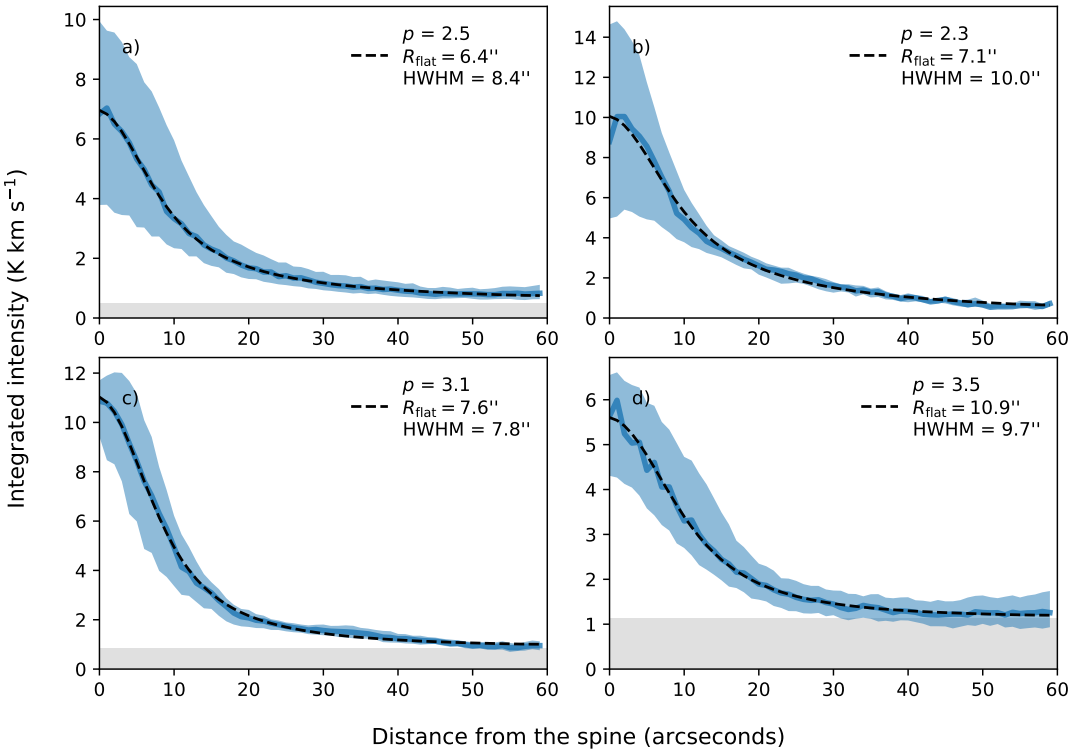

Figure 3.9: Radial profiles of the NH_3 integrated intensity for the B5 filaments. The blue solid lines show the median value of the profiles while the blue shaded regions represent the 25- and 75-percentile ranges of the profile. The black dashed lines represents the best-fitted Plummer-like models.

2008; Arzoumanian et al. 2011), i.e.,

$$I(r) = I_0 \left[1 + (r/R_{\rm flat})^2\right]^{\frac{1-p}{2}} + I_{\rm bg}, \tag{3.5}$$

where r is the radial distance from the filament spine, $R_{\rm flat}$ is the radius of the flat inner region, and p is the power-law index of the outer region. Furthermore, I_0 and $I_{\rm bg}$ are the integrated intensities of the filament spine and the background emission, respectively. To emulate the VLA+GBT observations, we convolved the Plummer-like functions with a 6″ full width at half maximum (FWHM) Gaussian beam prior to the fitting. For us to interpret integrated intensity as a proxy for gas column density, we assume the observed NH_3 emission is optically thin and does not have widely varying temperature. In the case where the best-fit $I_{\rm bg}$ reaches the lower limit of our model, zero, we refit the Plummer-like profile with $I_{\rm bg}$ fixed at zero to determine the covariance matrix of our fit for error estimates.

Figure 3.9 shows the Plummer-like function best-fitted to the integrated intensity profiles of filaments in B5. The best-fitted p values for filaments a, b, c, d are 2.5 ± 0.1, 2.3 ± 0.1, 3.1 ± 0.1, and 3.5 ± 0.4, respectively. For a comparison, P11's earlier NH_3 measurements with less-sensitive VLA+GBT observations showed that the Plummer function with p fixed at 4 fits the radial profile of filament c in B5 better than one with p fixed at 2. Being able to identify emission ridges (i.e., filament spines) precisely with `CRISPy` allows us to improve upon P11's box-averaged measurements substantially. Moreover, by using the watershed method to define inter-filament boundaries, we are able to extend further the radial measurements confidently out to $r = 60''$ (i.e., ~ 0.09 pc) compared to the $r = 30''$ limit used by P11. Interestingly, but perhaps unsurprisingly, our measured radial profiles resemble beam-convolved Plummer-like functions remarkably better than those previously measured by P11 using the box-averaged method, which inevitably smeared out the true radial profiles.

Using the same VLA+GBT observations as analyzed here, S20 (submitted) also made filament width profile measurements with individual perpendicular cuts across B5 filaments. The average best-fit p values they measured across the individual cuts in their filaments *B5-fil1* and *B5-fil2* are 3.4 and 3.5, respectively, and their best-fitted p values for the profiles averaged over the entire filament of *B5-fil1* and *B5-fil2* are 2.91 ± 0.06 and 2.98 ± 0.05, respectively. The p value they measured over the averaged profile of *B5-fil1*, i.e., our filament c, is very consistent with ours. Their measurement of p for *B5-fil2*, on the other hand, is higher than we find in filaments a and b, its rough counterparts. The fact that S20 identified filaments b and half of filament c combined as a single filament is likely the primary cause of this discrepancy between the measurements.

The $p \geq 3$ Plummer-like fits we find for filaments c and d are higher than those generally found in studies conducted with dust continuum (e.g., Arzoumanian et al. 2011) and CO emission (e.g., Panopoulou et al. 2014; **?**) observations, which found profiles that are better fitted with $p = 2$ than $p = 4$ functions. Similarly, studies that fit Plummer-like function with a free-floating p also find best-fit p values to be closer to 2 rather than 4, both in observations (e.g., Arzoumanian et al. 2019) and simulations (e.g., Smith et al. 2014). While dense gas tracers, as pointed out by Arzoumanian et al. (2019), can in principle have steeper power-law wings that give rise to higher p values due to their insensitivity towards more diffuse, lower-density gas and dust, such an interpretation does not fully explain why filament a and b have best-fit p values closer to 2.

The FWHM filament widths we measure from our best-fit radial profiles of filaments *a*, *b*, *c*, and *d* are 0.025 ± 0.01 pc, 0.029 ± 0.02 pc, 0.023 ± 0.01 pc, and 0.028 ± 0.03 pc, respectively. While these widths are significantly smaller than the ~ 0.1 pc widths commonly found with dust emission studies (e.g., Arzoumanian et al. 2011; André et al. 2016; Arzoumanian et al. 2019), they are nevertheless very similar to those found with ALMA observations of dust continuum emission in IRDC G035.39-00.33 (~ 0.028 pc; Henshaw et al. 2017), as well as VLA NH_3 (~ 0.02 pc; Monsch et al. 2018) and ALMA N_2H^+ (~ 0.035 pc; Hacar et al. 2018) observations of Orion A. Moreover, though ~ 0.1 pc widths have also been found in simulations (e.g., Federrath 2016), significantly narrower widths in the $0.02 - 0.04$ pc range are also common in simulations (e.g., Juvela et al. 2012; Chen et al. 2020a; Heigl et al. 2020). We note that unlike many of the dust continuum studies, we measure our FWHM filament widths directly from the fitted function, i.e., nonparametrically, rather than inferring them from the fitted $R_{\rm flat}$ parameter through a power-law-dependent scaling factor.

Similar to the ALMA dust continuum and N_2H^+ emission measurements made by Henshaw et al. (2017) and Hacar et al. 2018, respectively, the ~ 0.03 pc FWHM filament widths we find in B5 are about a factor of three smaller than the ~ 0.1 pc width typically found with single-dish, dust continuum studies, which have spatial resolutions $\sim 3 - 4$ times lower than that of the VLA data (e.g., Arzoumanian et al. 2011; André et al. 2016; Arzoumanian et al. 2019). The fact that the ~ 0.03 pc widths have been observed in dust continuum studies, with extended emission recovered (Henshaw et al. 2017), suggests that the ~ 0.03 pc widths measured with denser gas tracers such as NH_3 and N_2H^+ may not be necessarily biased significantly by the smaller volumes these molecular species trace relative to those traced by dust.

While no one-to-one comparisons have yet been made in Orion between filaments identified with N_2H^+ (Hacar et al. 2018) and $C^{18}O$ (**?**), where observations were obtained at comparable resolutions (i.e., 0.01 pc and 0.015 pc, respectively), it is worth noting that the $C^{18}O$ measured widths are typically consistent with the widely reported value of ~ 0.1 pc measured with lower resolution observations. The range of these $C^{18}O$ measured widths, however, is relatively large and their lower-end value (i.e., 0.02 pc) overlaps with the 0.035 pc widths typically measured there with N_2H^+ emission. Furthermore, $C^{18}O$ can become optically thick or chemically depleted at higher column densities, potentially flattening the inner regions to give rise to larger widths.

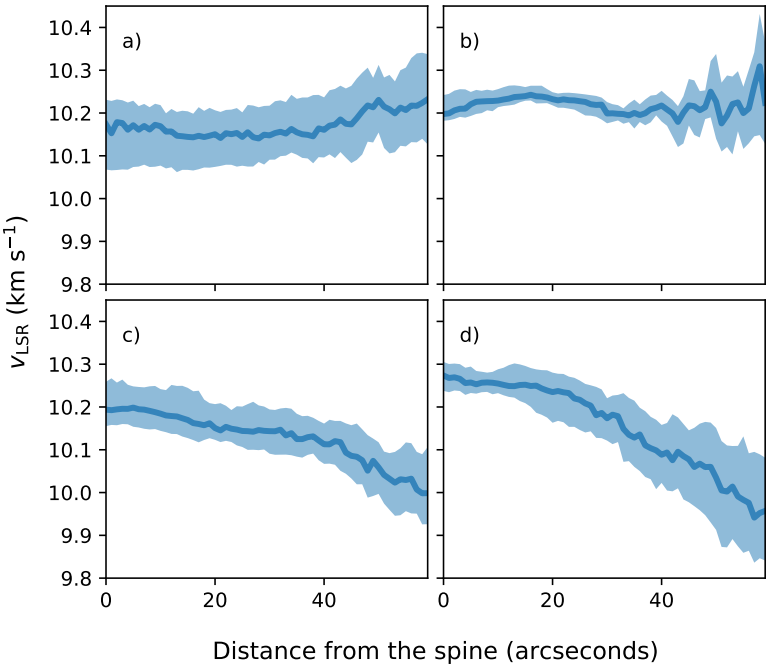

Figure 3.10: Radial profiles of $v_{\rm LSR}$ for the four B5 filaments. The solid lines show the median value of the profiles while the shaded regions represent the 25- and 75-percentile ranges of the profile.

Radial kinematic profiles.

Figure 3.10 shows the $v_{\rm LSR}$ radial profiles of the four B5 filaments. While $v_{\rm LSR}$ values of the southern filaments, i.e., *a* and *b*, remain relatively constant at all projected radii, the $v_{\rm LSR}$ values of the northern filaments, i.e., *c* and *d*, show clear downward trends (to lower velocities) at larger radii. An examination of our final $v_{\rm LSR}$ map shown in Figure 3.6 reveals that most of these lower $v_{\rm LSR}$ pixels reside on the western and northern outskirts of B5, well outside the central subsonic region. As discussed earlier in Section 3.5.1 based on the $v_{\rm LSR}$ map derived from the GBT-only data (see Fig. 3.3), these low $v_{\rm LSR}$ values seem to belong to a population of supersonic, ambient gas that surrounds the subsonic region in B5, both on the plane of the sky (see also P10) and along the line of sight (see Section 3.5.1).

Figure 3.11 shows the radial σ_v profiles of the B5 filaments. They tend to increase monotonically towards larger radii and typically become supersonic at radii $> 40''$, i.e., ~ 0.06 pc. For filaments *c* and *d*, these radii are also where the $v_{\rm LSR}$ values start to deviate from the center by > 0.2 km s^{-1}, roughly the sound speed of 10 K gas. Incidentally, the 0.06 pc radius is also about where the background emission starts

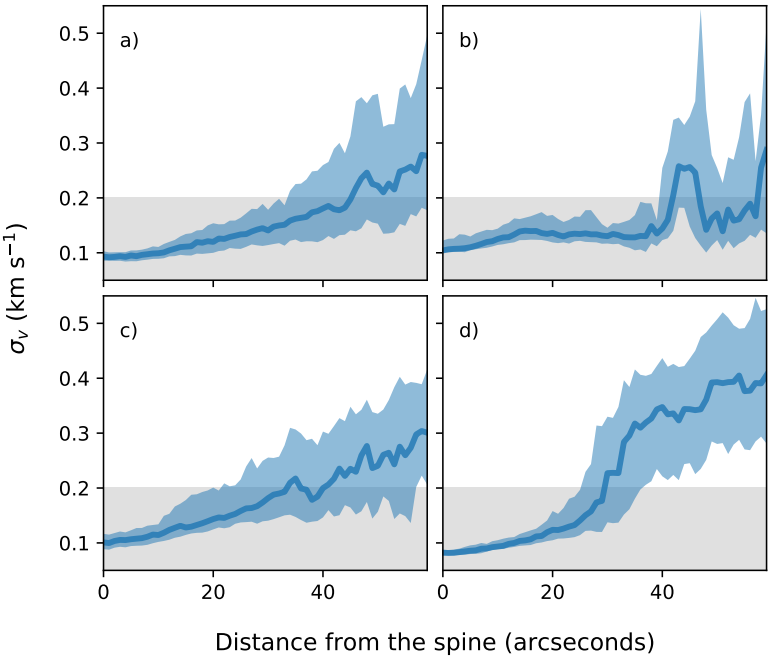

Figure 3.11: Radial profiles of σ_v for the four B5 filaments presented in the same way as Figure 3.10. The grey shaded region shown where the σ_v should be if its none-thermal component is subsonic.

to dominate over that of these two filaments according to our best-fit Plummer-like function (Eq. 3.5). This transition can be seen in Figure 3.9 where the grey shaded regions plotted over the integrated intensity profiles represent the background emission derived from our best-fit Plummer-like model. We note that filament *b* is best-fitted with no background.

The fact the σ_v measured in B5 tends to be supersonic where the background emission dominates over the filaments suggests the sharp increase of σ_v seen towards filament *d* around $r = 30''$ in Figure 3.11 is unlikely a physical feature inherent to that filament. The apparent σ_v transition we see, as inferred from the one-component fits, likely results from the ambient emission being picked up by the spectral fitting routine as it starts to dominate. Indeed, filament *d* has the lowest emission contrast relative to its background in B5, which can make such a transition more pronounced than is seen for the other filaments.

The transition between where ambient emission dominates over that from subsonic structures is also likely responsible for the sharp sonic transitions reported by studies of NH_3 emission fit with single components (e.g., P10; Chen et al. 2019a; Chen et al.

2020b). Indeed, our two-component fits to P10's GBT observation of B5 suggest that the second, supersonic components previously not captured towards the subsonic region belong to the ambient gas that surrounds the subsonic structures (see Section 3.5.1). Sharp sonic transitions thus appear in single-component fits whenever a bright, subsonic component dominates over an otherwise smooth, supersonic background.

While the σ_v profiles of the four filaments observed in B5 do not necessarily share a general shape, they all tend to increase monotonically towards larger projected radii. Filament b is the only exception, where its σ_v values rise sharply around $r = 40''$ before returning to their earlier values around $r = 50''$. Visual examination of the σ_v map shown in Figure 3.6 reveals that the high σ_v values seen towards these radii largely come from pixels located in the 'valley' between filaments b and c. The sharp drop in σ_v for filament b at $r \sim 50''$ is subsequently caused by the exclusion of pixels west of filament b by the watershed definition at $r \lesssim 50''$. We did not find any combined spatial and spectral correlation between the outflows driven by B5-IRS1 and the high σ_v regions, suggesting the higher σ_v values seen towards the 'valley' are related to the outflows. Instead, such high σ_v regions may be associated with ongoing infall towards the protostar.

The σ_v values found within 2 half widths at half maximum (HWHM) of the B5 filaments (i.e., $r \sim 20'' = 0.03$ pc) all tend to increase linearly overall. The only exception is found in filament b, where the profile appears fairly flat in the radial range of $15'' - 40''$. These flat or increasing trends appear consistent with those measured for subsonic cores in Taurus B18 and Ophiuchus L1688 with single-component fits by Chen et al. (2019a), which are marginally resolved at a 0.03 pc scale by the GBT beam (~ 0.02 pc in those clouds).

Interestingly, the fiducial model of an accreting filament in hydrodynamic simulations conducted by Heigl et al. (2020) also yields a radial σ_v profile that increases linearly with radius during various time-steps of their simulation. For example, the radial profile of their fiducial model taken at $t = 0.5$ Myr, when its radius is roughly at its maximum, has a best-fitted Plummer-like profile with $p = 3.86$ and a FWHM value of ~ 0.03 pc. These values are similar to those we measure in B5, and differ significantly from the typical FWHM ~ 0.1 pc and $p \sim 2$ widely reported by dust-continuum studies (e.g., Arzoumanian et al. 2011). If this model does indeed describe well the actual filament we observe, then the linear correlation between σ_v and the projected radii we observed in B5 can be attributed to accretion-driven turbulence. Under the model by Heigl et al., the anti-correlation between turbulence and gas

density does not produce a radial turbulent pressure gradient and consequently the turbulence cannot provide additional radial support against gravity.

Alternatively, if the radial inward motion of a filament takes the form of $v\,(r) \propto -r$ that describes the flat density inner regions of a gravitationally contracting, prestellar core (e.g., Whitworth & Summers 1985), then the linear correlation between σ_v and the projected radii we observed may be due to infall motions, rather than turbulence. Indeed, Vázquez-Semadeni et al. (2019) have proposed such an interpretation for similar σ_v trends seen towards subsonic dense cores (e.g., Chen et al. 2019a). Since the Plummer-like profile well describes density structures of prestellar cores and filaments alike, with $r < R_{\rm flat}$ corresponding to the flat inner region (e.g., Whitworth & Ward-Thompson 2001), an extrapolation of such an interpretation to filaments is not unreasonable. Synthetic observations of simulations with resolution comparable to our data (i.e., 0.009 pc) are needed to test such an interpretation by confirming whether or not the infall motions proposed by Vázquez-Semadeni et al. (2019) can remain unresolved as σ_v and produce radial profiles similar to those shown in Figure 3.11.

3.5.4 Velocity Gradients

Following C20, we calculate the velocity gradient, $\nabla v_{\rm LSR}$, of our final, velocity-coherent $v_{\rm LSR}$ map at each pixel by least-square fitting a plane over the $v_{\rm LSR}$ values found within a circular aperture centered on the pixel. The diameter of the aperture is 10 pixels wide, about twice the beam size, to ensure we measure gradients over well-resolved structures. The resulting $\nabla v_{\rm LSR}$ calculated for B5 reveals a highly complex field expected from neither a body of subsonic gas nor simple accretions. To well capture such complexity without reducing it to simple statistics, we focus much of our $\nabla v_{\rm LSR}$ discussion here on descriptive analyses.

Figure 3.12 shows the resulting $\nabla v_{\rm LSR}$ visualized as line integral convolution (LIC; Cabral & Leedom 1993) textures, overlaid on the integrated intensity map (left) and the $\log|\nabla v_{\rm LSR}|$ map (right) of our VLA+GBT observations of B5. The LIC technique visualizes a vector field as a texturalized image akin to iron filings tracing a magnetic field, which is effective at visualizing densely populated fields with which traditional visualization methods struggle. We use the `LicPy` software for our LIC visualizations (Rufat, 2018).

Interestingly, the local $\nabla v_{\rm LSR}$ field tends to be well ordered in the brightest (i.e.,

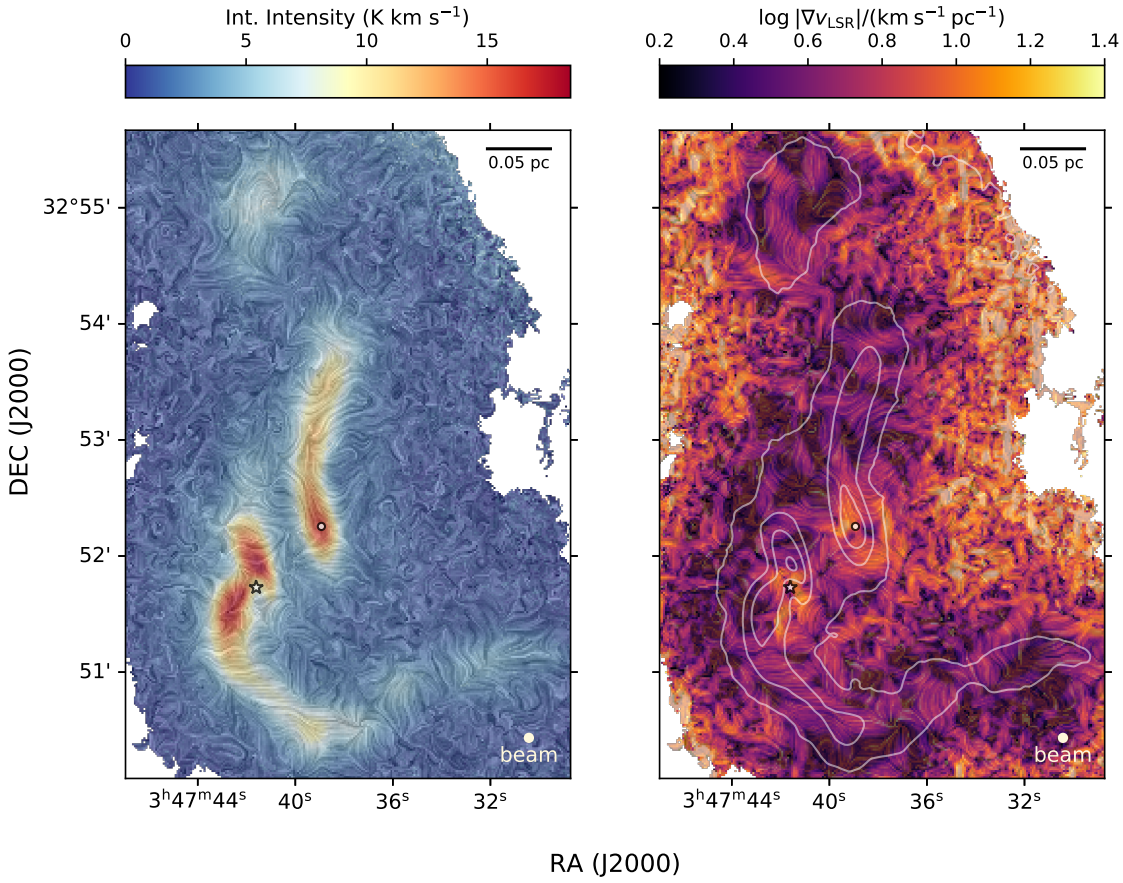

Figure 3.12: Line integral convolution of the $\nabla v_{\rm LSR}$ field overlaid on the integrated intensity map derived from our NH_3 fits (left) and the $\log|\nabla v_{\rm LSR}|$ map (right). The white contours show where the modelled integrated intensity are at 2.5 K km s^{-1}, 7.5 K km s^{-1}, 12.5 K km s^{-1}, and 17.5 K km s^{-1}, respectively. The IRS1 protostar and the *B5-Cond1* condensation are marked with the star and the circle symbol respectively. The beam of the data and the physical scale bar are shown in both panels.

densest) parts of the four B5 filaments, and becomes increasingly less organized further away from them. The $\nabla v_{\rm LSR}$ orientations tend be the same on the $\sim 30''$ (i.e. ~ 0.04 pc) scales within or near the filaments and remain relatively consistent throughout the lengths of the shorter filaments (i.e., *b* and *d*) but not their longer counterparts (i.e., *a* and *c*). The southeastern segment of filament *a*, for example, prominently features a well-ordered $\nabla v_{\rm LSR}$ that runs across the filament at about a 45° angle relative to the spine.

The $\nabla v_{\rm LSR}$ orientations at the fainter, western end of filament *a* and the brighter southern end of filament *c* also seem to vary according to their radial distance from

the spine. Specifically, the $\nabla v_{\rm LSR}$ at these locations tend to run perpendicular with respect to the filament at larger radii and become parallel as they get closer to the filament spines. While the observed $\nabla v_{\rm LSR}$ may not necessarily map well onto the underlying, three-dimensional velocity fields, these radial trends do qualitatively resemble those seen in simulations by Gómez & Vázquez-Semadeni (2014). In their simulations, which do not account for magnetic fields, gas tends to fall perpendicularly onto the filament and then starts to flow in parallel with the spine. We note, however, that the morphology of such a velocity field in projection may not necessarily imprint itself well onto the observed $\nabla v_{\rm LSR}$, which measures the acceleration/deceleration of line-of-sight velocities.

The right panel in Figure 3.12 shows the LIC visualization of $\nabla v_{\rm LSR}$ plotted over its log magnitude ($\log|\nabla v_{\rm LSR}|$) map. Interestingly, the locations of B5 closer to filaments tend to contain 'bands' of high $|\nabla v_{\rm LSR}|$ structures that are often $\sim 10'' - 20''$ in width and $\sim 60'' - 120''$ in length. Furthermore, the $\nabla v_{\rm LSR}$ is very ordered within these high $|\nabla v_{\rm LSR}|$ bands, usually running along the same direction within each band. The locations of these band-like $|\nabla v_{\rm LSR}|$ structures do not correlate well with the bright (i.e., high column density) structures seen in the integrated intensity map, except for filament *a*.

Figure 3.13 shows the $\nabla v_{\rm LSR}$ measured in B5 decomposed into components that are perpendicular (i.e., $\nabla v_{\rm LSR,\perp}$; left panel) and parallel ($\nabla v_{\rm LSR,\parallel}$; right panel) to the filament spines (black lines) within their respective watershed boundaries (white lines). We accomplished this decomposition using the technique developed by Chen et al. (2020c). The total magnitudes of the non-decomposed $\nabla v_{\rm LSR}$ are shown in the right panel. By the convention set by Chen et al. (2020c), positive $\nabla v_{\rm LSR,\perp}$ values point away from the filament spines and vice versa for the negative values. By the same convention, positive $\nabla v_{\rm LSR,\parallel}$ values point away from the end of the filament furthest away from the image origin, i.e., the southeastern corner, and vice versa for negative values.

Figure 3.13 shows that the $\nabla v_{\rm LSR}$ maps of B5 contain a wealth of small-scale, beam-resolved structures within $\sim 40''$ of the filament spine. The typical values of these compact structures in both the perpendicular and parallel directions are in the range of $1 - 5$ km s^{-1} pc^{-1}. While the $\nabla v_{\rm LSR}$ at locations beyond $\sim 40''$ is also rich in structures, the typical widths of these structures and the typical distances between them, however, appear to be around the size of our $6''$ beam. Examination of the B5 $\nabla v_{\rm LSR}$ field with LIC (see Figure 3.12) further reveals that $\nabla v_{\rm LSR}$ orientations in

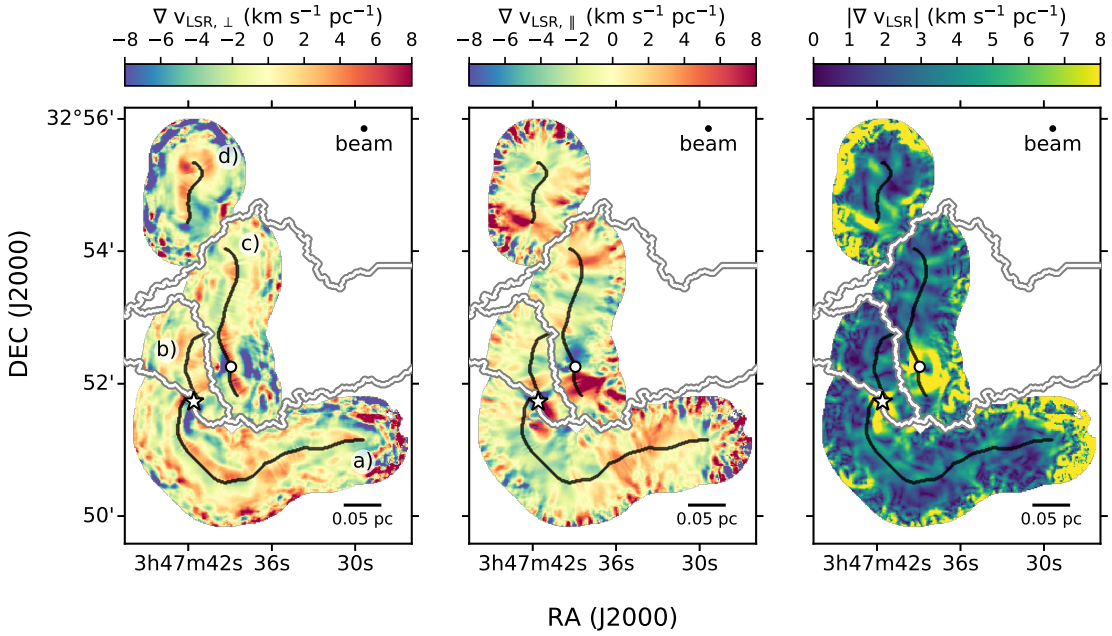

Figure 3.13: The spatial distributions of the perpendicular and parallel components of $\nabla v_{\rm LSR}$ in B5, measured relative to the four filament spines (black), shown in the left and center panels, respectively. The decomposition of the $\nabla v_{\rm LSR}$ into its two components is performed within the watershed boundaries (white) of their associated spines. The spatial distribution of the total $\nabla v_{\rm LSR}$ magnitude is shown in the right panel. The IRS1 protostar and the *B5-Cond1* condensation are marked by the star and circle symbols, respectively. The beam of the data and a physical scale bar are shown in all panels.

these regions are highly disordered. For this reason, we do not include $\nabla v_{\rm LSR}$ values from locations more than $\sim 40''$ away from the filament spines in our analysis and these locations have been masked out in Figure 3.13.

Within $40''$ of filament spines, we find no discontinuities between any of the filaments in B5. As a result, these filaments likely belong to the same parental, subsonic structure. The lack of $v_{\rm LSR}$ discontinuity between filaments also indicates that our kinematic analysis does not depend sensitively on the location of the watershed-defined borders that divides the faint, inter-filamentary gas.

The lack of $v_{\rm LSR}$ differences between the B5 filaments (see Figure 3.10) also contrasts greatly with kinematic behaviour of sub-filamentary fibers observed in Taurus with $C^{18}O$ by Hacar et al. (2013), which have supersonic levels of $v_{\rm LSR}$ differences in magnitude ($\gtrsim 0.4$ km s^{-1}) between them. Similarly, fibre-like 'sub-filaments' seen in simulations by Clarke et al. (2017) also have supersonic levels of line-of-sight velocity

differences ($\sim 0.5-2$ km s^{-1}). The filaments we find in B5 may thus represent objects that are either evolutionarily or intrinsically different from fibre-like features found in both observation and simulations.

Perpendicular velocity gradient

The $\nabla v_{\rm LSR,\perp}$ values measured in B5 tend to form elongated structures near the filament spines, often running parallel to the spines (see Figure 3.13). These $\nabla v_{\rm LSR,\perp}$ structures typically have magnitudes of $5-8$ km s^{-1} pc^{-1} and have opposite signs on the two sides of the spines, which indicates that the $\nabla v_{\rm LSR,\perp}$ field at those locations runs through, i.e., across, their respective filament spines rather than towards or away from the spines, as per the convention. The widths of these structures are typically about $8-12''$ and the $|\nabla v_{\rm LSR,\perp}|$ values of these structures are relatively constant throughout the structures.

If we assume a planar-like accretion geometry, such as that illustrated by Dhabal et al. (2018; see their Figure 15), and a $v(r) \propto -r$, prestellar-core-like, infall profile (e.g., Whitworth & Summers 1985), then we should expected a constant velocity gradient across the filament spine, i.e., $\nabla v_{\rm LSR,\perp} \propto -$constant. Specifically, we should see such a profile within the flat-density, inner regions of the filament, i.e., at radii where the assumed infall would hold for prestellar cores. Indeed, the typical $\sim 10''$ widths of $\nabla v_{\rm LSR,\perp}$ structures we found near the spines are comparable to the $R_{\rm flat}$ values we derived from the best-fit Plummer-like filament profiles ($\sim 6-11''$), suggesting that these observed $\nabla v_{\rm LSR,\perp}$ are signs of mass infall. Considering that planar-like accretion flows are commonly found in theoretical models, ranging from sheets fragmenting into filaments (e.g., Miyama et al. 1987) to post-shock accretion flows along magnetic fields (e.g., Chen & Ostriker 2014b, Chen & Ostriker 2015b), a planar-like geometry for such infall is plausible.

Interestingly, elongated, high $\nabla v_{\rm LSR,\perp}$ structures are not always symmetrically found on both sides of spines. For example, the eastern half of filament *a* exhibits such a structure only on its northwestern side. Furthermore, these elongated, high $\nabla v_{\rm LSR,\perp}$ structures are not always found near spines. Several are found at larger radii, i.e., $r \gtrsim 10''$, often running parallel to those adjacent to the spine but with an opposite sign. Such 'secondary' $\nabla v_{\rm LSR,\perp}$ structures can be found in the eastern segment of filament *a* and the southern segment of *c*. Indeed, the occurrence of the elongated $\nabla v_{\rm LSR,\perp}$ structures running parallel to the filament spines with signs that

alternate with radial distance is rather peculiar. Such behaviour is not expected from infall velocities that increase or decrease monotonically with radial distance, such as those commonly found in analytical models (e.g., Whitworth & Summers 1985). Moreover, prestellar-core-like infall (e.g., Whitworth & Summers 1985) outside the flat-density regions are expected to have a constant velocity, which should produce zero velocity gradient, contrary to what we found in B5.

Recent numerical simulations by Clarke et al. (2017) show an accreting filament with line-of-sight velocity structures that are qualitatively similar to those we find in B5. Specifically, the morphology and orientation of the velocity structures in these simulations is suggestive that their respective $\nabla v_{\mathrm{LSR},\perp}$ structures are also elongated and relatively parallel to the spine. Moreover, the expected $\nabla v_{\mathrm{LSR},\perp}$ from such a velocity field would also be asymmetrically distributed about the filament spines with alternating signs in the radial direction, much like what we see in B5.

In the simulation by Clarke et al. (2017), these elongated $\nabla v_{\mathrm{LSR},\perp}$ structures arise out of the vorticity of gas motions, i.e., $\omega \equiv \nabla \times \mathbf{v}$, that runs predominantly parallel to the filament spines, likely driven by the radial accretion of an inhomogeneous (e.g., clumpy) flow onto the filament. If such vorticity is indeed responsible for the $\nabla v_{\mathrm{LSR},\perp}$ observed in B5, then perhaps the partial, parallel overlap between filament b and c results from a process similar to the "fray" step of the "fray and fragment" fiber formation scenario proposed by Tafalla & Hacar (2015). The v_{LSR} differences between the individual B5 filaments ($\lesssim$ 0.2 km s^{-1}), however, are much smaller than those expected in the "fray and fragment" scenario. Indeed, the line-of-sight velocity differences between fibers found in observations (e.g., Hacar et al. 2013) and the sub-filaments found in the simulations (e.g., Clarke et al. 2017) are mostly supersonic. Further theoretical work is thus needed to determine if such discrepancies can be reconciled via filament properties such as mass or age. For example, the simulations by Clarke et al. (2017) involve initial conditions resembling filaments that are generally more massive than those found in our B5 observations (i.e., Kirk et al. 2013b, Palmeirim et al. 2013). Having initial conditions that better represent the B5 filaments in models are therefore needed to resolve whether or not the apparent tension between the v_{LSR} differences observed in B5 and the earlier simulations by Clarke et al. (2017) can be resolved.

Parallel velocity gradient

The $\nabla v_{\mathrm{LSR},\parallel}$ map shown in Figure 3.13 (center) also contains a wealth of small-scale structures. The morphology of these structures, however, are less well defined than their $\nabla v_{\mathrm{LSR},\perp}$ counterparts in general. The typical magnitudes of these $\nabla v_{\mathrm{LSR},\parallel}$ structures are about $3-6$ km s^{-1} pc^{-1}.

Two prominent, opposite-signed $\nabla v_{\mathrm{LSR},\parallel}$ structures can be seen towards the southern end of filament *c*, possessing the highest $\nabla v_{\mathrm{LSR},\parallel}$ magnitudes found in B5 (i.e., $5-12$ km s^{-1} pc^{-1}). These two structures are located adjacent to each other, centered around the *B5-Cond1* 'condensation' identified by P15 from these same data. The boundary between these two adjacent $\nabla v_{\mathrm{LSR},\parallel}$ structures are spatially correlated with *B5-Cond1*'s emission peak, indicating the v_{LSR} values measured in filament *c* are locally increasing towards the emission peak from both sides. Examination of the v_{LSR} map around this location (see Figure 3.3) confirms that the v_{LSR} values in the southern half of filament *c* are indeed higher in *B5-Cond1* than in its surroundings, by as much as 0.15 km s^{-1}.

While a spatial association between $\nabla v_{\mathrm{LSR},\parallel}$ and a density peak may indicate flow towards a dense core along the filament axis, the sign flip we observe at the emission peak is unexpected in such an interpretation. For example, if we model a filament as a cylinder inclined towards the observer (e.g., Figure 16 by Dhabal et al. 2018), then infall flow towards a dense core with a $v\,(r) \propto -r$ profile (e.g., Whitworth & Summers 1985) along the filament axis would produce a constant $\nabla v_{\mathrm{LSR},\parallel}$ across the core without a sign change. In fact, any infall velocity profile that increases monotonically away from the center of a dense core should not produce a sign change in $\nabla v_{\mathrm{LSR},\parallel}$ across the center of the core.

We speculate that the sign change in $\nabla v_{\mathrm{LSR},\parallel}$ across *B5-Cond1* indicates the southern end of filament *c* is curved towards our line of sight in three-dimensions. Considering that all four B5 filaments are somewhat curved on the 0.1 pc dense core scale ($\sim 60''$), the assumption these filaments are straight on this scale may indeed be poor. In this case, the observed $\nabla v_{\mathrm{LSR},\parallel}$ may correspond to longitudinal infall towards *B5-Cond1* along a filament that is curved such that the two ends of *B5-Cond1* are either both inclined towards or away from the observer.

Simulations by Smith et al. (2016) showed line-of-sight (LOS) velocity profiles along filaments that can produce $\nabla v_{\mathrm{LSR},\parallel}$ features that change signs across the center of a core. For example, two out of four cores along a series of connected sub-filaments

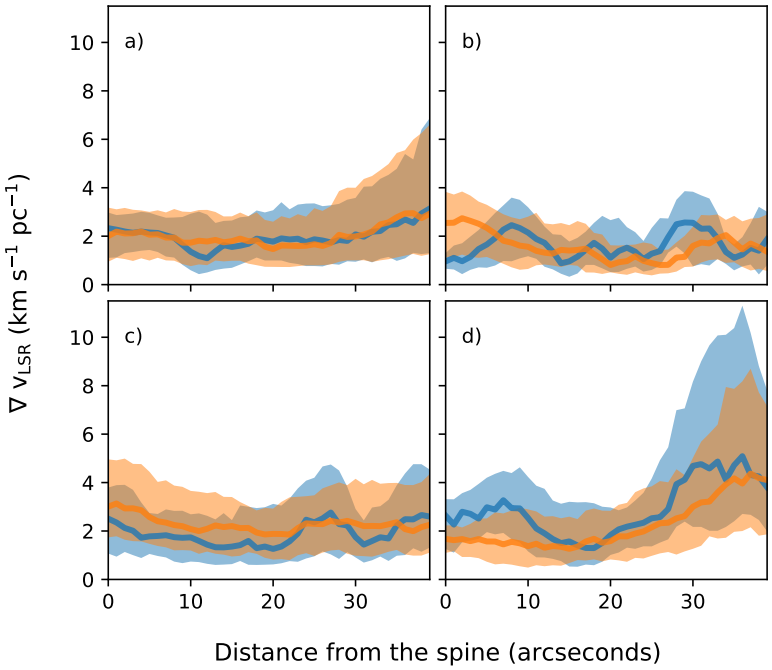

Figure 3.14: The radial profiles of $|\nabla v_{\mathrm{LSR},\perp}|$ (blue) and $|\nabla v_{\mathrm{LSR},\parallel}|$ (orange) of the four filaments identified in B5 with the solid lines showing the median values while the shaded regions show the 25- to 75-percentile ranges.

in their *S1F1T303* snapshot show a 'U' shape LOS velocity profile that would produce such a sign change. On the other hand, the LOS velocity profiles of the other two cores appeared fairly linear, which is consistent with the velocities expected from a relatively straight filament with a $v\,(r) \propto -r$ infall profile.

The sub-filaments found in simulations by Smith et al. (2016) contain many curves on the ~ 0.1 pc scale, similar to what we find in B5. While Smith et al. (2016) did not explicitly indicate where most of their cores are located in their three-dimensional simulations, they did note the locations of a few protostellar cores, i.e., cores that contain a sink particle. The one protostellar core found in their *S1F1T303* snapshot, in particular, is indeed located at a significantly curved location of a sub-filament. This particular curve, however, does not seem to locally orient both ends of the core towards or away from the observer.

Global trends in velocity gradients

Figure 3.14 shows radial profiles of $|\nabla v_{\mathrm{LSR},\perp}|$ (blue) and $|\nabla v_{\mathrm{LSR},\parallel}|$ (orange) of the four B5 filaments. The solid lines and the shaded regions show their median value and

their 25- to 75-percentile ranges, respectively. On scales larger than $\sim 10''$, the radial trends of $|\nabla v_{\rm LSR,\perp}|$ and $|\nabla v_{\rm LSR,\parallel}|$ are effectively the same in all radii. This result is different from that seen by Chen et al. (2020c) in Perseus NGC 1333 on larger scales (~ 0.05 pc), where $|\nabla v_{\rm LSR,\perp}|$ and $|\nabla v_{\rm LSR,\parallel}|$ can have distinctly different profiles. If the velocity gradients measured in B5 arise from acceleration/deceleration associated with accretion flows, then such a trend suggests that the radial (i.e., perpendicular) and longitudinal (i.e., parallel) accretion flows share the same behaviour regardless of their distance from a filament spine. Naively, such a result is contrary to behaviour expected from gravitationally dominated accretion, e.g., as found in simulations by (Gómez & Vázquez-Semadeni, 2014) where the flows are preferentially more radial further away from the filament and more longitudinal inside a filament. It is important to reiterate, however, that a velocity field and its corresponding acceleration field do not necessarily share the same morphology.

In addition to being similar to each other, the radial profiles of $|\nabla v_{\rm LSR,\perp}|$ and $|\nabla v_{\rm LSR,\parallel}|$ in the B5 filaments are also fairly constant, with the exception of those found in filament *d*. The median values of these constant profiles are in the range of $1.7 - 2.3$ km s^{-1} pc^{-1}, which is within the range of large-scale (> 0.2 pc) velocity gradients measured from other filaments in the Gould Belt Clouds ($\sim 0.5 - 5$ km s^{-1} pc^{-1}; e.g., Kirk et al. 2013b, Fernández-López et al. 2014, Lee et al. 2014b, Hacar et al. 2017). While it is tempting to interpret such a constant profile as the result of a $v\,(r) \propto -r$ type of infall, we note the $\nabla v_{\rm LSR,\perp}$ and $\nabla v_{\rm LSR,\parallel}$ in B5 are not completely smooth and featureless (see Figure 3.13). The B5 filaments actually contain a wealth of compact $\nabla v_{\rm LSR}$ structures, and the magnitudes of these structures are typically at least twice that of the radially averaged values. Though some of these structures found within the densest parts of the filament may indeed indicates a $v\,(r) \propto -r$ type of infall (see Section 3.5.4), the complex nature of the $\nabla v_{\rm LSR}$ structures found in B5 suggest additional physical processes are at play, as we have discussed earlier.

Figure 3.15 shows polar histograms of the $\nabla v_{\rm LSR}$ orientation measured in the B5 filaments. By convention, the 0° angle points along the filament spine, away from the end closest to the origin of the image. The 90° and −90° angles, on the other hand, point away and towards the spine, respectively. The light to dark colors correspond to contributions from pixels in the radial distance bins from $r = 0'' - 40''$, divided into increments of $10''$. Pixels with estimated $\nabla v_{\rm LSR}$ errors larger than their magnitudes are excluded from the sample.

With the exception of filament *a*, the $\nabla v_{\rm LSR}$ of the B5 filaments are not randomly

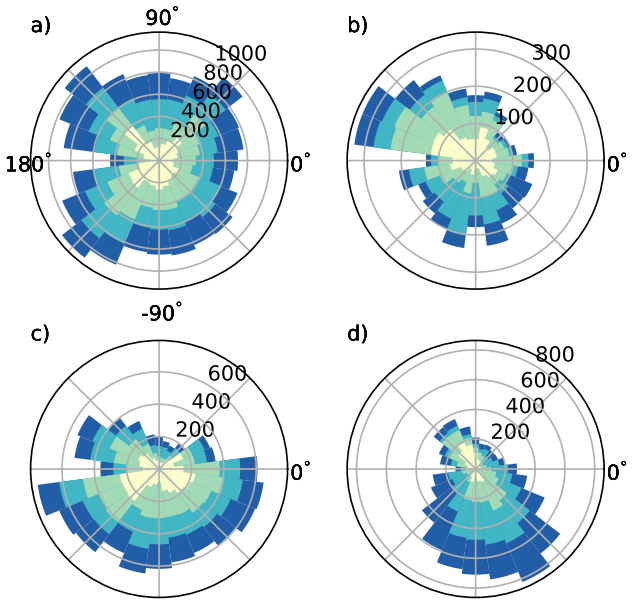

Figure 3.15: Polar histograms of the $\nabla v_{\rm LSR}$ orientation measured in the B5 filaments. By convention, 0° points along the filament spine, away from the end closest to the origin of the image, and 90° and −90° point away and towards the spine, respectively. The light to dark colors correspond to contributions from pixels in the radial bins from $r = 0 - 40''$, divided into increments of $10''$. Pixels with estimated $\nabla v_{\rm LSR}$ errors larger than their magnitudes are excluded from the sample.

distributed, consistent with what Chen et al. (2020c) found for filaments in Perseus NGC 1333 at the $\sim$ 0.05 pc scale. The orientations found in NGC 1333 on those scales, however, are much more unimodally or bimodally distributed than those we find in B5. Given that the small-scale $\nabla v_{\rm LSR}$ field we measured in B5 appears fairly ordered on the $\sim$ 0.05 pc scale (see Figure 3.12), observations made at a resolution comparable to such a scale will likely average-out the smaller-scale variations and produce more pronounced trends of $\nabla v_{\rm LSR}$ orientations, as seen in NGC 1333.

The $\nabla v_{\rm LSR}$ orientations measured in B5 also tend to be less random for pixels located near the spines than those measured further away from the spine. Given that these $\nabla v_{\rm LSR}$ fields are not often well ordered on scales $\gtrsim 30''$, as demonstrated by the LIC visualization seen in Figure 3.12), such an increase in randomness at the larger radial distance bins is thus partially due to the larger size of such bins that of course

encompass a larger part of the sky than their smaller counterparts. Nevertheless, while these radial trends do not necessarily imply the $\nabla v_{\rm LSR}$ orientation is intrinsically more random further away from the filament spines, they do illustrate that the small-scale $\nabla v_{\rm LSR}$ orientations measured in B5 ($\sim 10''$) are not well organized at larger distances ($\gtrsim 80''$). This result suggests fields, such as gravity or a magnetic field, are not imposing order near the densest structures of B5. Indeed, we do not see preferred parallel or perpendicular $\nabla v_{\rm LSR}$ field associated with the B5 filaments.

3.6 Summary and Conclusions

In this paper, we performed spectral fits to the NH_3 (1,1) observations of the Perseus B5 region with the GBT-only (P10) and the GBT+VLA combined data (P15). The spectral fits were carried out automatically using the `MUFASA` package (Chen et al., 2020c), which selects the best model between the noise, a one-component fit, and a two-component fit using the AICc criteria (Akaike 1974; Sugiura 1978). We used the GBT-only data to analyse the low surface brightness (i.e., diffuse) gas that is largely not seen in the VLA+GBT data, and used the VLA+GBT data to analyze the compact structures.

By employing the `CRISPy` package (Chen et al., 2020c), we identified four filament spines in B5 precisely from our best-fit emission models of the VLA+GBT data in PPV space. We further sorted the spectral components best fitted to the VLA+GBT data based on their kinematic similarities. The component that is the most kinematically similar to their surrounding one-component-fitted pixels are grouped together to form a final set of $v_{\rm LSR}$ and σ_v maps. We computed the velocity gradient field, i.e., $\nabla v_{\rm LSR}$ on the $10''$ scale, i.e., ~ 2 beam widths, from the resulting, final $v_{\rm LSR}$ maps and performed a detailed, high-resolution analysis of the filament kinematics on these final $v_{\rm LSR}$ and σ_v maps.

The main results of our analyses are summarized as follows:

1. We found two kinematically distinct populations of gas in B5 with the GBT-only data, ones with subsonic and supersonic levels of non-thermal velocity dispersion. The former originates from the bright, compact structure often known as the B5 'core,' while the latter surrounds the former not only in projection (see also P10) but also along the lines of sight, as revealed by our two-component fits. This result suggests the latter is indeed a part of the ambient, supersonic

cloud.

2. The two gas populations revealed by the GBT-only data have $v_{\rm LSR}$ values that tend to differ by > 0.3 km s^{-1} in the north (see Figure 3.3). This behaviour indicates the subsonic, compact region in B5 is moving through its ambient environment at a transonic/supersonic speed, potentially indicative of a dynamic origin such as one from intersecting shock fronts (e.g. Pudritz & Kevlahan 2013). This interpretation is further supported by the the ambient gas having a sharp $\Delta v_{\rm LSR} > 0.3$ km s^{-1} transition between its northwestern and southeastern regions that correlates with locations of the densest structures in B5 (see Figure 3.8).

3. The filamentary structures resolved by the VLA+GBT data in B5 not only have subsonic levels of internal σ_v (see also P10), but also have subsonic levels of $v_{\rm LSR}$ (i.e., bulk motions) relative to one another. This behaviour contrasts greatly from those of fibers found by Hacar & Tafalla (2011) in C^{18}O observations and of sub-filaments found by Clarke et al. (2017) in their simulations, which have supersonic levels of relative line-of-sight motions.

4. The B5 filaments have averaged integrated intensity radial profiles that resemble the Plummer-like functions remarkably well. The best-fit Plummer-like functions to filaments *a*, *b*, *c*, and *d* have best-fitted power-law index p values of 2.5 ± 0.1, 2.3 ± 0.1, 3.1 ± 0.1, and 3.5 ± 0.4, respectively. Interestingly, the p values found for filaments *c*, and *d* are higher than those typically found in dust continuum studies (~ 2; e.g., Arzoumanian et al. 2011).

5. The FWHM widths of filaments *a*, *b*, *c*, and *d* inferred from best-fitted Plummer-like functions are 0.025 ± 0.01 pc, 0.029 ± 0.02 pc, 0.023 ± 0.01 pc, and 0.028 ± 0.03 pc, respectively. These values are significantly smaller than those often found by the dust continuum studies (e.g., Arzoumanian et al. 2011) but consistent with those found by dense gas tracer studies of the clouds (e.g., Orion A; Hacar et al. 2018).

6. The radial σ_v profiles of the B5 filaments tend to increase monotonically towards larger radii and tend to have either a linear or flat profile within the subsonic regime. Such a behaviour is similar to that found by Heigl et al. (2020) in their simulated filaments with accretion-driven turbulence. Alternatively, if the

decrease in the non-thermal component of σ_v corresponds to unresolved infall motion rather than turbulence, as proposed by Vázquez-Semadeni et al. (2019), then the radial σ_v profiles we measured in the B5 filaments may correspond to $v\,(r) \propto -r$ type of prestellar infall motion (e.g., Whitworth & Summers 1985).

7. The $\nabla v_{\rm LSR}$ field we measured in B5 on the $10''$ scale appears to be well ordered locally, often on scales of $\sim 30''$ (~ 0.04 pc), but not always consistently across scales of an entire filament or larger.

8. The $\nabla v_{\rm LSR}$ component that is perpendicular to the filament spines (i.e., $\nabla v_{\rm LSR,\perp}$) often contains compact, elongated structures that run parallel to the spines, with magnitudes typically > 4 km s^{-1} pc^{-1}. While the structures found within the inner regions of the filaments may indicate $v\,(r) \propto -r$ type of infall, the alternating sign change of these structures outside the inner regions indicates additional physical processes at play. Such processes may include velocity vortices driven by radial, inhomogeneous accretions flows (Clarke et al., 2017), which may conform to the "fray and fragment" formation scenario proposed by Tafalla & Hacar (2015).

9. The radial profiles of $|\nabla v_{\rm LSR,\perp}|$ and $|\nabla v_{\rm LSR,\parallel}|$ closely resemble each other, suggesting forces that may impose order on the filament scale, such as gravity or a magnetic field, do not strongly govern the small-scale acceleration fields traced by $\nabla v_{\rm LSR}$. For three of the four B5 filaments in particular, both of these profiles are relatively flat and have median values in the range of $1.7 - 2.3$ km s^{-1} pc^{-1}.

Our $\nabla v_{\rm LSR}$ analyses of the B5 filaments revealed a wealth of complex kinematic structures previously unexplored at the 0.009 pc scale in observations and simulations. While the complex $\nabla v_{\rm LSR}$ field of B5 suggests turbulence and infall continue to dominate motions within subsonic structures, detailed synthetic observations of simulations are needed to further determine the nature of these motions, particularly regarding the decreasing σ_v towards the filament centers. Even though we did not find observational trends at the smaller scales that can differentiate between filament formation models between the gravoturbulent and the global hierarchical collapse scenarios, the velocity discontinuity observed on the larger-scales in the ambient gas suggests a formation scenario within a shock front, which disfavors the hierarchical collapse narrative. Observational confirmation of such a shock front in B5 will be crucial to place further constraints on filament formation scenarios.

Chapter 4

Filament Accretion and Fragmentation in the Perseus Molecular Cloud

4.1 Introduction

Advancements in observational and theoretical studies over the past decade have shown that star formation is intimately linked to filaments in molecular clouds (André et al., 2014). Observationally, filaments are both ubiquitous in molecular clouds (e.g., André et al. 2010) and seem to host a majority of the star-forming cores in these clouds (Könyves et al., 2015). Theoretically, filaments can be naturally produced by supersonic turbulence in molecular clouds (e.g., Porter et al. 1994; Vazquez-Semadeni 1994); and can undergo collapse to form stars under self-gravity (e.g., e.g., Ostriker et al. 1999; Ballesteros-Paredes et al. 1999; Mac Low & Klessen 2004). Details on how filaments are assembled in molecular clouds and subsequently produce stars, however, is not well constrained currently.

Formation of dense cores, the direct progenitor of protostars (Di Francesco et al., 2007), is often thought to occur through filament fragmentation (André et al., 2014). Under this scenario, filaments with masses per unit length ($M_{\rm lin}$) above the thermally critical value of $M_{\rm lin,crit} \sim 16$ M$_\odot$ (Ostriker 1964) are expected to collapse or fragment when modelled as cylinders near hydrostatic equilibrium. Consequently, the perturbations that grow the fastest during the thermally subcritical phase are expected to determine the fragmentation length scale in both quasi-equilibrium (e.g., Inutsuka &

Miyama 1992) and non-equilibrium (e.g., Clarke et al. 2016) cylindrical models.

On the other hand, more realistic simulations that include the cloud environment can produce filaments and cores simultaneously (e.g., Chen & Ostriker 2015b). The core properties found in these models can often be governed predominantly by cloud characteristics such as turbulent pressure and magnetic field strength. In the magnetized cases, the mass flow towards cores along the filaments, typically expected from the fragmentation models, can be significantly suppressed by the magnetic fields. Accretion towards cores and filaments in these models are thus expected to flow predominantly along the magnetic field lines, which are not necessarily perpendicular to the filaments, until cores becomes sufficiently massive at a later stage (e.g., Chen & Ostriker 2014b).

The ability to probe accretion flows with respect to the local orientation of the filaments is thus crucial to constrain core and filament formation models. Such constraints on the accretion flow behaviour can be further complemented by measurements of velocity dispersion σ_v to probe accretion driven turbulence (e.g., Klessen & Hennebelle 2010), $M_{\rm lin}$ to infer filament growth (e.g., Chira et al. 2018; Chen et al. 2020a), and average core spacing to test fragmentation theories (e.g., Inutsuka & Miyama 1992; Clarke et al. 2016). Indeed, the large-scale velocity field that runs perpendicular to the Taurus B211/3 filament and parallel to the magnetic field lines indicates that this thermally supercritical ($M_{\rm lin} \sim 54$ M$_\odot$ pc^{-1}) filament is indeed accreting from its surroundings (Palmeirim et al., 2013). Moreover, larger sample studies of filaments in the IC 5146, Aquila, and Polaris clouds have shown a correlation between $M_{\rm lin}$ and σ_v in thermally supercritical filaments, which further suggest the prevalence of filament growth through accretion (Arzoumanian et al., 2013).

While many velocity gradient ($\nabla v_{\rm LSR}$) analyses of filaments have been made along (e.g., Kirk et al. 2013b; Friesen et al. 2013) and across (e.g., Fernández-López et al. 2014; Dhabal et al. 2018) filaments on the global scale, relatively few studies have measured $\nabla v_{\rm LSR}$ on the beam-resolved, smaller scales (e.g., Hacar et al. 2018). Measurements of small-scale $\nabla v_{\rm LSR}$ orientations, which have been shown to be fairly complex, are fewer still (e.g., Chen et al. 2020c; Chen et al. 2021, submitted). Here, we present one of the first systematic, large-sample studies of the $\nabla v_{\rm LSR}$ fields measured on smaller scales (~ 0.05 pc), accompanied by measurements of σ_v, $M_{\rm lin}$, and number of cores per unit length, using observations of the Perseus Molecular Cloud.

At a distance of ~ 300 pc away (Zucker et al., 2018), the Perseus Molecular Cloud is one of the most well-studied nearby star-forming clouds. The cloud's dense core

population, for example, has been systematically studied with both dust continuum (e.g., Enoch et al. 2006; Kirk et al. 2006; Sadavoy et al. 2010) and molecular observations (e.g., Kirk et al. 2007; Rosolowsky et al. 2008). Numerous surveys have also revealed the full cloud structure of Persues in dust continuum (e.g., Pezzuto et al. 2020) and molecular emission observations (e.g., Ridge et al. 2006), accompanied by higher resolution mapping of individual star-forming clumps (e.g., Pineda et al. 2011; Dhabal et al. 2019).

We layout our paper as follows: we present the observational details of our NH_3 data in Section 4.2 followed by methods on our (up to) two-component spectral fitting as well as our filament identification and analyzes in Section 4.3. We present and discuss our results in Section 4.4 and present a summary of our findings, accompanied by concluding remarks, in Section 4.5.

4.2 Data

We obtained our data as a part of the Green Bank Ammonia Survey (GAS; Friesen et al. 2017), which mapped star-forming regions in the Gould Belt molecular clouds visible to the northern hemisphere with $A_V > 7$ mag. The GAS team observed the NH_3 (1,1) and (2,2) inversion lines in these regions with the Robert C. Byrd Green Bank Telescope (GBT) using its 7-beam K-Band Focal Plane Array (KFPA) and its VErsatile GBT Astronomical Spectrometer (VEGAS) backend. The full width at half maximum (FWHM) spectral resolutions of these observations is 5.7 kHz, which corresponds to ~ 0.07 km s^{-1} at 23.7 GHz. The FWHM beam of the GBT at this frequency is $32''$, which corresponds to a physical resolution of ~ 0.05 pc at 300 pc away.

The GAS observations were conducted over $10' \times 10'$ on-sky tiles using the On-The-Fly (OTF) technique, which scans the sky with Nyquist-sampled spacing between each row. We used GBT KFPA data reduction pipeline (Masters et al., 2011) with a recipe by Mangum et al. (2007) to reduce and image these observations, respectively. Further details of the GAS data product are available in the Data Release 1 (DR1) paper Friesen et al. (2017).

4.3 Method

4.3.1 Spectral Fitting

We fitted the NH_3 (1,1) spectral lines with two-component models using the `MUFASA` software developed by Chen et al. (2020c). `MUFASA` is an automated spectral-fitter that utilizes infrastructures of the `PySpecKit` package (Ginsburg & Mirocha, 2011) to handle spectral models and least-squares fitting. `MUFASA` obtains its initial guesses for the fits using a two-step process that first fits the data after a convolution to half of its angular resolution, with initial guesses estimated from the convolved moment maps. Results obtained from the convolved fits are then interpolated and used as initial guesses for the full resolution fit. Since the NH_3 (2,2) lines were only detected over a smaller footprint of the sky relative to the (1,1) lines, we do not include the NH_3 (2,2) lines in this study.

Following Chen et al. (2020c), we modelled each spectral component of the NH_3 (1,1) emission with a slab of gas parameterized by its velocity centroid ($v_{\rm LSR}$), velocity dispersion (σ_v), excitation temperature (T_{ex}), and optical depth (τ_0). Each model spectrum is generated by performing radiatve transfer sequentially through each gas slab towards the observer, starting with the cosmic microwave background. All 18 hyperfine structures of the NH_3 (1,1) emission are accounted for in our spectral model.

`MUFASA` perform model selections between the best-fit two-component, one-component, and noise models using the corrected Akaike Information Criterion (AICc, Akaike 1974; Sugiura 1978), which accounts for finite sample size of the data with a second-order correction. Specifically, `MUFASA` selects one model over another when their AICc-determined log-likelihood, i.e., $\ln K_a^b$, is greater than a statistically robust value of 5 (Burnham & Anderson, 2004). The subscripts here denote arbitrary models a and b. Model selection with AICc on the fits to the GAS data performs similarly to the full Bayesian approach (Sokolov et al., 2020), which requires a exhaustive search of the likelihood space for each model fit. The AICc approach also recovers faint signals much better than a simple signal-to-noise ratio (S/N) cutoff approach (see Chen et al. 2020c).

4.3.2 Filaments Identification and Analysis

We use the modelled emission derived from our spectral fits to identify filaments in the position-position-velocity (PPV) space with the `CRISPy` software (Chen et al.,

2020c). `CRISPy` identifies density ridges in multi-dimensional space using the Subspace Constrained Mean Shift algorithm (Ozertem & Erdogmus 2011; Chen et al. 2014; Chen & Ostriker 2015b). We removed the hyperfine structures from the reconstructed emission to ensure the emission cube represents real kinematic structures. We accomplished this reconstruction by re-modelling the optical depth profile of each velocity slab as a single Gaussian, with the peak re-normalized to one-tenth of the τ_0 value derived from the fit to emulate optical depths of the satellite lines, which are typically thin. To optimize the spectral resolution, we further constrain the σ_v value of the model to 0.09 km s^{-1}, the minimally Nyquist-sampled value of the GAS data. Further details of such a reconstruction can be found in Chen et al. (2020c).

The emission ridges identified with `CRISPy` in continuous space are gridded back to match that of the data cube. The branches on the ridge are subsequently removed, leaving a branchless spine that traces the longest path in the ridge. We use these filament spines to sort our modelled spectra into velocity-coherent structures, i.e., structures with $v_{\rm LSR}$ that are spatially continuous. We carried out membership assignments of the velocity-coherent filaments based on each spectral slab's $v_{\rm LSR}$ proximity to the filament spines as well as their $v_{\rm LSR}$ and σ_v similarity to their neighbouring pixels. To ensure we do not include ambient gas not associated with the filament, we limited our membership to gas emission found within 5 pixels of the spine in radius, which corresponds to $r \sim 0.11$ pc. For a comparison, the typical FWHM widths (i.e., diameters) found by Herschel studies are ~ 0.1 pc (e.g., Arzoumanian et al. 2011; Arzoumanian et al. 2019). Further details on membership assignment to velocity-coherent structures are presented in the paper by Chen et al. (2020c).

The velocity gradient ($\nabla v_{\rm LSR}$) within each velocity-coherent filament are calculated by fitting a plane to the $v_{\rm LSR}$ values found within 6-pixel diameter of a given position. Such a measure is taken to ensure the $\nabla v_{\rm LSR}$ is well-resolved by the beam. For a similar reason, we do not include positions with more than one-third of its 6-pixel diameter being empty in our calculations of $\nabla v_{\rm LSR}$.

We integrated the Herschel derived column density found within the on-sky footprints of each velocity-coherent filament to estimate the total mass of each filament. The Herschel column density maps are interpolated and gridded onto the GAS data's image grid before such a calculation is performed. To calculate the integration's physical pixel size, we assumed a distance of 302 pc, 295 pc, 301 pc, 299 pc, 288 pc, and 279 pc for the B5, IC 348, B1, NGC 1333, L1448, and L1455 star-forming clumps,

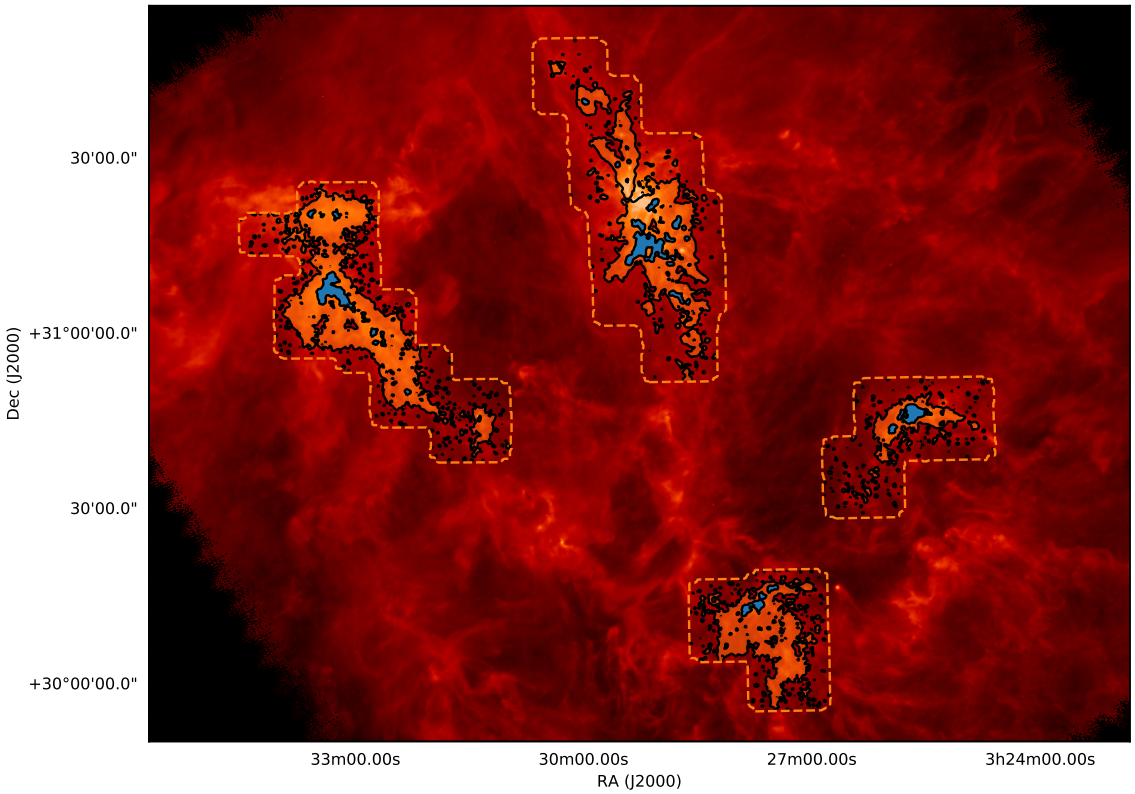

Figure 4.1: The Herschel-derived H_2 column density map of Perseus West, overlaid with filled contours of where the GBT-observed NH_3 spectra are best-fitted by one-component and two-component models in orange and blue, respectively. The extend of the GAS observation are shown in orange dashed contours.

respectively. All these distances are taken directly from the measurements by Zucker et al. (2018), except for L1455, which was not reported directly in their work. For L1455, we adopted the measurement made for L1451 instead, given their proximity to each other in projection. We note these mass estimates are an upper limit for each filament due to the presence of background emissions and occasional overlaps between the filaments in projection. We divide each filament's mass further by the length of its respective spine to calculate the $M_{\rm lin}$ of each filament.

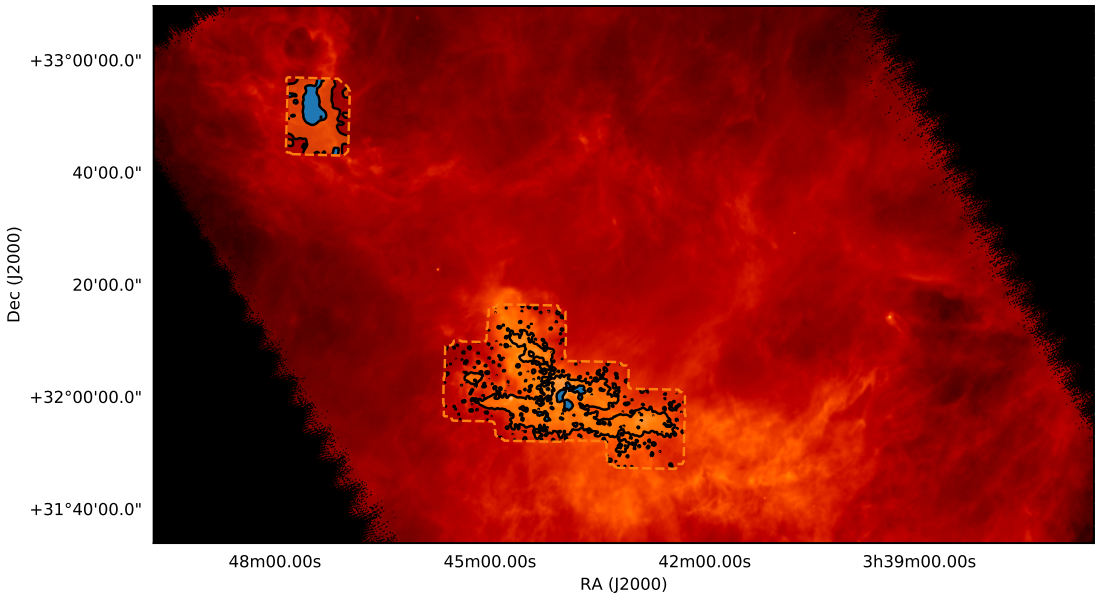

Figure 4.2: The Herschel-derived H_2 column density map of Perseus East, overlaid with filled contours of where the GBT-observed NH_3 spectra are best-fitted by one-component and two-component models, with labels the same as in Figure 4.1

4.4 Results and Discussion

4.4.1 Spectrally Modelled Data

Figures 4.1 and 4.2 show the extends of the GAS observations and the locations of where the GBT-observed NH_3 spectra are best-fitted by one-component and two-component models. The Herschel-derived H_2 column density map we used for our mass analyses are further overlaid in the background.

4.4.2 The role of clump environment

Like molecular clouds in general, most of the star formation in Perseus takes place in clumps of higher density gas where the probability density distribution of their column densities at $N(H_2) > 1 \times 10^{22}$ cm^{-2} behaves like power-law functions rather than log-normal functions expected from their parental cloud (Sadavoy et al., 2014). To showcase the range of $v_{\rm LSR}$ and $M_{\rm lin}$ cleanly within each star-forming clump, we plot the median $v_{\rm LSR}$ values of GAS filaments against their respective $M_{\rm lin}$ in Figure 4.3. As shown, the $v_{\rm LSR}$ values of the GAS filaments are consistent with the average-reddening weighted velocity calculated by Zucker et al. (2018) using the CO data

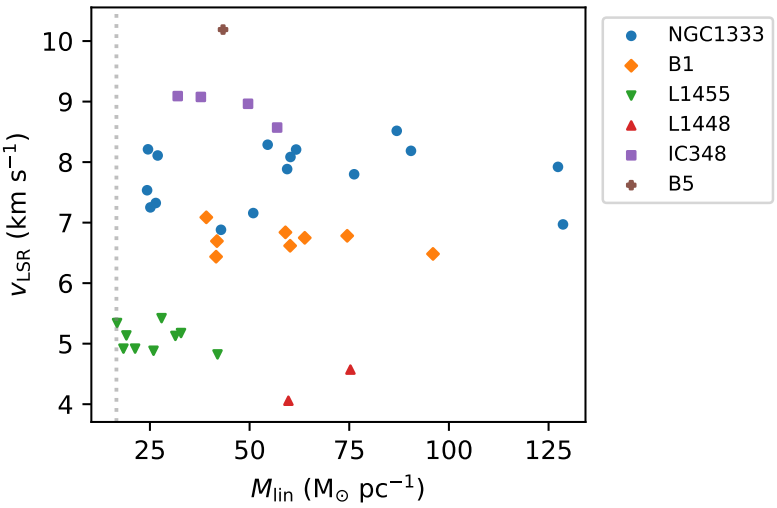

Figure 4.3: The median $v_{\rm LSR}$ of each filament plotted against the filament's $M_{\rm lin}$. The measurements taken from different star-forming clumps are marked with different symbols labeled in the legend. The value of $M_{\rm lin,crit}$ at 10 K is marked by the vertical dotted line. Errors in $M_{\rm lin,crit}$ will have to be taken into further consideration to determine if the differences are significant.

from the COMPLETE Survey (Ridge et al., 2006). We note that their data trace much larger volumes of the Perseus clumps than our NH_3 filaments.

The total mass of each Perseus clump at gas column densities of $N(H_2) > 1 \times 10^{22}$ cm^{-2} are 365 $M_\odot$, 342 $M_\odot$, 101 $M_\odot$, 118 $M_\odot$, 156 $M_\odot$, and 28 $M_\odot$ for NGC 1333, B1, L1455, L1448, IC 348, and B5, respectively (Sadavoy et al., 2014). Figure 4.4 shows the $v_{\rm LSR}$ dispersion (i.e., standard deviation) between the Perseus filaments and the mass of their respective clump, with B5 excluded due to having only one filament. Interestingly, the two quantities do not depend on each other strongly. For example, all the Perseus clumps seem to have the same, roughly sonic inter-filament $v_{\rm LSR}$ dispersion of ~ 0.2 km s^{-1} regardless of their mass. NGC 1333 and B1, on the other hand, have roughly the same clump mass, but the former has a $v_{\rm LSR}$ dispersion that is more than twice the latter. Such a difference suggests the velocity dispersion within a star-forming clump may not be driven predominantly by infall onto the clump, where the velocity dispersion is expected to scale with the gravitational potential of the clump. Even though these clumps are expected to be planar under many models, projection effects should be properly considered before drawing further conclusions.

The $M_{\rm lin}$ values of the Perseus filaments do not depend on the clump mass. For example, L1455 and L1448 have comparable clump masses of 101 $M_\odot$ and 118 $M_\odot$,

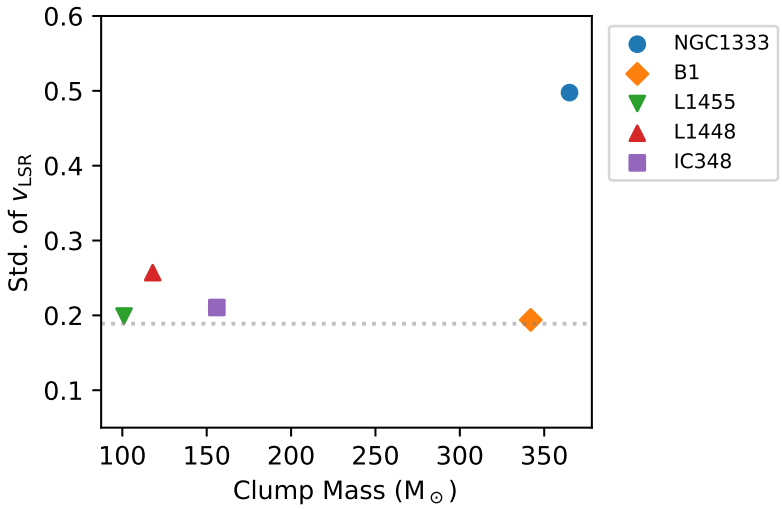

Figure 4.4: The standard deviation of the median $v_{\rm LSR}$ of each filament plotted against the mass of the star-forming clump that each filament belongs to. The symbols are the same those in Figure 4.3.

respectively, but very different $M_{\rm lin}$ values. Moreover, the number of dense filaments detected with `CRISPy` using the GAS data differs significantly between the two clumps. The number of dense filaments and their $M_{\rm lin}$ are thus unlikely drive purely by gravitational processes.

Filaments modeled as isothermal cylinders in near hydrostatic equilibrium are unstable against radial contraction and longitudinal fragmentation when their $M_{\rm lin}$ exceeds that above the critical value (Inutsuka & Miyama, 1992), i.e., $M_{\rm lin,crit} = 2c_s^2/G$ (Ostriker, 1964). In particular, radial collapse dominates in isothermal filaments with $M_{\rm lin}$ significantly larger than $M_{\rm lin,crit}$. Here, the isothermal sound speed is calculated as $c_s = (k_{\rm b}T/\mu m_{\rm H})^{1/2}$, where T is the isothermal gas temperature, and $k_{\rm b}$, μ, and $m_{\rm H}$ are the Boltzmann constant, mean interstellar molecular weight, and the atomic hydrogen mass, respectively. Assuming a mean molecular weight of $\mu = 2.33$, a 10 K filament would have $M_{\rm lin,crit} = 16.6$ M$_\odot$. As shown in Figure 4.3, all filaments identified in Perseus with the GAS data are thermally supercritical, suggesting that they should all be contracting or fragmenting in the absence of additional support, with the former outpacing the latter for very supercritical filaments. Consistent with such an expectation, the clump with the lowest $M_{\rm lin}$ values in Perseus, i.e., L1455, also has the lowest star formation efficiency (SFE) amongst the Perseus clumps that contain Spitzer-identified young stellar objects (YSOs) (Sadavoy et al., 2014).

In comparison, the majority of the filaments identified by Pezzuto et al. (2020) in Perseus with the Herschel dust emission observations are thermally subcritical. Such a result, however, is not inconsistent with ours, given that we preferentially sample the densest filaments in Perseus by observing with NH_3, a dense gas tracer. Most filaments identified by Pezzuto et al. (2020) are indeed located well outside where NH_3 emission has been detected with GAS and where $N(H_2) > 1 \times 10^{22}$ cm^{-2}, suggesting our filaments are a higher-mass subsample of Pezzuto et al.'s filaments. The filament sample we have should thus be viewed as those from the denser population that are more likely to be thermally supercritical.

4.4.3 Velocity dispersion and gradients

Accreting filaments can expect to have higher σ_v than their non-accreting counterpart through accretion-driven turbulence (e.g., Klessen & Hennebelle 2010). Figure 4.5 shows the median σ_v of each filament plotted against their respective $M_{\rm lin}$. Similar to results found by Arzoumanian et al. (2013) for thermally supercritical filaments, the σ_v and $M_{\rm lin}$ of the Perseus filaments are correlated. The linear regression model that best fits this trend has a slope of 1.1 ± 0.2 m s^{-1} M$_\odot^{-1}$ pc. For a comparison, Arzoumanian et al. (2013) fitted their data with a power-law model, which has a best-fit index of 0.36 ± 0.07. We note Arzoumanian et al.'s sample mostly falls in a higher range of σ_v than ours, i.e., $\sim 0.2 - 0.6$ km s^{-1}, with two filaments having values of ~ 1 km s^{-1}.

The observed correlation between σ_v and $M_{\rm lin}$ has been interpreted by Arzoumanian et al. (2013) as the consequences of accretion/contraction driven turbulence (e.g., Klessen & Hennebelle 2010) that increases with filament growth via accretion. Indeed, the filament accretion rate does appear to depend on $M_{\rm lin}$ in simple analytical models, where $M_{\rm lin}$ grows over time and subsequently increases accretion-driven turbulence (Heitsch, 2013). Such an interpretation also explains why no similar correlation was found by Arzoumanian et al. for thermally subcritical filaments as such filaments are not expected to be contracting.

While accretion driven turbulence also well explains the $\sigma_v - M_{\rm lin}$ relation we observe in Perseus, we note that the majority of our filaments have subsonic σ_v while those found by Arzoumanian et al. are all supersonic. If the difference between these results is physical, rather than the result of unaccounted observational biases, then they may indicate environmental differences between the observed clouds. For

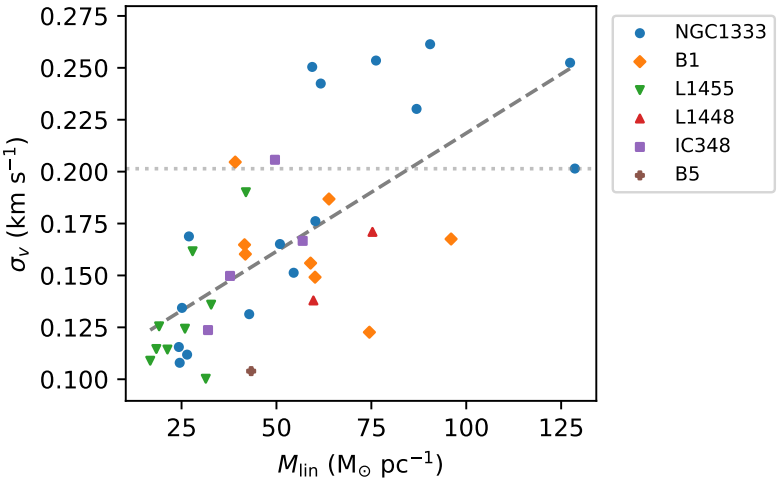

Figure 4.5: The median σ_v of each filament plotted against the filament's $M_{\rm lin}$, using the same markers as those shown in Figure 4.3. The grey dashed line marks the best-fit linear regression model while the horizontal dotted line marks the σ_v value of a 10 K gas with a sonic non-thermal component.

example, a lower σ_v may result from a higher local magnetic field strength, which can provide filaments with higher level of support against gravity while damping turbulence within them.

Velocity gradients that are perpendicular (e.g., Fernández-López et al. 2014) and parallel (e.g., Kirk et al. 2013b) to the filament spine have often been interpreted as mass flow onto and along filaments, respectively. Figure 4.6 shows the median magnitudes of the perpendicular component of $\nabla v_{\rm LSR}$ (i.e., $|\nabla v_{\rm LSR,\perp}|$), plotted against their parallel counterparts (i.e., $|\nabla v_{\rm LSR,\parallel}|$) for individual Perseus filaments. The linear regression model that best fits these data has a slope of 0.73 ± 0.16. The shaded region that highlights the regime between the 1:1 and 1:2 lines suggests that while $|\nabla v_{\rm LSR,\parallel}|$ and $|\nabla v_{\rm LSR,\parallel}|$ are fairly comparable in magnitude in the Perseus clump filaments, a significant number have $|\nabla v_{\rm LSR,\parallel}|$ that is about twice as large as their $|\nabla v_{\rm LSR,\perp}|$ counterparts.

Figure 4.7 shows the median $|\nabla v_{\rm LSR,\perp}|$ (left) and the $|\nabla v_{\rm LSR,\parallel}|$ (right) of the Perseus filament plotted against their $M_{\rm lin}$ counterparts. Interestingly, a correlation exists between $|\nabla v_{\rm LSR,\perp}|$ and $M_{\rm lin}$, but not for their $|\nabla v_{\rm LSR,\parallel}|$. The linear regression model best-fitted to the former has a best-fitted slope of 9.7 ± 2.5 m s^{-1} M$_\odot$ while the latter has no significant slope based on a Wald Test with a t-distribution, which has a p-value of $=0.1$. Here, p-value is the probably that the observed data can be

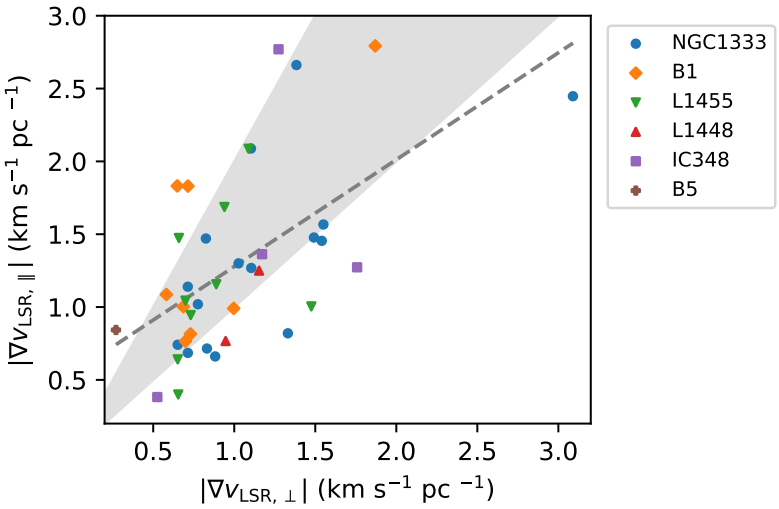

Figure 4.6: The median $|\nabla v_{\mathrm{LSR},\perp}|$ of the Perseus filaments plotted against their $|\nabla v_{\mathrm{LSR},\parallel}|$ counterparts. The marker symbols are the same as those found in Figure 4.3. The best-fitted linear regression models are represented the grey dashed line. The solid shaded region shows the area between the 1:1 and 1:2 lines.

drawn from the distribution assumed for the null hypothesis, which is a zero-slope distribution in this case.

Since ∇v_{LSR} can be a sign of acceleration/deceleration associated with gas flow, the correlation between $|\nabla v_{\mathrm{LSR},\perp}|$ and M_{lin} likely indicates that the radial (i.e., perpendicular) accretion rate of filaments does indeed increase with M_{lin}, much in the manner predicted by analytical models (e.g., Heitsch 2013). Even if the observed ∇v_{LSR} does not directly trace accretion flow, inhomogeneous radial accretion can still produce prominent $|\nabla v_{\mathrm{LSR},\perp}|$ by generating vortices with axes that run parallel to the filament spines, as seen in simulations by Clarke et al. (2017). Indeed, the morphology of clumpy, alternating $\nabla v_{\mathrm{LSR},\perp}$ structures found by Chen et al. (2020c) for Perseus NGC 1333 using the same data analyzed here as well as the elongated $\nabla v_{\mathrm{LSR},\perp}$ structures found by Chen et al. (2021, submitted) using much higher resolution ($\sim$ 0.01 pc) NH_3 observations are both qualitatively consistent with the line-of-sight velocity structures seen in those simulations.

The $\nabla v_{\mathrm{LSR},\parallel}$ values seen on the scales of filament lengths, on the other hand, have been often attributed to longitudinal mass flow accreting towards a star-forming hub (e.g., Kirk et al. 2013b). Under such a scenario, $|\nabla v_{\mathrm{LSR},\parallel}|$ should depend mostly on the gravitational potential of the hub, rather than M_{lin}. The presence of such flows may be why $|\nabla v_{\mathrm{LSR},\parallel}|$ and M_{lin} do not appear to be correlated in Perseus. Moreover,

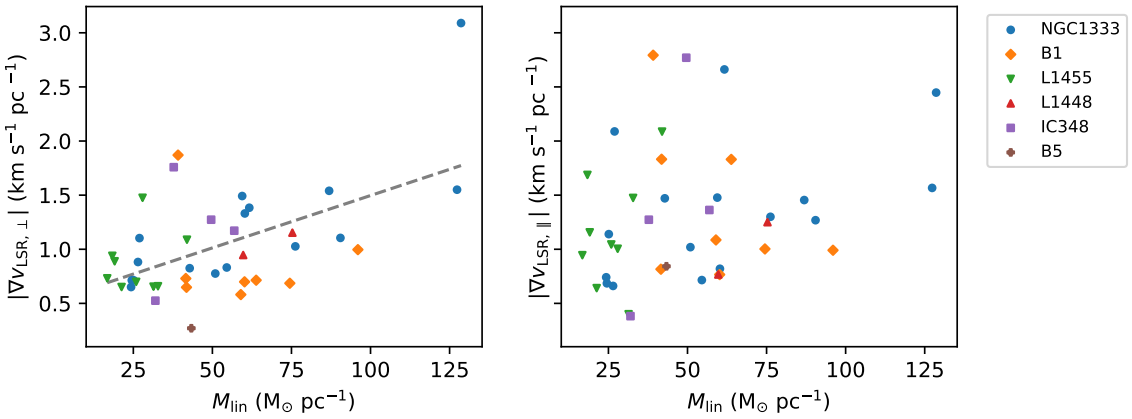

Figure 4.7: The median $|\nabla v_{\mathrm{LSR},\perp}|$ (left) and the $|\nabla v_{\mathrm{LSR},\parallel}|$ (right) of the Perseus filament plotted against their M_{lin} counterparts. The marker symbols are the same as those found in Figure 4.3 and the best-fitted linear regression models are represented by the grey dashed lines.

since Perseus clumps do not feature prominent star-forming hubs (with perhaps the exception of NGC 1333), we do not necessarily expect $|\nabla v_{\mathrm{LSR},\parallel}|$ to depend on M_{lin} indirectly via co-evolution of hubs and their associated filaments.

Considering the ∇v_{LSR} values we measure are over scales much smaller than the filament lengths (e.g., ~ 0.05 pc), $\nabla v_{\mathrm{LSR},\parallel}$ could also be a measure of velocity structures caused by other processes such as longitudinal filament fragmentation (e.g., Inutsuka & Miyama 1992) or oscillation (e.g., Gritschneder et al. 2017). If these processes are indeed responsible for the observed $\nabla v_{\mathrm{LSR},\parallel}$ behavior found in Perseus, then they do not seem to depend strongly on either the M_{lin} of the filament or other filament properties that co-evolve with M_{lin}.

To further examine the role of accretion-driven turbulence, Figure 4.8 shows the median $|\nabla v_{\mathrm{LSR},\perp}|$ (left) and the $|\nabla v_{\mathrm{LSR},\parallel}|$ (right) of the Perseus filaments plotted against their median σ_v counterparts. Interestingly, the perpendicular and parallel components of $|\nabla v_{\mathrm{LSR}}|$ both correlate with the σ_v of each filament. The slopes of the linear regression models that best fit the trends found in the left and the right panels are 6.1 ± 1.4 pc^{-1} and 7.7 ± 1.7 pc^{-1}, respectively. The correlation between $|\nabla v_{\mathrm{LSR}}|$ and σ_v thus does not discriminate strongly between the perpendicular and parallel components of $|\nabla v_{\mathrm{LSR}}|$. Given that $|\nabla v_{\mathrm{LSR},\parallel}|$ does not correlate well with M_{lin}, the increase in σ_v with M_{lin} (see Figure 4.5) are thus unlikely caused predominately by presumed increase in radial accretion driven by higher M_{lin}. Instead, other drivers

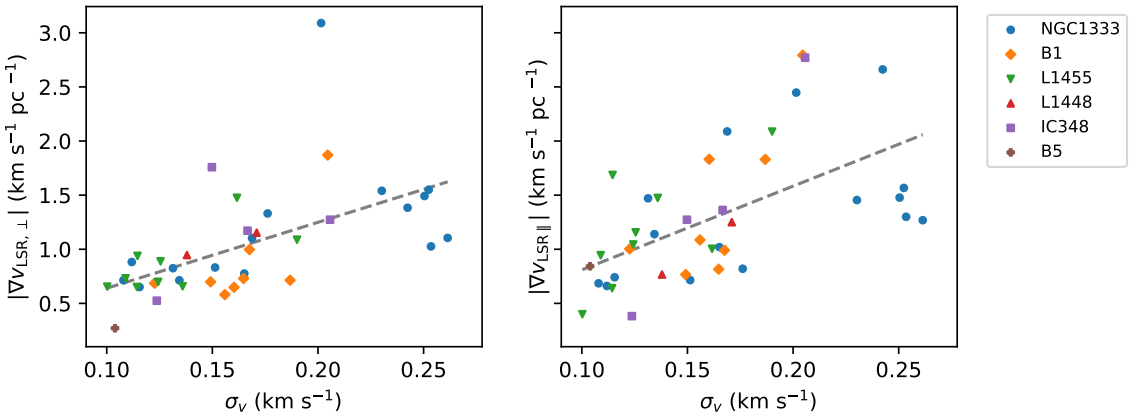

Figure 4.8: The median $|\nabla v_{\mathrm{LSR},\perp}|$ (left) and the $|\nabla v_{\mathrm{LSR},\parallel}|$ (right) of the Perseus filament plotted against their median σ_v counterparts. The marker symbols are the same as those found in Figure 4.3 and the best-fitted linear regression models are represented by the grey dashed lines.

behind the increased $|\nabla v_{\mathrm{LSR},\parallel}|$, such as fragmentation, may be potentially responsible for increasing σ_v. We will revisit this speculation with respect to core formation in Section 4.4.4.

4.4.4 Filament fragmentation, cores, and YSOs

Cores have been theorized to form in thermally supercritical filaments via fragmentation (André et al., 2014), which are seeded during the subcritical phase by the fastest growing perturbation in both quasi-equilibrium (e.g., Inutsuka & Miyama 1992) and non-equilibrium (e.g., Clarke et al. 2016) models of isolated filaments. Under these models, the number of cores within each filament is not expected to increase once supercriticality is reached due to filament fragmentation or radial collapse outpacing perturbation growth.

Figure 4.9 shows the number of cores in each Perseus filament plotted against their M_{lin} counterparts. The cores are taken from catalogs by Pattle et al. (2021, in prep.) and the linear regression model that best fits the data has a slope of 0.12 ± 0.03 $\mathrm{M}_{\odot}{}^{-1}$. The correlation between cores per unit length and M_{lin} may suggest the average spacing between cores in a filament depends on M_{lin}. But since all our filaments are thermally supercritical and have likely evolved far past the subcritical phase for which initial conditions for fragmentation are set, M_{lin} will have to depend on other properties that set core spacing during the subcritical phase for such an

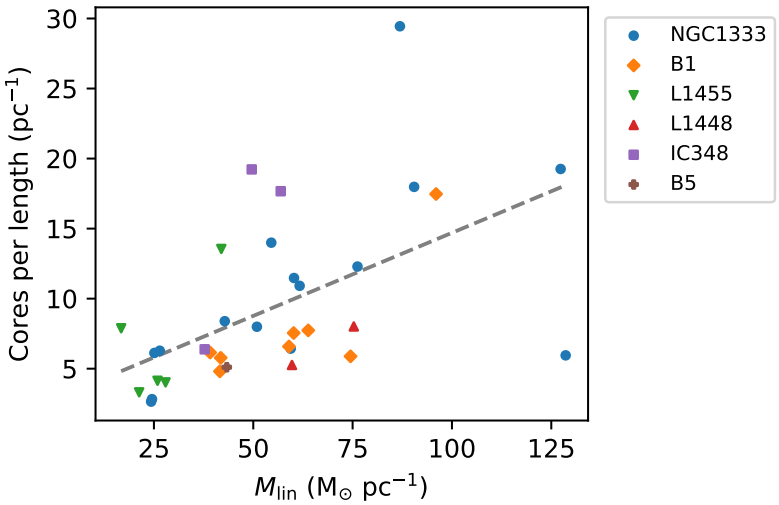

Figure 4.9: The number of cores per unit length in each Perseus filament plotted against their $M_{\rm lin}$ counterparts. The marker symbols are the same as those found in Figure 4.3. The best-fitted linear regression model is represented the grey dashed line.

interpretation to hold. For example, accretion flow with higher level of turbulence could produce more filament substructure (e.g., Clarke et al. 2017) while driving $M_{\rm lin}$ towards higher values during their subsequent evolution in the supercritical phase.

Alternatively, the correlation between the number of cores per unit length and $M_{\rm lin}$ may suggest the number of cores can continue to increase as filaments evolve past the subcritical stage. Indeed, simulations of filaments in a molecular cloud, rather than in isolation, have shown that the number of fragments (i.e., cores) and the mean $M_{\rm lin}$ of these filaments tend to increase consistently over time, even after their mean $M_{\rm lin}$ is well above the supercritical value (Chira et al., 2018). Moreover, the typical separation between these fragments and their closest neighbours within the same filament decreases over time, indicating that the cores-per-unit-length values of these filaments and their respective $M_{\rm lin}$ are correlated. Such co-evolution may thus well explain the correlation we found between cores per unit length and $M_{\rm lin}$ in the Perseus filaments.

To see if the co-evolution between cores and $M_{\rm lin}$ also maps onto newly-formed, deeply-embedded protostars, Figure 4.10 shows the number of Class 0/I YSOs per unit length in each Perseus filament plotted against their $M_{\rm lin}$ counterparts. Our YSO sample was taken from the YSO catalog by Dunham et al. (2015), selected for those found within the on-sky footprints of each filament. The linear regression model that

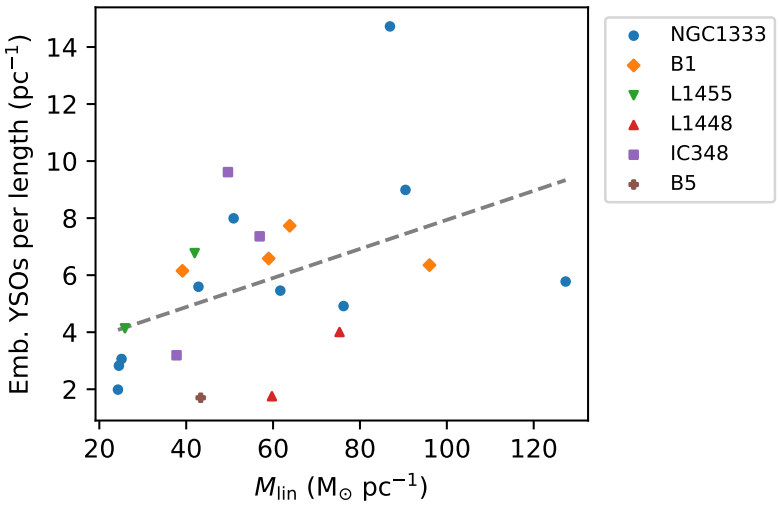

Figure 4.10: The number of class 0/1 YSOs per unit length in each Perseus filament plotted against their $M_{\rm lin}$ counterparts. The marker symbols are the same as those found in Figure 4.3. The best-fitted linear regression model is represented the grey dashed line.

best fits the data here is 0.051 ± 0.023 M$_\odot{}^{-1}$, with a p-value of 0.04 for the zero-slope null hypothesis, which is less robust than the other correlations we have found partially due the smaller sample size here. Given that the cores are direct progenitors of YSOs, and the Class 0/I YSOs identified by Dunham et al. (2015) are expected to be embedded in some of the cores identified by Pattle et al. (2021, in prep.), the correlation we find here may indeed results from a simple, linear mapping of number of cores per unit length to their number of YSO counterpart.

Figure 4.11 shows the number of cores per unit length (left) of each Perseus filament and their Class 0/I YSOs counterparts (right) plotted against their respective median σ_v values. The linear regression models best-fit to these data have slopes of 77 ± 18 s km^{-1} pc^{-1} and 38 ± 11 s km^{-1} pc^{-1}, respectively. As discussed in Section 4.4.3, the correlation between σ_v and $M_{\rm lin}$ in Perseus filaments may not be driven purely by higher radial accretion rate for filaments with larger $M_{\rm lin}$ values. The correlation between $M_{\rm lin}$ and the number of cores/YSOs per unit length thus suggest the infall towards core/YSOs also contributes significantly to the increase of σ_v in filaments. Indeed, N_2H^+ observations of Perseus cores showed that protostellar cores, i.e., collapsing cores, have σ_v values that are higher than their prestellar counterparts by ~ 0.5 km s^{-1} on average (Kirk et al., 2007).

While we do not find any correlation between $|\nabla v_{\rm LSR,||}|$ and the number of cores

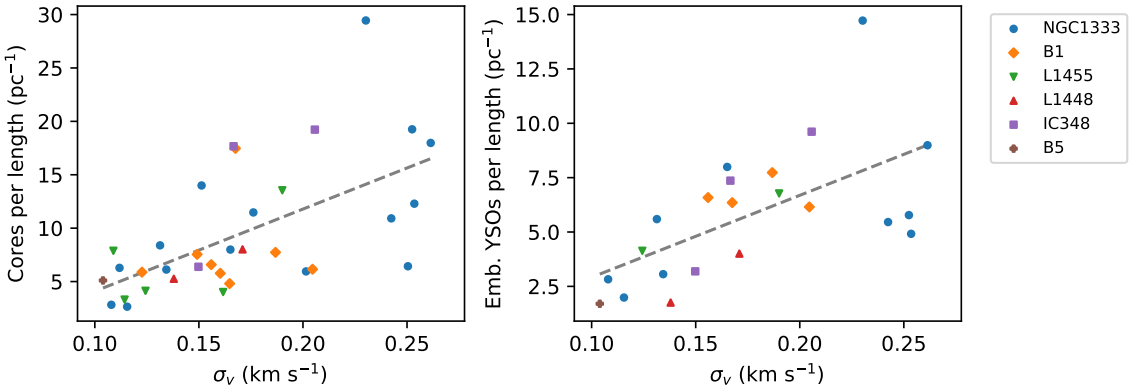

Figure 4.11: The number of cores per unit length (left) and the numbers of Class 0/I YSOs per unit length (right) of each Perseus filament plotted against their median σ_v counterparts. The marker symbols are the same as those found in Figure 4.3 and the best-fitted linear regression models are represented by the grey dashed lines.

per unit length, Figure 4.12 shows that such a correlation exists between $|\nabla v_{\mathrm{LSR},\parallel}|$ and the number of Class 0/I YSOs per unit length. The linear regression model best-fitted to the data has a slope of 0.087 ± 0.04 km s^{-1} and a zero-slope null hypothesis p-value of 0.05, which is mildly robust. This apparent correlation suggests the $|\nabla v_{\mathrm{LSR},\parallel}|$ observed on the 0.05 pc scale in filaments are likely dominated by longitudinal infall towards YSOs.

4.4.5 Velocity gradient orientations

A preferred, non-random ∇v_{LSR} orientation within a filament may indicate a well-ordered acceleration field within that filament, likely governed by gravity or magnetic field. Figure 4.13 shows the probability (i.e. the p-values) that the ∇v_{LSR} field measured in each filament is randomly oriented, plotted against the median σ_v measured in each filament. Specifically, these p-values are calculated using the Rayleigh test for uniformity (Wilkie, 1983b), where the null hypothesis assumes the orientations are uniformly distributed around a circle while the alternative hypothesis assumes the orientations are unimodally distributed. Consistent with the findings of Chen et al. 2020c in NGC 1333 using some of the same data considered here, most ∇v_{LSR} values measured in Perseus filaments on the 0.05 pc scale are not randomly distributed. Only 6 out of the 40 filaments (15%) have p-values greater than 0.001, and only 3 out of the 40 filaments (7.5%) have p-values greater than 0.05.

While we find no correlation between the Rayleigh-tested p-values and σ_v in the

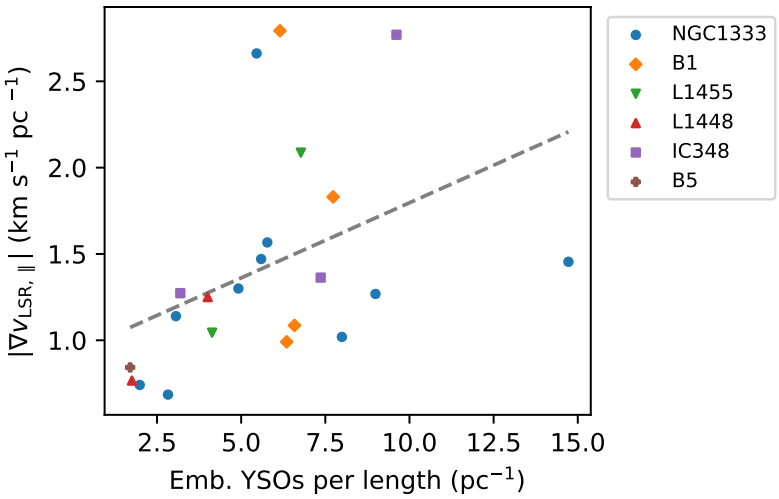

Figure 4.12: The median $|\nabla v_{\mathrm{LSR},\perp}|$ of each filament plotted against their number of class 0/1 YSOs per unit length counterparts. The marker symbols are the same as those found in Figure 4.3. The best-fitted linear regression model is represented the grey dashed line.

Perseus filaments, these two properties do nevertheless share some notable relations. For example, the higher σ_v filaments found in the subsonic regime tend to have lower probability of having a low Rayleigh-tested p-value, i.e., being being less randomly distributed. Such a relationship suggests the ∇v_{LSR} measured in the high σ_v filaments are likely more dominated by turbulence-driven motions than gravity-driven motions. In the supersonic regime, however, the probability of having a low Rayleigh-tested p-value is comparable to those found in filaments with $\sigma_v \sim 0.10$ km s^{-1}. These mildly supersonic filaments thus likely represent a different class of filament than those found in the subsonic regime, potentially differentiated by environmental factors considering that they appear to be found in NGC 1333 exclusively (see Figure 4.13).

In general, we also find no correlation between Rayleigh-tested p-values and filament properties presented in this paper, such as σ_v, M_{lin}, and $|\nabla v_{\mathrm{LSR}}|$. While a significant number of Perseus filaments have ∇v_{LSR} orientations that are highly directional (i.e., with low Rayleigh-tested p-values), the mean angle of their distribution, relative to the local orientation of the filament spine, do not correlate well with any of the filament properties either. The lack of correlation with M_{lin} suggest gravity is unlikely responsible for the observed ∇v_{LSR} fields that are directionally well ordered over an entire filament. Further study with dust polarization measurements, however, may reveal whether or not these preferred orientations align with magnetic fields.

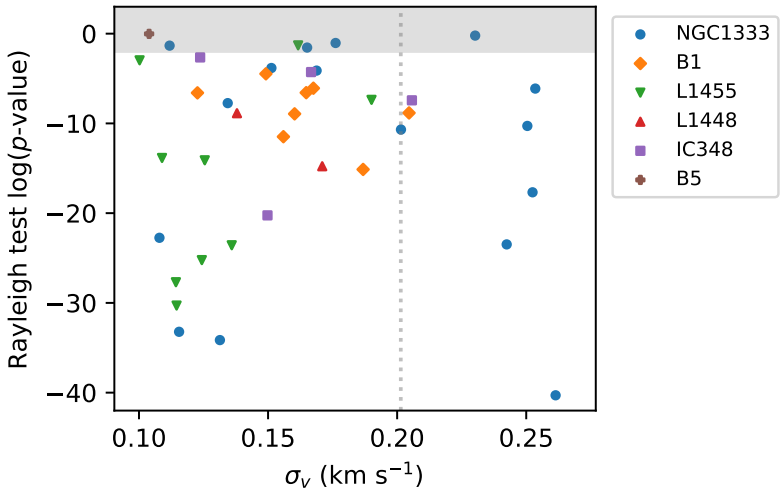

Figure 4.13: The Rayleigh test p-values for $\nabla v_{\rm LSR}$ orientations measured in each filament plotted against their respective median σ_v values. The null hypothesis of the test is that the $\nabla v_{\rm LSR}$ orientations are randomly distributed. The marker symbols are the same as those found in Figure 4.3, and the shaded region shows where p-value is greater than 0.001. The vertical dotted line shows the total σ_v value of a 10 K gas when its non-thermal component is sonic.

4.5 Summary and Conclusions

In this paper, we fit two-component spectral models to the NH_3 GBT observations of the Perseus Molecular Cloud obtained from the GAS survey (Friesen et al., 2017) using the `MUFASA` software (Chen et al., 2020c). We identify velocity-coherent filaments from our emission model in PPV space using the `CRISPy` software (Chen et al., 2020c), and subsequently sorted our modelled velocity slabs into velocity-coherent structures associated with each filament. We further measure $\nabla v_{\rm LSR}$ of these filaments on the beam-resolved scale (~ 0.05 pc), and subsequently decompose them into components that are parallel and perpendicular with respect to the local orientation of the filament spine. Moreover, we calculate mass enclosed within the boundaries of our velocity-coherent filaments using the $N(H_2)$ column density map of the Peruses Molecular Cloud derived from Herschel dust emission observations (Pezzuto et al. 2012; Sadavoy et al. 2012; Sadavoy et al. 2014; Pezzuto et al. 2020) to evaluate the gravitational potentials of these filaments.

Our main results are summarized as follows:

1. All the Perseus filaments we identified from the NH_3 data have $M_{\rm lin}$ values

greater than the thermally supercritical value of $M_{\rm lin,crit} \simeq 16$ M$_\odot$ for isothermal cylinders in hydrostatic equilibrium. The majority of these filaments have $M_{\rm lin} > 2M_{\rm lin,crit}$.

2. Most of the Perseus filaments have non-thermal velocity dispersions that are subsonic. Even in the transonic/supersonic cases, the median σ_v of the filaments are all < 0.27 km s^{-1}, which is unlikely to provide significant pressure support for the filaments.

3. Filaments in the L1455 clump, which has the lowest star formation efficiency in Perseus, have some of the lowest $M_{\rm lin}$ values within our sample, suggesting that they are fairly young and may have just reached supercriticality, marking the onset of star formation.

4. The σ_v, $M_{\rm lin}$, $|\nabla v_{\rm LSR,\perp}|$, and $|\nabla v_{\rm LSR,\parallel}|$ values we measured in filaments all tend to moderately correlate with each other positively. The only exception is the lack of correlation between $M_{\rm lin}$ and $|\nabla v_{\rm LSR,\parallel}|$, which indicates that $M_{\rm lin}$ is unlikely the sole driver behind all these kinematic trends despite seemingly being responsible for the radial-accretion-related kinematics.

5. The number of cores and Class 0/I YSOs per unit length correlates weakly with σ_v and $M_{\rm lin}$. Such a correlation suggests the physical processes that predetermine the average fragmentation spacing during the thermally subcritical phase may also set the subsequent evolution of $M_{\rm lin}$ in the supercritical phase. Alternatively, filament fragmentation spacing may not be preset solely by the initial conditions seeded during the subcritical phase, as predicted by isolated filament models (e.g., Inutsuka & Miyama 1992), but may co-evolve with $M_{\rm lin}$ well into the supercritical phase, much like those found by Chira et al. (2018) in their MHD cloud simulations.

6. The $\nabla v_{\rm LSR}$ orientations, measured on the ~ 0.05 pc scale, are not randomly distributed in filaments relative to the local spine. The mean directions of these orientations, however, do not correlate well with any of the filament properties we analyzed, suggesting the gas kinematics traced by $\nabla v_{\rm LSR}$ are not dominated by acceleration fields that are well ordered on the filament scale.

We conducted one of the first large sample studies of star-forming filament kinematics within a molecular cloud, focusing on the orientation and magnitudes of $\nabla v_{\rm LSR}$

fields measured on the ~ 0.05 pc scale. While the $\nabla v_{\rm LSR}$ orientations in the Perseus filaments are not randomly oriented, they do not show behavior naively expected of accretion flow onto and along filaments. The gas kinematics revealed by our $\nabla v_{\rm LSR}$ on these smaller scales are inherently complex. Indeed, in-depth studies of $\nabla v_{\rm LSR}$ in NGC 1333 using the same survey data (Chen et al. 2020c) and in B5 with a much higher resolution data (0.009 pc; Chen et al. 2021, submitted) revealed a wealth of complex kinematic structures on even the smaller scales.

The increase of σ_v and $|\nabla v_{\rm LSR,\perp}|$ with $M_{\rm lin}$ in the thermally supercritical filaments suggests these filaments are growing continuously via accretion, similar to the scenario proposed by Arzoumanian et al. (2013). Given the complex behavior of the $\nabla v_{\rm LSR}$ fields, particularly their orientations, these accretion flows are likely fairly turbulent and inhomogeneous, similar to those reported in simulations by Clarke et al. (2017). Furthermore, the correlation between the number of cores per unit length and $M_{\rm lin}$ can be better explained by the behavior of filaments simulated in a cloud (e.g., Chira et al. 2018) than in isolation (e.g., Inutsuka & Miyama 1992), indicating that core formation in filaments depends heavily on the environment and is not solely set by perturbation growth in the early, thermally subcritical phase.

Chapter 5

Conclusions

5.1 Conclusions of the Dissertation

In my dissertation, I demonstrated that star-forming filaments in the Perseus Molecular Cloud are far from being the idealized isothermal cylinders in hydrostatic quasi-equilibrium described in the classical model (Ostriker, 1964). Not only do these dense filaments, as traced by NH_3 emission, contain noticeable curves and bends in their morphologies, they also tend to have masses per unit length ($M_{\rm lin}$) that are thermally supercritical. These filaments' supercritical states suggest they should be contracting radially or fragmenting longitudinally if they are not further supported by means beyond thermal pressure.

While reaching thermal criticality is likely necessary for filaments to form stars, the correlations I unveiled between $M_{\rm lin}$ of the Perseus filaments and other filament properties suggest that filaments can continue to grow well past the critical phase through mass accretion. Indeed, the correlation between velocity dispersion (σ_v) and $M_{\rm lin}$ in the Perseus filaments suggests accretion-driven turbulence is responsible for such a trend. Furthermore, except for the higher $M_{\rm lin}$ filaments in NGC 1333, nearly all the Perseus filaments have subsonic internal motions despite this increasing σ_v trend. This result suggests that having subsonic internal motion may be an important initial condition for filaments to grow and reach thermal criticality rather than re-expanding back into the cloud as transient structures.

My measurements of smaller-scale velocity gradient fields in filaments showed that filament accretion in Perseus is more complex than expected from analytic models (e.g., Heitsch 2013), as well as complex hydrodynamic (e.g., Gómez & Vázquez-

Semadeni 2014) and magnetohydrodynamic simulations (Chen & Ostriker 2015b). On the 0.05 pc scale, neither do the inferred filament accretions appear to be smooth nor do the preferred velocity gradient orientations correlate with other filament properties when present in filaments. The latter lack of correlation suggests the preferred velocity gradient orientations are independent of filament evolution and may be strongly influenced by the filament's environment. On the 0.01 pc scale, the velocity gradient field does not have a globally preferred orientation. This lack of preference suggests either gravity and magnetic fields are not the dominant forces on the 0.01 pc scale, or these forces are not well-ordered on these scales. Therefore, turbulence may remain important in dense filaments even though these filaments tend to have subsonic internal motions, unlike their supersonic parental cloud.

The correlation between the number of cores per unit length and $M_{\rm lin}$ further suggests that filament fragmentation may not be predetermined by perturbation growth during the thermally subcritical phase, as predicted from models of isolated filaments. Instead, this correlation can be better explained by the ongoing fragmentation of the growing, supercritical filament, such as those simulated from within a wider cloud environment (Chira et al., 2018). Together with the complex kinematic structures probed by the velocity gradient, my result suggests a scenario for which turbulence is not only crucial to the formation of filaments, as expected in the gravoturbulent framework (e.g., Mac Low & Klessen 2004), but also important in shaping filament growth and their subsequent fragmentation even well after filaments become subsonic and thermally supercritical.

5.2 Work Moving Forward

5.2.1 Investigating the Role of Magnetic Fields

While turbulence and gravity have commonly been considered the dominant player in structure formation and evolution within molecular clouds (e.g., Mac Low & Klessen 2004; Vázquez-Semadeni et al. 2019), theoretical and observational studies have also shown that magnetic fields can become important at certain physical regimes (e.g., Kudoh & Basu 2008; Li et al. 2009; Vázquez-Semadeni et al. 2011). For example, magnetohydrodynamic simulations (e.g., Chen & Ostriker 2014b; Chen & Ostriker 2015b) have shown that magnetic fields can guide accretion flows onto filaments while simultaneously preventing these filaments from fragmenting longitudinally. Indeed, this

behavior appears to conform to that observed in a few case studies (e.g., Palmeirim et al. 2013; Chen et al. 2020a), and the lack of correlation between the preferred velocity gradient orientations I found for several Perseus filaments in this dissertation and their respective filament properties suggests that magnetic fields, which are not always perpendicularly aligned with the filaments, may be at play. A holistic theory of star formation must therefore also include the role of magnetic fields.

The coupling between magnetic field, velocity field, and gas morphology means magnetic fields can be inferred from velocity (González-Casanova & Lazarian, 2017) or density (Soler et al., 2013) gradients in the absence of dust polarization data. The technique I developed for my dissertation lends naturally to measuring vector fields relative to the filament spines, allowing detailed investigations of the relationship between velocity gradients, density gradients, and dust polarization. Such an investigation would allow us to probe further the robustness of these techniques and the role of magnetic fields in star formation. For example, the 14″ angular resolution polarization maps of nearby molecular clouds from the BISTRO survey (Pattle et al., 2017) would be excellent for conducting such a study, particularly in comparison with the GAS data. Since interferometric facilities such as the Very Large Array (VLA) and Atacama Large Millimeter/submillimeter Array (ALMA) can observe molecular lines and dust polarization, they would be in excellent positions to follow up on the BISTRO and GAS studies. The planned polarization surveys with the upcoming TolTEC instruments for the Large Millimetre Telescope (LMT) will also provide invaluable data for a large sample study of filaments at a 6″ resolution in the near future, easily complementing the resolution of VLA and ALMA at their more compact configurations.

5.2.2 Multi-tracer Surveys

While my dissertation has made significant progress in understanding star-forming filaments preferentially sampled by NH_3 emission at densities $\gtrsim 10^3$ cm^{-3} (Shirley, 2015), a comprehensive kinematic comparison with lower density, non-star-forming filaments is further needed to constrain the physics that governs core and star formation in filaments. Furthermore, since mass assembly in star formation is a highly multi-scale process, studying gas dynamics requires observations that are sensitive to a broad range of angular scales and gas volume densities. While the former can be achieved with a combination of single-dish and interferometric data, the latter is often

achieved by observing different molecular species that are chemically differentiated by their environment.

Even though large multi-tracer surveys have been historically cost-prohibitive, the Argus+ instrument proposed for the GBT in the US AStro2020 Decadal Survey can significantly alter that status. The 144-element radio camera of Argus+ will not only increase the mapping speed of the GBT by an order of magnitude at the 3-mm band (74 –116 GHz), it will also have angular resolutions of $6.5'' - 10''$, making it highly complementary to the LMT's $6''$ resolution for dust polarimetry surveys. This synergy can be particularly productive when Argus+ is used to observe both the neutral (e.g., CO and HCN) and ionized (e.g., HCO^+ and N_2H^+) gas species to understand better the ion-neutral coupling to magnetic fields. Furthermore, mapping of SiO at such high resolutions can be used to determine whether or not accretion or turbulence-induced shocks are commonly present on the filament level, a crucial test to rule in favor of the gravoturbulent framework of star formation (e.g., Mac Low & Klessen 2004) over the global hierarchical collapse framework (e.g., Vázquez-Semadeni et al. 2019).

Further down the road, the Next Generation Very Large Array (ngVLA) will not only be able to observe molecular species accessible to GBT's Argus+ but also other species that are excellent probes of gas properties such as temperatures (e.g., NH_3) and densities (e.g., H_2CO). Even when the ngVLA observation is convolved to resolutions comparable to ALMA and VLA for a comparison, ngVLA's main 214 x 18m array will be able to achieve the same data sensitivity as ALMA and VLA with at least an order of magnitude less integration time. Combined with ngVLA's unprecedented angular resolution of at least ~ 0.5 mas (i.e., at the lowest frequency band), the ngVLA's ability to access a wide range of molecular species capable of probing various densities makes it an excellent facility to study the multi-scale physics behind star formation, both in our Milky Way and potentially the galaxies beyond.

5.3 Synthetic Observations

One of the outstanding challenges in the study of star formation is our ability to constrain theoretical models. Due to the nature of observation, gas behaviors seen in simulations do not often map trivially onto the observations. Radiative transfer, tracer chemistry, and projection effects can all make parsing the underlying physics behind an observation difficult. Synthetic observations that model these 'viewing

effects' realistically are thus needed to compare simulations with observations accurately.

Analyzing synthetic observations of simulations that include a full chemical network and account for radiative transfer, such as those by Offner et al. (2014), will thus be a crucial first step to interpret better the results of my dissertation, particularly with regards to velocity gradient measurements. Expanding similar work to simulations that incorporate magnetic fields, complemented by synthetic polarization observations of these simulations, will also be needed to place further pivotal constraints on theoretical models.

Bibliography

Akaike, H. 1974, IEEE Transactions on Automatic Control, 19, 716

André, P., Di Francesco, J., Ward-Thompson, D., et al. 2014, Protostars and Planets VI, 27, doi: 10.2458/azu_uapress_9780816531240-ch002

André, P., Men'shchikov, A., Könyves, V., & Arzoumanian, D. 2011, in IAU Symposium, Vol. 270, Computational Star Formation, ed. J. Alves, B. G. Elmegreen, J. M. Girart, & V. Trimble, 255–262, doi: 10.1017/S1743921311000470

André, P., Men'shchikov, A., Bontemps, S., et al. 2010, A&A, 518, L102, doi: 10.1051/0004-6361/201014666

André, P., Revéret, V., Könyves, V., et al. 2016, A&A, 592, A54, doi: 10.1051/0004-6361/201628378

Arzoumanian, D., André, P., Peretto, N., & Könyves, V. 2013, A&A, 553, A119, doi: 10.1051/0004-6361/201220822

Arzoumanian, D., André, P., Didelon, P., et al. 2011, A&A, 529, L6, doi: 10.1051/0004-6361/201116596

Arzoumanian, D., André, P., Könyves, V., et al. 2019, A&A, 621, A42, doi: 10.1051/0004-6361/201832725

Ballesteros-Paredes, J., Hartmann, L., & Vázquez-Semadeni, E. 1999, ApJ, 527, 285, doi: 10.1086/308076

Bally, J., Langer, W. D., Stark, A. A., & Wilson, R. W. 1987, ApJ, 312, L45, doi: 10.1086/184817

Balsara, D., Ward-Thompson, D., & Crutcher, R. M. 2001, MNRAS, 327, 715, doi: 10.1046/j.1365-8711.2001.04787.x

Barranco, J. A., & Goodman, A. A. 1998, ApJ, 504, 207, doi: 10.1086/306044

Barrett, A. H., Ho, P. T. P., & Myers, P. C. 1977, ApJ, 211, L39, doi: 10.1086/182338

Bastien, P., Arcoragi, J.-P., Benz, W., Bonnell, I., & Martel, H. 1991, ApJ, 378, 255, doi: 10.1086/170424

Beaumont, C. N., Offner, S. S. R., Shetty, R., Glover, S. C. O., & Goodman, A. A. 2013, ApJ, 777, 173, doi: 10.1088/0004-637X/777/2/173

Benson, P. J., & Myers, P. C. 1989, ApJS, 71, 89, doi: 10.1086/191365

Blake, G. A., Sandell, G., van Dishoeck, E. F., et al. 1995, ApJ, 441, 689, doi: 10.1086/175392

Bonnell, I. A., Bate, M. R., & Vine, S. G. 2003, MNRAS, 343, 413, doi: 10.1046/j.1365-8711.2003.06687.x

Burnham, K. P., & Anderson, D. R. 2004, Sociological Methods Research, 33, 261

Cabral, B., & Leedom, L. C. 1993, in Proceedings of the 20th annual conference on Computer graphics and interactive techniques, SIGGRAPH '93 (New York, NY, USA: ACM), 263–270, doi: 10.1145/166117.166151

Caselli, P., van der Tak, F. F. S., Ceccarelli, C., & Bacmann, A. 2003, A&A, 403, L37, doi: 10.1051/0004-6361:20030526

Chabrier, G. 2003, PASP, 115, 763, doi: 10.1086/376392

Chabrier, G. 2005, in Astrophysics and Space Science Library, Vol. 327, The Initial Mass Function 50 Years Later, ed. E. Corbelli, F. Palla, & H. Zinnecker, 41, doi: 10.1007/978-1-4020-3407-7_5

Chen, C.-Y., Mundy, L. G., Ostriker, E. C., Storm, S., & Dhabal, A. 2020a, MNRAS, 494, 3675, doi: 10.1093/mnras/staa960

Chen, C.-Y., & Ostriker, E. C. 2014a, ApJ, 785, 69, doi: 10.1088/0004-637X/785/1/69

—. 2014b, ApJ, 785, 69, doi: 10.1088/0004-637X/785/1/69

—. 2015a, ApJ, 810, 126, doi: 10.1088/0004-637X/810/2/126

—. 2015b, ApJ, 810, 126, doi: 10.1088/0004-637X/810/2/126

Chen, H. H.-H., Offner, S. S. R., Pineda, J. E., et al. 2020b, arXiv e-prints, arXiv:2006.07325. https://arxiv.org/abs/2006.07325

Chen, H. H.-H., Pineda, J. E., Goodman, A. A., et al. 2019a, ApJ, 877, 93, doi: 10.3847/1538-4357/ab1a40

Chen, H.-R. V., Zhang, Q., Wright, M. C. H., et al. 2019b, ApJ, 875, 24, doi: 10.3847/1538-4357/ab0f3e

Chen, M. C.-Y. 2020a, MUlti-component Fitter for Astrophysical Spectral Applications, 0.1, Zenodo, doi: 10.5281/ZENODO.3637660

—. 2020b, Computational Ridge Identification with SCMS for Python, 0.1, Zenodo, doi: 10.5281/ZENODO.3637613

Chen, M. C.-Y., Francesco, J. D., Rosolowsky, E., et al. 2020c, ApJ, 891, 84, doi: 10.3847/1538-4357/ab7378

Chen, Y.-C., Genovese, C. R., & Wasserman, L. 2014, ArXiv e-prints. https://arxiv.org/abs/1406.1803

Chen, Y.-C., Ho, S., Freeman, P. E., Genovese, C. R., & Wasserman, L. 2015, MNRAS, 454, 1140, doi: 10.1093/mnras/stv1996

Chira, R. A., Kainulainen, J., Ibáñez-Mejía, J. C., Henning, T., & Mac Low, M. M. 2018, A&A, 610, A62, doi: 10.1051/0004-6361/201731836

Choudhury, S., Pineda, J. E., Caselli, P., et al. 2020, A&A, 640, L6, doi: 10.1051/0004-6361/202037955

Clarke, S. D., Whitworth, A. P., Duarte-Cabral, A., & Hubber, D. A. 2017, MNRAS, 468, 2489, doi: 10.1093/mnras/stx637

Clarke, S. D., Whitworth, A. P., & Hubber, D. A. 2016, MNRAS, 458, 319, doi: 10.1093/mnras/stw407

Clarke, S. D., Whitworth, A. P., Spowage, R. L., et al. 2018a, MNRAS, 479, 1722, doi: 10.1093/mnras/sty1675

—. 2018b, MNRAS, 479, 1722, doi: 10.1093/mnras/sty1675

Cohen, J. 1988, Statistical Power Analysis for the Behavioral Sciences (Lawrence Erlbaum Associates)

Dhabal, A., Mundy, L. G., Chen, C.-y., Teuben, P., & Storm, S. 2019, ApJ, 876, 108, doi: 10.3847/1538-4357/ab15d3

Dhabal, A., Mundy, L. G., Rizzo, M. J., Storm, S., & Teuben, P. 2018, ApJ, 853, 169, doi: 10.3847/1538-4357/aaa76b

Di Francesco, J., Evans, II, N. J., Caselli, P., et al. 2007, Protostars and Planets V, 17

Dole, H., Lagache, G., Puget, J.-L., et al. 2006, A&A, 451, 417, doi: 10.1051/0004-6361:20054446

Dunham, M. M., Allen, L. E., Evans, Neal J., I., et al. 2015, ApJS, 220, 11, doi: 10.1088/0067-0049/220/1/11

Elmegreen, B. G., Efremov, Y., Pudritz, R. E., & Zinnecker, H. 2000, Protostars and Planets IV, 179

Enoch, M. L., Young, K. E., Glenn, J., et al. 2006, ApJ, 638, 293, doi: 10.1086/498678

Evans, II, N. J. 1999, ARA&A, 37, 311, doi: 10.1146/annurev.astro.37.1.311

Fahrmeir, L., Kneib, T., Lang, S., & Marx, B. 2013, Regression: Models, Methods and Applications, doi: 10.1007/978-3-642-34333-9

Federrath, C. 2016, MNRAS, 457, 375, doi: 10.1093/mnras/stv2880

Fernández-López, M., Arce, H. G., Looney, L., et al. 2014, ApJ, 790, L19, doi: 10.1088/2041-8205/790/2/L19

Friesen, R. K., Di Francesco, J., Shirley, Y. L., & Myers, P. C. 2009, ApJ, 697, 1457, doi: 10.1088/0004-637X/697/2/1457

Friesen, R. K., Medeiros, L., Schnee, S., et al. 2013, MNRAS, 436, 1513, doi: 10.1093/mnras/stt1671

Friesen, R. K., Pineda, J. E., co-PIs, et al. 2017, ApJ, 843, 63, doi: 10.3847/1538-4357/aa6d58

Fuller, G. A., Myers, P. C., Welch, W. J., et al. 1991, ApJ, 376, 135, doi: 10.1086/170262

Ginsburg, A., & Mirocha, J. 2011, PySpecKit: Python Spectroscopic Toolkit, Astrophysics Source Code Library. http://ascl.net/1109.001

Goldsmith, P. F., Heyer, M., Narayanan, G., et al. 2008, ApJ, 680, 428, doi: 10.1086/587166

Gómez, G. C., & Vázquez-Semadeni, E. 2014, ApJ, 791, 124, doi: 10.1088/0004-637X/791/2/124

Gong, H., & Ostriker, E. C. 2011a, ApJ, 729, 120, doi: 10.1088/0004-637X/729/2/120

—. 2011b, ApJ, 729, 120, doi: 10.1088/0004-637X/729/2/120

González-Casanova, D. F., & Lazarian, A. 2017, ApJ, 835, 41

Goodman, A. A., Barranco, J. A., Wilner, D. J., & Heyer, M. H. 1998, ApJ, 504, 223, doi: 10.1086/306045

Gritschneder, M., Heigl, S., & Burkert, A. 2017, ApJ, 834, 202, doi: 10.3847/1538-4357/834/2/202

Hacar, A., Kainulainen, J., Tafalla, M., Beuther, H., & Alves, J. 2016, A&A, 587, A97, doi: 10.1051/0004-6361/201526015

Hacar, A., & Tafalla, M. 2011, A&A, 533, A34, doi: 10.1051/0004-6361/201117039

Hacar, A., Tafalla, M., & Alves, J. 2017, A&A, 606, A123, doi: 10.1051/0004-6361/201630348

Hacar, A., Tafalla, M., Forbrich, J., et al. 2018, A&A, 610, A77, doi: 10.1051/0004-6361/201731894

Hacar, A., Tafalla, M., Kauffmann, J., & Kovács, A. 2013, A&A, 554, A55, doi: 10.1051/0004-6361/201220090

Heiderman, A., Evans, II, N. J., Allen, L. E., Huard, T., & Heyer, M. 2010, ApJ, 723, 1019, doi: 10.1088/0004-637X/723/2/1019

Heigl, S., Gritschneder, M., & Burkert, A. 2020, MNRAS, 495, 758, doi: 10.1093/mnras/staa1202

Heitsch, F. 2013, ApJ, 769, 115, doi: 10.1088/0004-637X/769/2/115

Heitsch, F., Ballesteros-Paredes, J., & Hartmann, L. 2009, ApJ, 704, 1735, doi: 10.1088/0004-637X/704/2/1735

Henshaw, J. D., Longmore, S. N., Kruijssen, J. M. D., et al. 2016, MNRAS, 457, 2675, doi: 10.1093/mnras/stw121

Henshaw, J. D., Jiménez-Serra, I., Longmore, S. N., et al. 2017, MNRAS, 464, L31, doi: 10.1093/mnrasl/slw154

Heyer, M. H., & Brunt, C. M. 2004, ApJ, 615, L45, doi: 10.1086/425978

Hill, T., Motte, F., Didelon, P., et al. 2011, A&A, 533, A94, doi: 10.1051/0004-6361/201117315

Ho, P. T. P., & Townes, C. H. 1983, ARA&A, 21, 239, doi: 10.1146/annurev.aa.21.090183.001323

Inutsuka, S.-I., & Miyama, S. M. 1992, ApJ, 388, 392, doi: 10.1086/171162

Inutsuka, S.-i., & Miyama, S. M. 1997, ApJ, 480, 681, doi: 10.1086/303982

Jappsen, A. K., Klessen, R. S., Larson, R. B., Li, Y., & Mac Low, M. M. 2005, A&A, 435, 611, doi: 10.1051/0004-6361:20042178

Juvela, M., Malinen, J., & Lunttila, T. 2012, A&A, 544, A141, doi: 10.1051/0004-6361/201219558

Keown, J., Di Francesco, J., Teimoorinia, H., Rosolowsky, E., & Chen, M. C.-Y. 2019, ApJ, 885, 32, doi: 10.3847/1538-4357/ab4657

Kirk, H., Johnstone, D., & Di Francesco, J. 2006, ApJ, 646, 1009, doi: 10.1086/503193

Kirk, H., Johnstone, D., & Tafalla, M. 2007, ApJ, 668, 1042, doi: 10.1086/521395

Kirk, H., Myers, P. C., Bourke, T. L., et al. 2013a, ApJ, 766, 115, doi: 10.1088/0004-637X/766/2/115

—. 2013b, ApJ, 766, 115, doi: 10.1088/0004-637X/766/2/115

Klessen, R. S., & Burkert, A. 2000, ApJS, 128, 287, doi: 10.1086/313371

Klessen, R. S., & Hennebelle, P. 2010, A&A, 520, A17, doi: 10.1051/0004-6361/200913780

Koch, E. W., & Rosolowsky, E. W. 2015, MNRAS, 452, 3435, doi: 10.1093/mnras/stv1521

Könyves, V., André, P., Men'shchikov, A., et al. 2010, A&A, 518, L106, doi: 10.1051/0004-6361/201014689

—. 2015, A&A, 584, A91, doi: 10.1051/0004-6361/201525861

Kramer, C., Stutzki, J., Rohrig, R., & Corneliussen, U. 1998, A&A, 329, 249

Kroupa, P. 2001, MNRAS, 322, 231, doi: 10.1046/j.1365-8711.2001.04022.x

Krumholz, M. R., Klein, R. I., & McKee, C. F. 2007, ApJ, 656, 959, doi: 10.1086/510664

Krumholz, M. R., & McKee, C. F. 2005, ApJ, 630, 250, doi: 10.1086/431734

Kudoh, T., & Basu, S. 2008, ApJ, 679, L97, doi: 10.1086/589618

Kullback, S., & Leibler, R. A. 1951, Ann. Math. Statist., 22, 79, doi: 10.1214/aoms/1177729694

Larson, R. B. 1981, MNRAS, 194, 809, doi: 10.1093/mnras/194.4.809

Lee, K. I., Fernández-López, M., Storm, S., et al. 2014a, ApJ, 797, 76, doi: 10.1088/0004-637X/797/2/76

—. 2014b, ApJ, 797, 76, doi: 10.1088/0004-637X/797/2/76

Levenberg, K. 1944, Quarterly of Applied Mathematics, 2, 164

Li, H.-b., Dowell, C. D., Goodman, A., Hildebrand , R., & Novak, G. 2009, ApJ, 704, 891, doi: 10.1088/0004-637X/704/2/891

Li, Z.-Y., & Nakamura, F. 2004, ApJ, 609, L83, doi: 10.1086/422839

Lourakis, M. I. A. 2005, A Brief Description of the Levenberg-Marquardt Algorithm Implemened by levmar, Tech. rep., Institute of Computer Science, Foundation for Research and Technology - Hellas (FORTH), Vassilika Vouton, P.O. Box 1385, GR 711 10. http://users.ics.forth.gr/~lourakis/levmar/levmar.pdf

Mac Low, M.-M., & Klessen, R. S. 2004, Reviews of Modern Physics, 76, 125, doi: 10.1103/RevModPhys.76.125

Mangum, J. G., Emerson, D. T., & Greisen, E. W. 2007, A&A, 474, 679, doi: 10.1051/0004-6361:20077811

Mangum, J. G., & Shirley, Y. L. 2015, PASP, 127, 266, doi: 10.1086/680323

Marganian, P., Garwood, R. W., Braatz, J. A., Radziwill, N. M., & Maddalena, R. J. 2013, GBTIDL: Reduction and Analysis of GBT Spectral Line Data. http://ascl.net/1303.019

Markwardt, C. B. 2009, in Astronomical Society of the Pacific Conference Series, Vol. 411, Astronomical Data Analysis Software and Systems XVIII, ed. D. A. Bohlender, D. Durand, & P. Dowler, 251. https://arxiv.org/abs/0902.2850

Marquardt, D. W. 1963, SIAM Journal on Applied Mathematics, 11, 431, doi: 10.1137/0111030

Masters, J., Garwood, B., Langston, G., & Shelton, A. 2011, in Astronomical Society of the Pacific Conference Series, Vol. 442, Astronomical Data Analysis Software and Systems XX, ed. I. N. Evans, A. Accomazzi, D. J. Mink, & A. H. Rots, 127

Matzner, C. D., & Jumper, P. H. 2015, ApJ, 815, 68, doi: 10.1088/0004-637X/815/1/68

Mayer, C. H., Waak, J. A., Cheung, A. C., & Chui, M. F. 1973, ApJ, 182, L65, doi: 10.1086/181220

McKee, C. F., & Ostriker, E. C. 2007, ARA&A, 45, 565, doi: 10.1146/annurev.astro.45.051806.110602

McMullin, J. P., Waters, B., Schiebel, D., Young, W., & Golap, K. 2007, in Astronomical Society of the Pacific Conference Series, Vol. 376, Astronomical Data Analysis Software and Systems XVI, ed. R. A. Shaw, F. Hill, & D. J. Bell, 127

Men'shchikov, A., André, P., Didelon, P., et al. 2010, A&A, 518, L103, doi: 10.1051/0004-6361/201014668

Miville-Deschênes, M. A., Martin, P. G., Abergel, A., et al. 2010, A&A, 518, L104, doi: 10.1051/0004-6361/201014678

Miyama, S. M., Narita, S., & Hayashi, C. 1987, Progress of Theoretical Physics, 78, 1273, doi: 10.1143/PTP.78.1273

Moeckel, N., & Burkert, A. 2015, ApJ, 807, 67, doi: 10.1088/0004-637X/807/1/67

Monsch, K., Pineda, J. E., Liu, H. B., et al. 2018, ApJ, 861, 77, doi: 10.3847/1538-4357/aac8da

Moré, J. J. 1978, Lecture Notes in Mathematics, Berlin Springer Verlag, 630, 105, doi: 10.1007/BFb0067700

Moré, J. J., Garbow, B. S., & Hillstrom, K. E. 1980, User guide for MINPACK-1, Tech. Rep. ANL-80-74, Argonne Nat. Lab., Argonne, IL. http://cds.cern.ch/record/126569

Motte, F., Andre, P., & Neri, R. 1998, A&A, 336, 150

Nordlund, Å. K., & Padoan, P. 1999, in Interstellar Turbulence, ed. J. Franco & A. Carraminana, 218

Nutter, D., Kirk, J. M., Stamatellos, D., & Ward-Thompson, D. 2008, MNRAS, 384, 755, doi: 10.1111/j.1365-2966.2007.12750.x

Offner, S. S. R., Bisbas, T. G., Bell, T. A., & Viti, S. 2014, MNRAS, 440, L81, doi: 10.1093/mnrasl/slu013

Offner, S. S. R., & Liu, Y. 2018, Nature Astronomy, 2, 896, doi: 10.1038/s41550-018-0566-1

Onishi, T., Mizuno, A., Kawamura, A., Ogawa, H., & Fukui, Y. 1998, ApJ, 502, 296, doi: 10.1086/305867

Ortiz-León, G. N., Loinard, L., Dzib, S. A., et al. 2018, ApJ, 865, 73, doi: 10.3847/1538-4357/aada49

Ostriker, E. C., Gammie, C. F., & Stone, J. M. 1999, ApJ, 513, 259, doi: 10.1086/306842

Ostriker, E. C., Stone, J. M., & Gammie, C. F. 2001, ApJ, 546, 980, doi: 10.1086/318290

Ostriker, J. 1964, ApJ, 140, 1056, doi: 10.1086/148005

Ozertem, U., & Erdogmus, D. 2011, The Journal of Machine Learning Research, 12, 1249

Padoan, P., Juvela, M., Goodman, A. A., & Nordlund, Å. 2001, ApJ, 553, 227, doi: 10.1086/320636

Palmeirim, P., André, P., Kirk, J., et al. 2013, A&A, 550, A38, doi: 10.1051/0004-6361/201220500

Panopoulou, G. V., Tassis, K., Goldsmith, P. F., & Heyer, M. H. 2014, MNRAS, 444, 2507, doi: 10.1093/mnras/stu1601

Pattle, K., Ward-Thompson, D., Berry, D., et al. 2017, ApJ, 846, 122

Pezzuto, S., Elia, D., Schisano, E., et al. 2012, A&A, 547, A54, doi: 10.1051/0004-6361/201219501

Pezzuto, S., Benedettini, M., Di Francesco, J., et al. 2020, arXiv e-prints, arXiv:2010.00006. https://arxiv.org/abs/2010.00006

Pineda, J. E., Goodman, A. A., Arce, H. G., et al. 2010a, ApJ, 712, L116, doi: 10.1088/2041-8205/712/1/L116

—. 2011, ApJ, 739, L2, doi: 10.1088/2041-8205/739/1/L2

Pineda, J. E., Offner, S. S. R., Parker, R. J., et al. 2015, Nature, 518, 213, doi: 10.1038/nature14166

Pineda, J. L., Goldsmith, P. F., Chapman, N., et al. 2010b, ApJ, 721, 686, doi: 10.1088/0004-637X/721/1/686

Plummer, H. C. 1911, MNRAS, 71, 460, doi: 10.1093/mnras/71.5.460

Pon, A., Johnstone, D., & Heitsch, F. 2011, ApJ, 740, 88, doi: 10.1088/0004-637X/740/2/88

Pon, A., Johnstone, D., & Kaufman, M. J. 2012, ApJ, 748, 25, doi: 10.1088/0004-637X/748/1/25

Porter, D. H., Pouquet, A., & Woodward, P. R. 1994, Physics of Fluids, 6, 2133, doi: 10.1063/1.868217

Pudritz, R. E., & Kevlahan, N. K. R. 2013, Philosophical Transactions of the Royal Society of London Series A, 371, 20120248, doi: 10.1098/rsta.2012.0248

Ridge, N. A., Di Francesco, J., Kirk, H., et al. 2006, AJ, 131, 2921, doi: 10.1086/503704

Riener, M., Kainulainen, J., Henshaw, J. D., et al. 2019, A&A, 628, A78, doi: 10.1051/0004-6361/201935519

Rivers, M. 2002, Perform Levenberg-Marquardt Least-squares Minimization, http://cars9.uchicago.edu/software/python/mpfit.html

Rosolowsky, E., & Leroy, A. 2006, PASP, 118, 590, doi: 10.1086/502982

Rosolowsky, E. W., Pineda, J. E., Foster, J. B., et al. 2008, ApJS, 175, 509, doi: 10.1086/524299

Roy, A., André, P., Arzoumanian, D., et al. 2015, A&A, 584, A111, doi: 10.1051/0004-6361/201526431

Rufat, D. 2018, LicPy, 0.2, GitHub. https://github.com/drufat/licpy/archive/v0.2.tar.gz

Sadavoy, S. I., Di Francesco, J., Bontemps, S., et al. 2010, ApJ, 710, 1247, doi: 10.1088/0004-637X/710/2/1247

Sadavoy, S. I., di Francesco, J., André, P., et al. 2012, A&A, 540, A10, doi: 10.1051/0004-6361/201117934

Sadavoy, S. I., Di Francesco, J., André, P., et al. 2014, ApJ, 787, L18, doi: 10.1088/2041-8205/787/2/L18

Salpeter, E. E. 1955, ApJ, 121, 161, doi: 10.1086/145971

Schneider, N., André, P., Könyves, V., et al. 2013, ApJ, 766, L17, doi: 10.1088/2041-8205/766/2/L17

Schneider, S., & Elmegreen, B. G. 1979, ApJS, 41, 87, doi: 10.1086/190609

Shirley, Y. L. 2003, A quick & Dirty Guide to Astrophysical Molecular Rotation Spectroscopy

—. 2015, PASP, 127, 299, doi: 10.1086/680342

Smith, R. J., Glover, S. C. O., Bonnell, I. A., Clark, P. C., & Klessen, R. S. 2011, MNRAS, 411, 1354, doi: 10.1111/j.1365-2966.2010.17775.x

Smith, R. J., Glover, S. C. O., & Klessen, R. S. 2014, MNRAS, 445, 2900, doi: 10.1093/mnras/stu1915

Smith, R. J., Glover, S. C. O., Klessen, R. S., & Fuller, G. A. 2016, MNRAS, 455, 3640, doi: 10.1093/mnras/stv2559

Sokolov, V., Pineda, J. E., Buchner, J., & Caselli, P. 2020, ApJ, 892, L32, doi: 10.3847/2041-8213/ab8018

Sokolov, V., Wang, K., Pineda, J. E., et al. 2017, A&A, 606, A133, doi: 10.1051/0004-6361/201630350

—. 2018, A&A, 611, L3, doi: 10.1051/0004-6361/201832746

Soler, J. D., Hennebelle, P., Martin, P. G., et al. 2013, ApJ, 774, 128

Solomon, P. M., Rivolo, A. R., Barrett, J., & Yahil, A. 1987, ApJ, 319, 730, doi: 10.1086/165493

Sousbie, T. 2011, MNRAS, 414, 350, doi: 10.1111/j.1365-2966.2011.18394.x

Sousbie, T., Pichon, C., & Kawahara, H. 2011, MNRAS, 414, 384, doi: 10.1111/j.1365-2966.2011.18395.x

Stahler, S. W., & Palla, F. 2005, The Formation of Stars, 865

Stodólkiewicz, J. S. 1963, Acta Astron., 13, 30

Sugiura, N. 1978, Communications in Statistics - Theory and Methods, 7, 13, doi: 10.1080/03610927808827599

Tafalla, M., & Hacar, A. 2015, A&A, 574, A104, doi: 10.1051/0004-6361/201424576

Tafalla, M., Myers, P. C., Caselli, P., Walmsley, C. M., & Comito, C. 2002, ApJ, 569, 815, doi: 10.1086/339321

Tilley, D. A., & Pudritz, R. E. 2004, MNRAS, 353, 769, doi: 10.1111/j.1365-2966.2004.08077.x

Townes, C. H., & Schawlow, A. L. 1975, Microwave spectroscopy.

Tritsis, A., & Tassis, K. 2016, MNRAS, 462, 3602, doi: 10.1093/mnras/stw1881

—. 2018, Science, 360, 635, doi: 10.1126/science.aao1185

van der Walt, S., Schönberger, J. L., Nunez-Iglesias, J., et al. 2014, arXiv e-prints, arXiv:1407.6245. https://arxiv.org/abs/1407.6245

Vazquez-Semadeni, E. 1994, ApJ, 423, 681, doi: 10.1086/173847

Vázquez-Semadeni, E., Banerjee, R., Gómez, G. C., et al. 2011, MNRAS, 414, 2511, doi: 10.1111/j.1365-2966.2011.18569.x

Vázquez-Semadeni, E., Palau, A., Ballesteros-Paredes, J., Gómez, G. C., & Zamora-Avilés, M. 2019, MNRAS, 490, 3061, doi: 10.1093/mnras/stz2736

Walawender, J., Bally, J., Francesco, J. D., Jørgensen, J., & Getman, K. . 2008, NGC 1333: A Nearby Burst of Star Formation, ed. B. Reipurth, Vol. 4, 346

Walsh, A. J., Bourke, T. L., & Myers, P. C. 2006, ApJ, 637, 860, doi: 10.1086/498564

Whitworth, A., & Summers, D. 1985, MNRAS, 214, 1, doi: 10.1093/mnras/214.1.1

Whitworth, A. P., & Ward-Thompson, D. 2001, ApJ, 547, 317, doi: 10.1086/318373

Wilkie, D. 1983a, Applied Statistics, 32, 311

—. 1983b, Applied Statistics

Williams, J. P., de Geus, E. J., & Blitz, L. 1994, ApJ, 428, 693, doi: 10.1086/174279

Zamora-Avilés, M., Ballesteros-Paredes, J., & Hartmann, L. W. 2017, MNRAS, 472, 647, doi: 10.1093/mnras/stx1995

Zucker, C., Schlafly, E. F., Speagle, J. S., et al. 2018, ApJ, 869, 83, doi: 10.3847/1538-4357/aae97c

Appendix A

Further details on filament identification and membership assignment

A.1 Parameter choices for CRISPy

As mentioned in Section 2.3.3, the operation of SCMS, including our implementation in CRISPy, primarily depends on two user-defined parameters: density (i.e., intensity) threshold and smoothing bandwidth. We adopted a density threshold of 0.15 K to capture most of our emission in the model while avoiding going near the typical rms noise level of our data (~ 0.1 K). We further adopted a smoothing length of 1.5 pixels, which corresponds to about the 1-σ sampling width of our data, i.e., ~ 3 pixels across the FWHM beam. Since our deblended cube at its native resolution is too noisy for SCMS even after a density cutoff, we further smoothed our deblended cube spatially to twice its original beam width prior to running SCMS. We smoothed the data only spatially and not spectrally to avoid further loss in our spectral resolution.

In addition to density threshold and smoothing bandwidth parameters, SCMS requires a few additional parameters to run in practice: convergence criterion, the maximum number of iterations, and walker placement. Convergence criterion and the maximum number of iterations are used to decide when to stop running SCMS further. We set our convergence criterion to 10^{-3} to ensure the ridges represented by the converged walkers have scatters that are smaller than the equivalent width of a voxel in the deblended cube. We set the maximum number of iterations to 1000

and the walker placement such that a walker is placed at each voxel in the deblended cube above a density threshold. We adopted a walker placement threshold of 0.16 K to sample the density field well without placing walkers near the edges of the field defined by our cutoff threshold (0.15 K).

The CRISPy implementation of SCMS also includes scaling parameters for which each dimension of the deblended emission can be rescaled. The purpose of such a rescaling is to renormalize the distance between each particle in the field and consequently the density field. Such a renormalization is essential for structure identification in a parameter space with dimensions that are not necessarily physically related, e.g., a ppv space.

Since the two spatial distances in a ppv space are physically related, only the velocity axis needs to be rescaled, provided that the smoothing bandwidth was already chosen appropriately based on the spatial sampling. For our runs, we kept velocity scaling the same as the one native to our deblended cube. We made this choice deliberately to avoid elongating spatially compact structures along the velocity axis such that they are misidentified as filaments. Shorter scaling is avoided to prevent further loss in our spectral resolution from bandwidth smoothing.

A.2 Membership Assignment to Velocity Coherent Structures

As briefly described in Section 2.3.3, velocity slabs are assigned memberships to velocity-coherent structures (vc-structures) based on their proximity to filament spines in the ppv space. This process is performed iteratively, starting with pixels spatially closest to the filament spine. At each iteration, velocity slabs are assigned to spine-derived ppv-footprints nearest to them in v_{LSR} along a line of sight, which forms what we call an association. The slabs in each association are subsequently sorted internally, based on their kinematic similarities, into a vc-structure that contains only a single velocity slab along a line of sight. Here, we describe the process of assigning membership to vc-structures in more detail.

We first create a ppv-footprint, a spatial extension of a spine, to serve as a reference from which the v_{LSR} proximities between a slab and a spine are calculated along a line of sight, i.e., a pixel. We construct a ppv-footprint by dilating, i.e., expanding, filament spines by one pixel in the two spatial dimensions but not in the velocity

dimension. This expansion is initially accomplished by taking the first-moment map of a filament spine, dilating the map's on-sky footprint by one pixel, and adopting the median $v_{\rm LSR}$ value of the moment map within a 3-pixel radius of each pixel as its new value.

Once the ppv-footprint is created, velocity slabs with $v_{\rm LSR}$ values closest to the ppv-footprint at each pixel are then assigned to that ppv-footprint as a member of the association. Only slabs with velocity separations < 0.21 km s^{-1} from the ppv-footprint, i.e., about three spectral channel widths, are accepted to ensure the assigned members are reasonably velocity-coherent with respect to the ppv-footprint. We note that this threshold implicitly imposes an upper limit to velocity gradients of 0.42 km s^{-1} pix^{-1} (i.e., ~ 29 km s^{-1} pc^{-1}) for a given association.

Following these assignments, member slabs within each association are further sorted into a vc-structure containing only a single slab along each line of sight, based on their similarities in $v_{\rm LSR}$, σ_v, and $\delta v_{\rm LSR}$, i.e., the Jacobian estimated error of $v_{\rm LSR}$ from the fits. We used $\delta v_{\rm LSR}$ similarity as our additional proxy for spatial coherence assuming that spectral components which are spatially similar in their properties, such as their brightness, will produce fitted $\delta v_{\rm LSR}$ that are spatially similar as well.

At each iteration, we sort these velocity slabs as follows:

1. Assign velocity slabs with the smallest $\delta v_{\rm LSR}$ values at each pixel in a given association into a new, single slab structure we call a vc-structure.

2. Median-smooth the $\delta v_{\rm LSR}$ map of the vc-structure with a circular aperture, 1 pixel in radius, to serve as a reference map.

3. Reassign velocity slabs at each pixel with the most similar $\delta v_{\rm LSR}$ values, i.e., the least difference between the smoothed $\delta v_{\rm LSR}$ map and their respective $\delta v_{\rm LSR}$ values, to the vc-structure.

4. Create reference maps of $v_{\rm LSR}$ and σ_v by employing the same median-smoothing technique used in step 2 on property maps of the vc-structure,

5. Reassign velocity slabs with the minimum quadrature sum difference between the reference maps and their respective $v_{\rm LSR}$ and σ_v values, i.e.,

$$\left[(v_{\rm LSR} - v_{\rm LSR,ref})^2 + (\sigma_v - \sigma_{v,\rm ref})^2\right]^{0.5},$$

to the vc-structure.

Following each sortation above, we median smooth the final $v_{\rm LSR}$ map in each vc-structure with a 3 pixel radius aperture and adopt the resulting $v_{\rm LSR}$ map as our new ppv-footprint for the subsequent iteration of membership assignment and sortation. This procedure is carried out for five iterations in total, growing ppv-footprints and their respective associations radially one pixel at a time. This five pixel radial distance typically marks the spatial extent for which the SNR values of our pixels start to fall below 3.

To illustrates such a process, Figure 2.8 shows a ppv-footprint at each iteration in panels labeled with the iteration number n. The last two panels of Figure 2.8 show $v_{\rm LSR}$ maps of the first and second velocity slabs in an association, taken from the final iteration. The first slab shown here defines the final vc-structure used in our filament analyses.